Elastoplastic Response of Unidirectional Graphite/Aluminum under Combined Tension-Compression Cyclic Loading

by

Mark Wenyih Lin

Thesis submitted to the Faculty of the

Virginia Polytechnic Institute and State University

in partial fulfillment of the requirements for the degree of

Master of Science

in

Engineering Mechanics

APPROVED:

Marek-Jerzy Pindera (Chairman)

Carl T. Herakovich

Jacob Aboudi

O. Hayden Griffin

August 1987

Blacksburg, Virginia

Elastoplastic Response of Unidirectional Graphite/Aluminum under Combined Tension-Compression Cyclic Loading

by

Mark Wenyih Lin

Marek-Jerzy Pindera (Chairman)

Engineering Mechanics

(ABSTRACT)

A test fixture for combined tension-compression cyclic testing of unidirectional composites was designed and characterized using 6061-O aluminum specimens. The elastoplastic response of graphite/aluminum 15° off-axis and 90° specimens under tension-compression cyclic loading was subsequently investigated at three temperatures, -150°F, room temperature and 250°F. The test results showed that the tensile response was predominantly elastoplastic, whereas the compressive response could not be characterized exclusively on the basis of the classical plasticity theory. Secondary dissipative mechanisms caused by inherent voids in the material's microstructure had an apparent influence on the elastoplastic behavior in compression. At different test temperatures, the initial yield stress in tension and compression were translated in the tension direction with increasing temperature. This is believed to be caused by residual stresses induced in each phase of the composite. The micromechanics model proposed by Aboudi was subsequently employed to correlate the experimental and analytical results at room temperature. A semi-inverse methodology was incorporated to determine the in-situ properties of the constituents. Comparison between the analytical and experimental results showed good agreement for monotonic tensile response. For tension-compression cyclic loading, fairly good correlation was obtained for 15° specimens, but poor for 90° specimens. The major cause of the discrepancy is suggested to be caused by the secondary dissipative mechanisms.

Acknowledgements

The author would like to express his gratitude to Prof. Marek-Jerzy Pindera for the kind guidance and courteous advice throughout his graduate study and this research. Likewise, the author would like to thank Prof. Jacob Aboudi for providing the computer programs of the micromechanics analysis and his patient guidance. The author also wishes to thank Prof. C. T. Herakovich and O. H. Griffin for their helpful advice on this work.

Special thanks is due to Mr. R. L. Davis and B. Shaver. Without their expertise and timely help, the test fixture could not have been completed. The author is grateful to J. S. Hidde and T. Williams for their assistance in the experimental work, and J. M. Starbuck and for providing experimental results of their study.

The author would like to acknowledge the Materials Science Corporation and Center for Innovative Technology at Virginia Polytechnic Institute and State University for providing the material and financial support for the completion of this project.

Finally, the author would like to express his gratitude to his wife, , for her support with love and patience during the period of his graduate study and the typing of the manuscript for this thesis.

Table of Contents

List of Illustrations

List of Tables

Chapter 1 Introduction

1.1 Introduction

The study of metal matrix composite materials has received considerable attention in the past twenty years. Metal matrix composites are high-stiffness , low-weight materials that possess certain properties that are superior to those of polymer matrix composites. The most obvious properties are resistance to severe environments and retention of strength at elevated temperatures. However, due to difficulties in manufacturing techniques and high fabrication costs, the research in the area of metal matrix composites has been limited in the past. Recently, improved manufacturing techniques have eliminated a number of technical problems and reduced the fabrication costs. This, in turn, has resulted in intensive characterization of these advanced materials in the past few years.

The most common metal matrix composite is aluminum based fibrous composite. This type of composite consists of high stiffness fibers, such as boron or graphite, and ductile aluminum matrix. One of the apparent characteristics of the mechanical response of aluminum based composites is the relatively low yield strength. Typically, the elastic response occupies only a limited portion of the entire response, see Fig. 1.1. This is caused by the inherently ductile nature of the aluminum

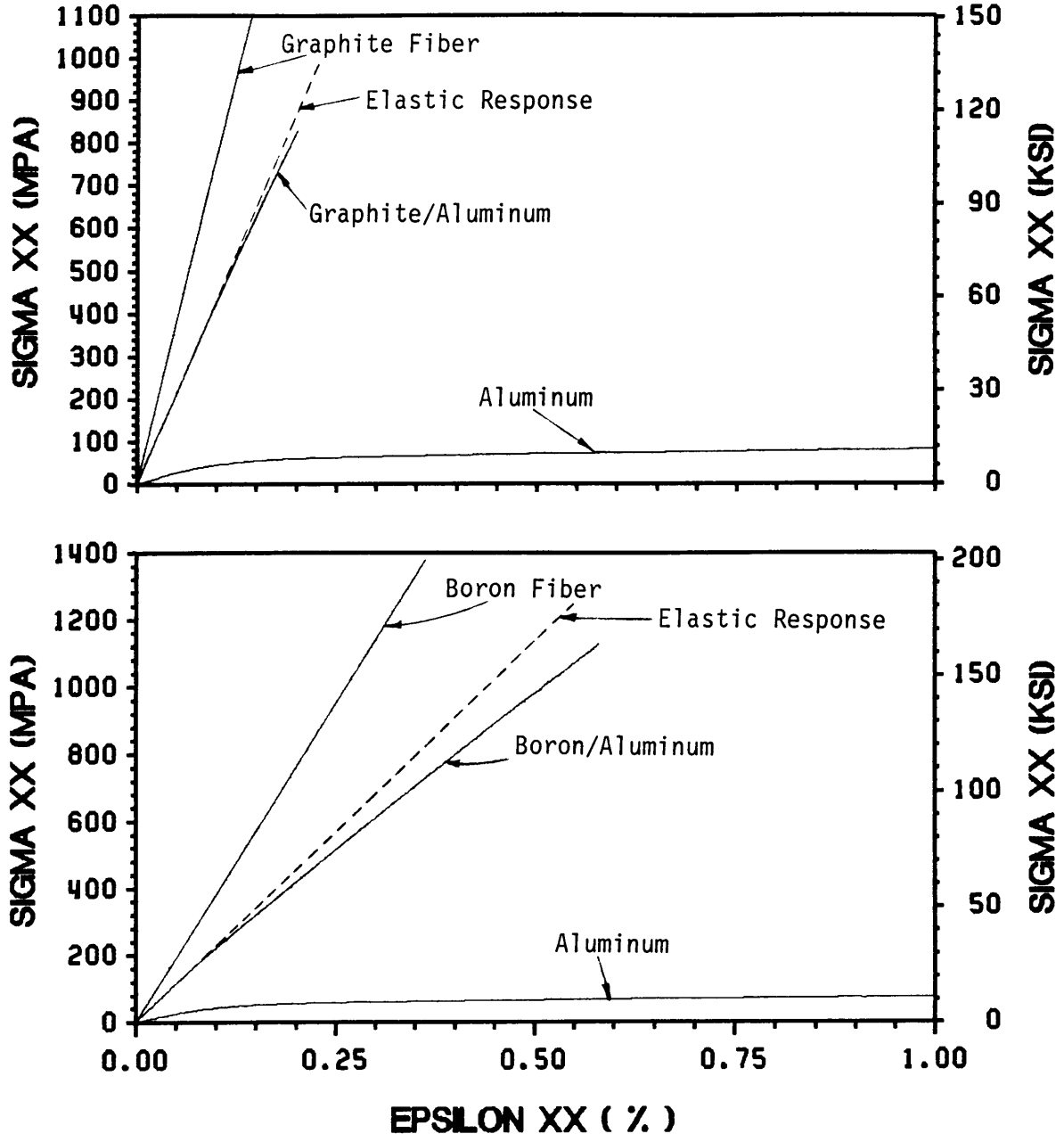

Figure 1. 1. Nonlinear characteristics of metal matrix composites.

matrix and complicated residual stresses in individual phases after fabrication. Therefore, in order to fully exploit the potential that metal matrix composites can offer, it is necessary to accurately characterize the response both in the elastic and plastic ranges. Consequently, experimental and analytical characterization of the thermomechanical response of metal matrix composites has become an area of great activity in the composite mechanics community.

In experimental investigations, promising test methodologies for tension, compression, or shear loading have been developed. Reliable test data under these types of loading conditions have also been generated. However, this type of test data supplies only a limited amount of information in the course of elastoplastic investigations. In order to further understand such elastoplastic response characteristics as the Baushinger effect, yield surface evolution, plastic strain accumulation and influence of different loading paths, combined tension-compression cyclic loading is required.

In analytical investigations, many approaches have been developed to predict the elastoplastic behavior of metal matrix composites. Among those, the so-called micromechanics formulation, which determines the overall macromechanical response of the composite from the properties and geometries of the constituents, has played a major role. Theoretically, this approach provides a straightforward formulation in predicting composite behavior. In reality, however, due to complex interactions and changes in chemical and physical properties of the constituents during the manufacturing processes, the bulk properties of the individual constituents typically employed in various micromechanics analyses may not be representative of the in-situ properties. Thus, in order to predict accurately the elastoplastic response of metal matrix composites, the above factors need to be taken into account in the course of micromechanics analyses of metal matrix composites.

A review of recent experimental and analytical investigations of the elastoplastic response of unidirectional metal matrix composites is presented in the following section.

1.2 Literature Review

The most common metal matrix composites whose thermomechanical response has been investigated experimentally are boron/aluminum and graphite/aluminum. Herakovich et al [1,2] conducted monotonic and cyclic off-axis tension and compression tests on borsic/aluminum composite laminates. In this investigation, yielding and strain hardening were analyzed. In 1976, Pipes et al [3] studied the strength and acoustic emission characteristics of unidirectional boron/aluminum laminae. Monotonic off-axis tension tests were performed on various off-axis fiber orientations, and the acoustic emission was monitored. The obtained failure strengths were compared with several failure criteria and acoustic response data were presented. Further studies were subsequently carried out by Herakovich et al [4-6]. In these investigations, the effects of temper conditions and cyclic loading on the nonlinear response of boron/aluminum laminates were analyzed using monotonic and cyclic tension and compression tests. Most recently, Becker [7] characterized the mechanical response of unidirectional boron/aluminum composites by conducting off-axis tension and compression tests and Iosipescu shear tests. The characteristics of mechanical response including elastic properties, yielding and subsequent plastic (nonlinear) response were investigated.

A relatively limited amount of experimental information is available in the open literature regarding the elastoplastic response of graphite/aluminum composites. Pepper et al [8] studied mechanical properties of different types of unidirectional graphite/aluminum composites under tension and compression loading. Various specimens composed of different types of aluminum alloy matrix were investigated. The effects of different fabrication conditions were also considered. In 1977, Hoover [9] carried out four-point bending tests to measure tensile and fracture toughness properties of unidirectional graphite/aluminum composites. In this work, longitudinal and transverse response and fracture toughness were analyzed, and the test results were subsequently compared with those of boron/aluminum composites. Pfeifer et al [10] characterized the mechanical properties of

unidirectional Thornel T-50 graphite fiber/201 aluminum composites at room and elevated temperatures in the range 300°F to 900°F. Tension and compression tests were performed on various off-axis fiber orientations. Elastic properties and ultimate strengths were measured, and the effect of test temperature was also investigated. In 1981, the same materials were studied by Tribendis [11]. The author investigated the effects of fiber orientation and thermal treatment on the mechanical properties using off-axis tension and Izod impact tests. The obtained tensile strengths were compared with Azzi-Tsai and Kelly and Davies theories [45,46]. In the above mentioned investigations, elastic properties and ultimate strengths were emphasized, but no detailed study of yielding and subsequent plastic response was discussed. Recently, Fujita [12] conducted off-axis tension and Iosipescu shear tests on Thornel P100-2K graphite fiber/6061 aluminum unidirectional composites at four test temperatures, -150°F, 75°F, 250°F and 500°F. In this work, complete in-plane elastic properties were obtained, and the effects of test temperature were also analyzed. In addition, yielding and subsequent plastic response were presented. A similar investigation was performed by Starbuck [13] on the same material under compressive loading.

Theoretical studies of the elastoplastic response of metal matrix composites have been performed by numerous researchers using micromechanics analyses. Hill [14,15] pioneered the discussion of the inelastic behavior of fiber-strengthened materials with the aid of a self-consistent scheme. In these studies, the inelastic response was expressed in the form of instantaneous plastic moduli. In 1966, Mulhern et al [16] considered the response of a circular cylindrical elastic fiber coated by elastic-plastic matrix obeying Tresca's yield condition and associated flow rule. Analytical solutions for the uniform extension of the composite cylinder were given, and good qualitative agreement with the experimental results of an aluminum-silica system was obtained. Adams [17] employed the finite element method to analyze inelastic response of unidirectional composite under transverse loading. In this investigation, two types of representative arrays, rectangular and hexagonal, were considered, and Prandtl-Reuss flow rule was utilized. The influence of local yielding and failure on the overall response were discussed in detail. In 1972, the same numerical technique was employed by Lin et al [18,19] to investigate the elastic-plastic response of unidirectional composites

under longitudinal loading, and initial yield surfaces under combined longitudinal, transverse normal and longitudinal shear loading. The finite element micromechanical formulation was also employed by Dvorak [20,21] to investigate yielding in unidirectional composite under arbitrary combinations of applied composite stresses and temperature changes, and by Foye [22] to study post-yielding behavior of composite laminates. The above finite element investigations have demonstrated sufficiently accurate characterization of stresses in the representative volume element to relate the influence of stress concentration and yielding in the constituents to the overall response of the composite. However, this numerical technique is time-consuming and expensive. In order to reduce the computational costs, a simplified continuum theory for axisymmetric plastic deformation of fibrous composites was proposed by Dvorak et al [23]. In this theory, the composite material was modeled by a single composite cylinder consisting of an elastic fiber and a von Mises nonhardening matrix. The results were compared with the finite element plasticity solution and good agreement was demonstrated for a number of axisymmetric loading situations. However, the theory could not be generalized in a simple manner to general (nonsymmetric) loading situations.

Recently, Aboudi [24-27] proposed a micromechanics model which consists of a doubly periodic array of unidirectional rectangular fibers embedded in the matrix phase. In this model, the representative volume element consists of a single fiber and three matrix subcells. Using a first order displacement expansion in each subcell of the representative volume, a continuum theory was developed. In this theory, the effective overall behavior of the composite is established on the basis of average stress-strain relations of the representative volume element. In this manner, no tedious and high-cost computation is required, and a sufficiently accurate stress-strain response of the composite can be obtained. In application, the determination of the response of composites can be performed for arbitrary loading conditions. When it is incorporated with Bodner's unified plasticity theory [36], no yielding criterion, loading or unloading condition need to be specified. These features of Aboudi's theory yield an efficient and convenient model in characterizing the elastoplastic behavior of metal matrix composites. Using this model, closed-form constitutive equations for the prediction of the overall behavior of unidirectional fiber-reinforced composites

have been developed [28]. Good agreement between prediction of this model and experimental and numerical results has been obtained [25 , 29]

A general survey and discussion of the various micromechanics based analyses of the elastoplastic response of composites can be found in the review paper by Pindera [30].

1.3 Objectives and Outline of the Present Study

The present study is an extension of Fujita and Starbuck's investigation of the elastoplastic response of unidirectional graphite/aluminum [12,13]. The objective of this study is to examine further material response of the graphite/aluminum system investigated by the above authors under combined tension-compression cyclic loading conditions at different test temperatures. This includes the investigation of the Baushinger effect, subsequent yield surface, plastic strain accumulation and influence of different loading paths. To achieve this, a combined tension-compression test fixture has been designed and employed to conduct cyclic tests on unidirectional P100/6061 graphite/aluminum specimens at three different temperatures. The experimental results generated by previous workers and the present testing program are subsequently compared with the predictions of the micromechanics analysis proposed by Aboudi.

The outline of the present study is as follows. In Chapter 2, the experimental technique, which includes the design of a combined tension-compression cyclic loading fixture, experimental methodology and set-up of testing apparatus, is described. The test results, discussion and comparison with the results of monotonic tension and compression tests performed by Fujita and Starbuck are given in Chapter 3. Chapter 4 provides a brief outline of Aboudi's micromechanics model, and the correlation of analysis and experiment. The phenomena observed in the experiment

and the comparison between analytical and experimental results are discussed in Chapter 5. In Chapter 6, the conclusions and recommendations for further studies are given.

Chapter 2 Experimental Methodology

2.1 Introduction

The objective of the present test program is to conduct combined tension-compression cyclic loading tests on an unidirectional metal matrix composite. In order to perform these tests, a special combined tension-compression cyclic loading fixture was designed and characterized using 6061-O aluminum specimens. The metal matrix composite investigated in the present study is unidirectional P100/6061 Graphite/Aluminum composite which is composed of Thornel P100-2K high strength graphite fibers and 6061 aluminum matrix. For investigating the elastoplastic response of this material, two specimen configurations, 15° off-axis and 90° fiber orientations (see Fig. 2.1), have been selected based on the results obtained by Fujita and Starbuck. These configurations have been chosen because of their significant nonlinear response. Two opposite loading cycles, tension-compression-tension and compression-tension-compression, have been applied to each specimen configuration to investigate the influence of loading path. In order to examine the effects of temperature on the mechanical response, these tests have been carried out at the three different temperatures, -150°F, room temperature and 250°F. The test matrix for this

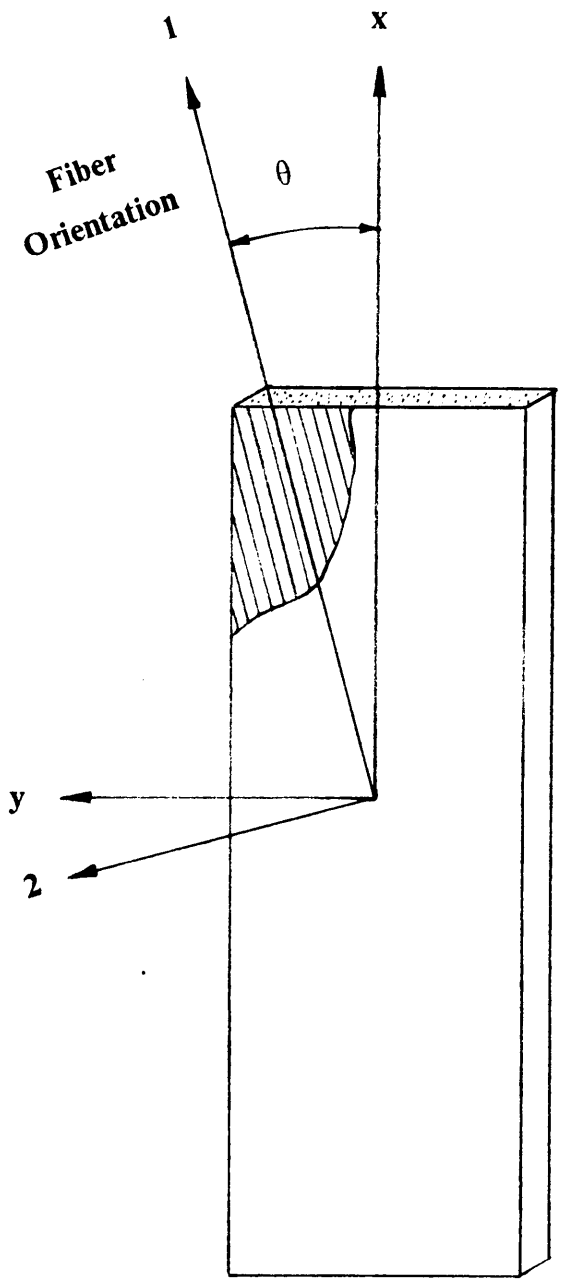

Figure 2. 1. Specimen coordinate system.

investigation is outlined in Table 2.1. Detailed description of the test program is presented in the following sections.

Table 2.1 Test Matrix (Unidirectional Gr/Al Composites)

Testing Temperature	Fiber Orientation	Type of Loading (# of Specimens) Cycle A*	Cycle B**
Low(-150° F)	15°	2	1
	90°	2	2
Room	15°	2	2
	90°	2	2
Elevated(250° F)	15°	2	2
	90°	2	2

* Cycle A: Tension - Compression - Tension
** Cycle B: Compression - Tension - Compression

In Section 2.2, the design of the combined loading fixture is outlined, and the set-up of the fixture is subsequently described. The characterization of the fixture is discussed in Section 2.3. In Section 2.4, material system, specimen preparation and instrumentation are described. In Section 2.5, test procedure, experimental apparatus and data acquisition are presented. The set-up for elevated and low temperature tests is given in Section 2.6. Finally, the analysis of the end-constraint effects in testing off-axis coupons is discussed in the closing section.

2.2 Design of the Tension-Compression Fixture

Promising test fixtures for investigating the elastoplastic response of unidirectional composites under tension, compression, and shear loading have recently been developed. Among those, Pindera's tension fixture, which allows a tensile coupon to rotate to reduce end-constraint effects has shown good results for longitudinal, transverse and off-axis loading conditions [31]. Gurdal's compression fixture, which gives sufficient side support to prevent a thin specimen from buckling has yielded promising results as well [32]. However, no suitable fixture design is available for investigating the nonlinear response of unidirectional composites under combined tension-compression cyclic loading. For such loading situations, a special combined tension-compression loading fixture has been designed in the course of the present study by incorporating the various features of the above two fixtures. The requirements for combined tension and compression loading situations make the design of the fixture fairly complicated.

The fixture is composed of the following components : grips, tension bolts, side support plates, wedges, guide rods and housing blocks. The grips (Fig. 2.2a), which have center holes and side slots to locate tension bolts and side support plates, hold the specimen in place. The tension bolts (Fig. 2.2b) slide into the center holes of the grips to transmit the load to the specimen in tension loading and align the grips in the fixture. To prevent the specimen from buckling in compression loading, the side support plates (Fig. 2.2c) are located in the side slots of the grips to give continuous side support to the specimen. They are brought into contact with the specimen by small screws shown in Fig. 2.2d. In order to support compression loading, the wedges (Fig. 2.2e) are pushed into the bottom and the top gaps between the grips and the housing blocks, and are fixed in position by two bolts (Fig. 2.2f). The contact surfaces of the wedges and grips are tapered to eliminate play between the wedges, grips and housing blocks. Four guide rods with four linear bearings shown in the assembly picture (Fig. 2.3) are employed to assure the alignment of the loading. All components described above are positioned in the housing blocks. Fig. 2.3 shows the assembly of the fixture.

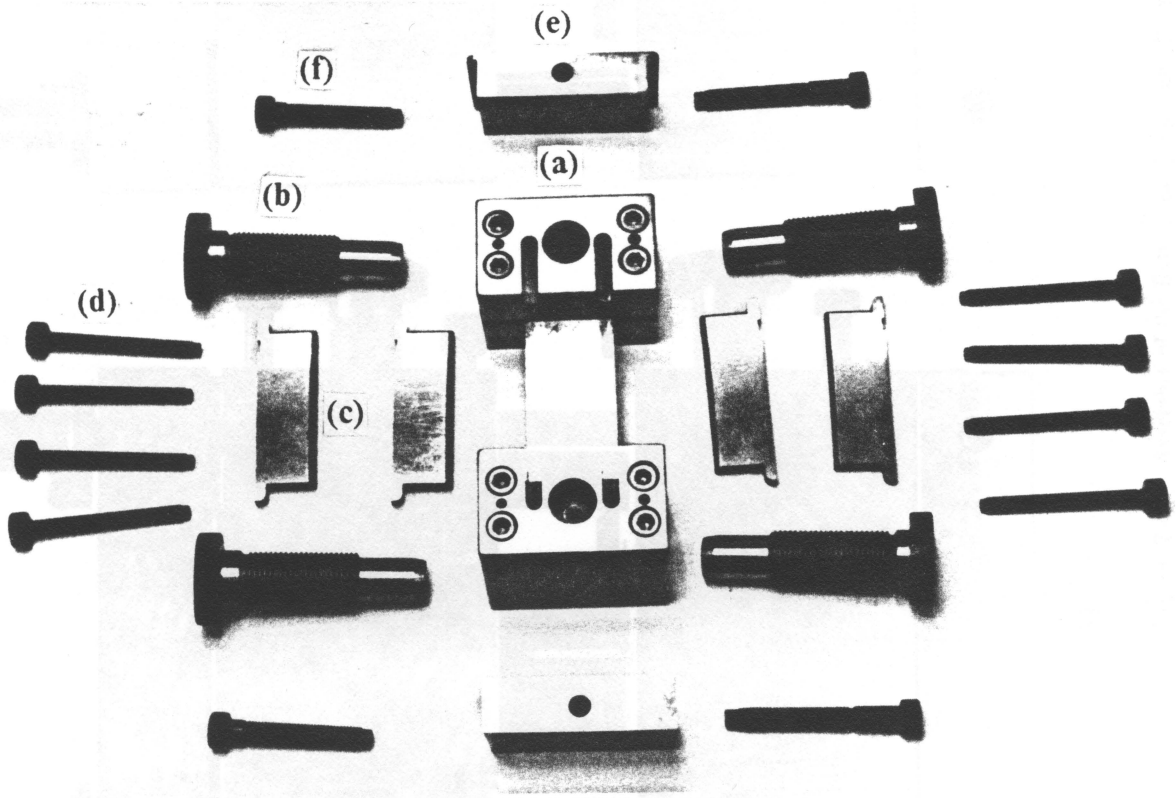

Figure 2. 2. Components of the fixture.

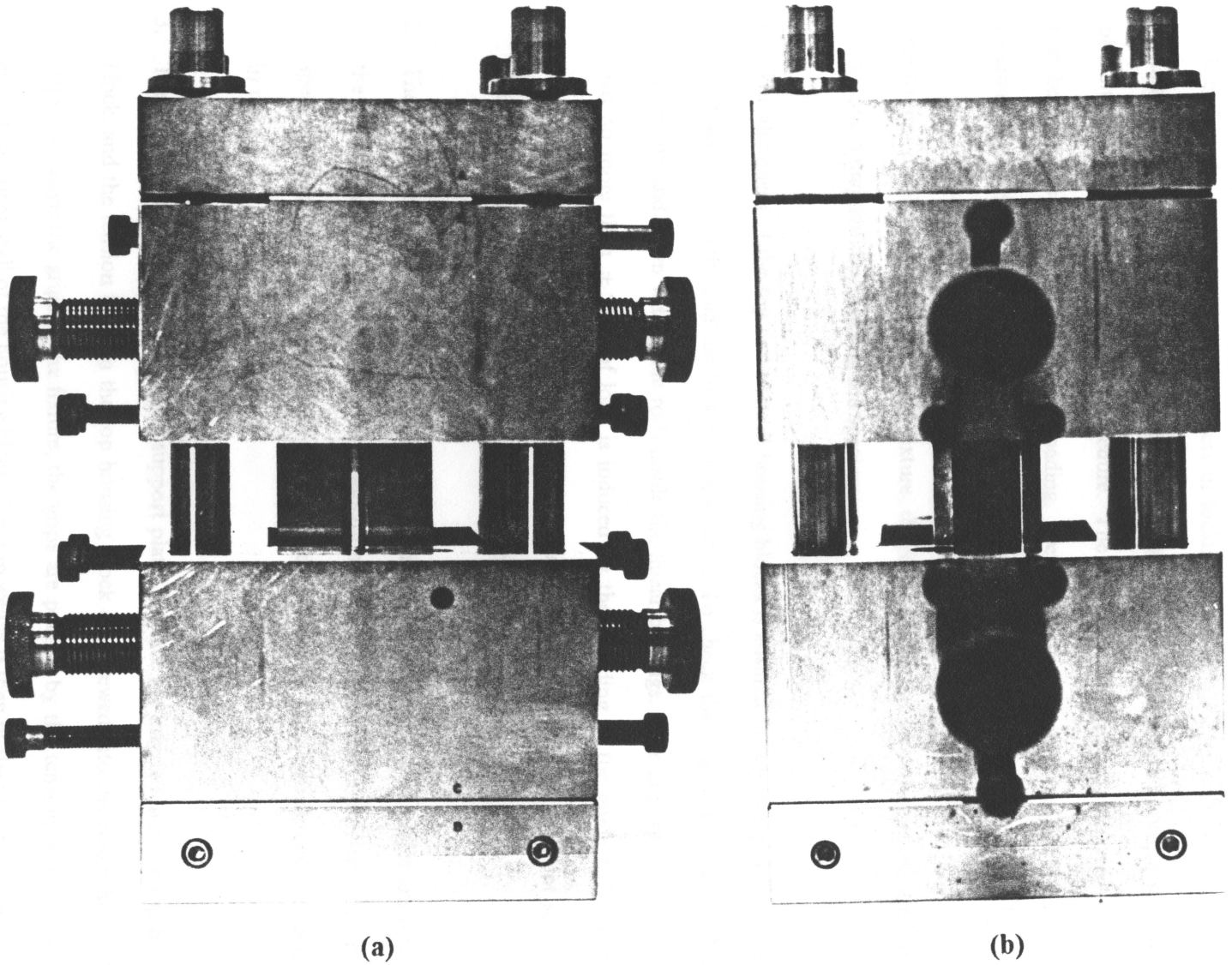

Figure 2. 3. Assembly of the fixture: (a) front view, (b) side view.

A bidirectional joint is used to transmit the load from the testing machine to the fixture, both in tension and compression. The joint consists of two pins perpendicular to each other, located at each end of the loading rod, and two sets of locking screw nuts. The pins can be adjusted to eliminate possible misalignment of the center lines of the crosshead and the bottom support plate of the testing machine during set-up procedure. The locking screw nuts are employed to eliminate play between the joint while in reversal loading. Detailed set-up procedure of the fixture and the specimen is described below.

Due to the complicated structure of the fixture, the following set-up procedure is required to align the specimen and avoid preloading the specimen.

1. The alignment of the top and bottom housing blocks is ensured by adjusting the bidirectional joint and then tightening the locking screw nuts. To check the alignment, the crosshead is moved up and down with guide rods inside the linear bearings. It is important to make sure that no more than ± 5 lbs of load is induced by the binding of the guide rods and linear bearings due to misalignment. If the induced load is more than ± 5 lbs, the joint screw nuts must be loosened and the top and bottom housing blocks be realigned.

2. The specimen is subsequently installed in the grips and the side support plates are placed in the slots of the grips with the aid of an installation frame. This installation frame prevents the specimen from being twisted while it is tightened and ensures the alignment of the specimen in the grips.

3. The grips with the specimen and side support plates in place are inserted into the top housing block, and the tension bolts in the top housing block are screwed into the center holes of the grips. To align the grips in the fixture, the grips are pushed by the tension bolts all the way against the inner wall of the housing block. The top wedge is then pushed into the gap between the grip and the housing block.

4. The crosshead is moved downward until the bottom grip is at the correct location where the centers of the tension bolts and the center holes of the bottom grip are aligned. The tension bolts in the bottom housing block are then screwed into the center holes of the bottom grip. The crosshead is moved upward until the tension bolts and the center holes of the grip are in perfect contact. This induces tension in the specimen. By monitoring the load cell channel, the tension load can be minimized.

5. The bottom wedge is pushed into the gap between the bottom grip and the bottom housing block. This procedure induces compression in the specimen. By monitoring the load cell channel, the crosshead is moved upward in order to zero the load on the specimen. Because no more than 5 lbs of load should be applied to the specimen in tension or compression in the course of moving the crosshead or adjusting the bottom wedge, the above procedure needs to be repeated several times until the bottom wedge is firmly inserted.

2.3 Characterization of the Fixture

As a first step, the combined tension-compression fixture was characterized using 6061-O aluminum specimens, which are isotropic and relatively soft. Three different loading tests, namely monotonic tension, monotonic compression and combined tension-compression cyclic loading, were carried out for this procedure. The specimens were 1″ wide and 4″ long with 1.75″ gage length. For monotonic tension and monotonic compression tests the specimen thickness was 0.04″ , and for combined tension-compression cyclic test the specimen thickness was 0.08″. A 45° rectangular rosette and uniaxial gage were mounted in a back-to-back fashion at the center of the specimen to measure in-plane strains (detailed experimental methodology and testing apparatus will be described in Section 2.4). The test results are presented and discussed below.

Due to the critical problem of buckling in testing specimens with high aspect ratio in compression, the ability of the fixture to prevent the specimen from buckling was characterized first. Monotonic compression tests were carried out on initially flat specimens, and the resulting stress-strain curves are illustrated in Fig. 2.4. In this figure, the solid curve represents data recorded by the front gage and the dashed curve represents data recorded by the back gage. It is observed that the strain readings from the front and back gages are quite close up to -1% strain. Apparently, the bending effects in compression loading are within an acceptable range up to -1% strain. Therefore it is concluded that the side support plates, which give continuous side support to the specimen, successfully prevent the relatively soft aluminum specimen from buckling.

The results of monotonic compression tests carried out with the combined tension-compression fixture are compared with those obtained using Gurdal's compression fixture in the lower portion of Fig. 2.5. The geometry of the specimen tested in the compression fixture was 1″ x 1.5″ x 0.04″ which is very similar to the specimen geometry used in the combined tension-compression fixture. It is seen that up to -1% strain, the stress-strain curves obtained with the two fixtures are essentially identical. The differences observed at higher strain levels could be caused by bending effects and initial curvature of the specimens.

To characterize the performance of the fixture in tension, the results of monotonic tension tests are compared with the results obtained using Pindera's tensile fixture. The geometry of the specimen tested in the tensile fixture was 0.5″ x 6″ x 0.04″, which gives an aspect ratio of 12. The comparison of the resulting stress-strain curves is plotted in the upper portion of Fig.2.5. It is evident that two curves are initially identical with a slight difference observed in the nonlinear response. This difference could be due to friction induced by side support plates and end constraint effects in the short specimen tested in the combined tension-compression fixture (the end constraint effects will be discussed in Section 2.7). From these comparisons, it is concluded that the combined tension-compression fixture performs well both in monotonic tension and monotonic compression loading of an isotropic material, and the results are reliable.

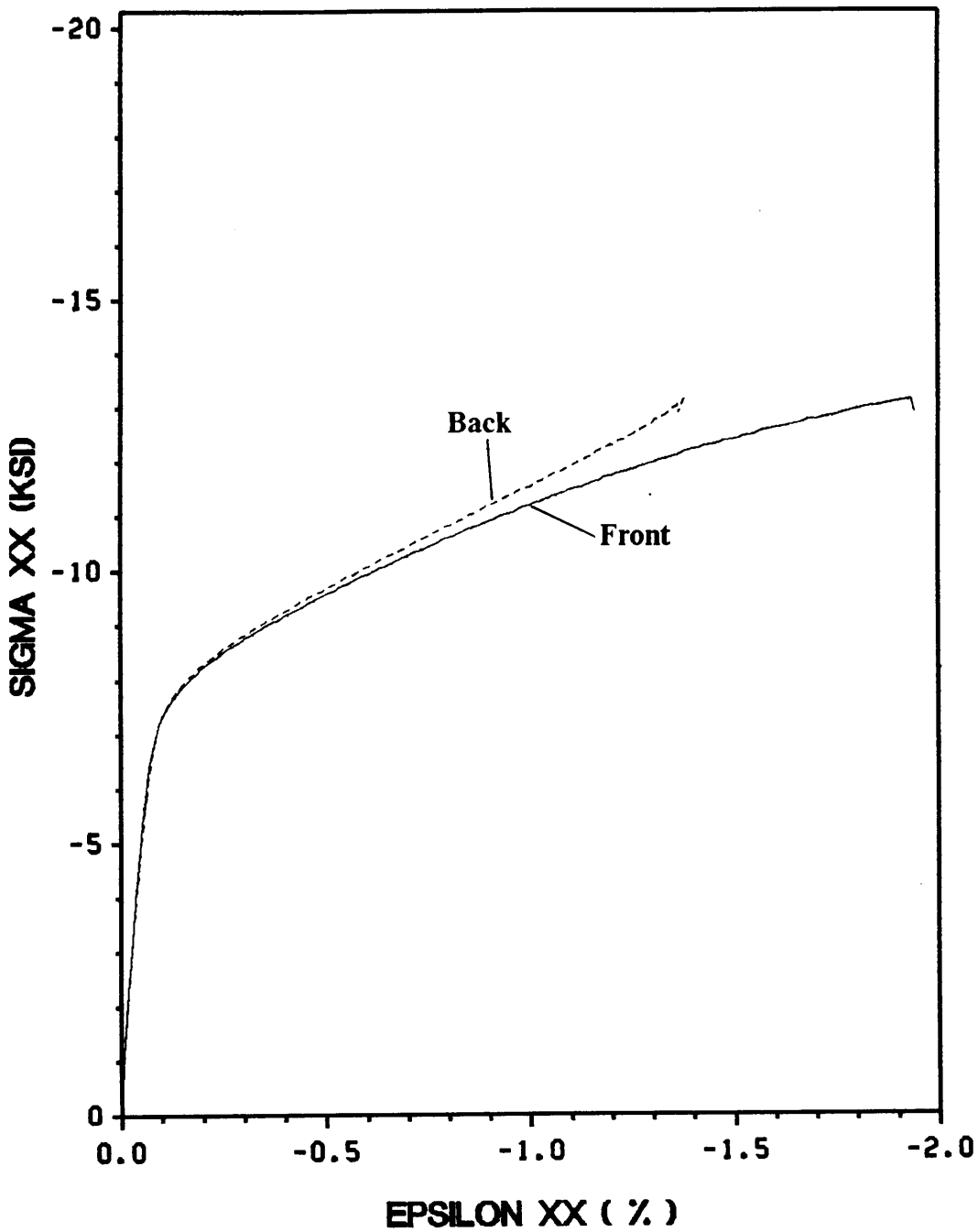

Figure 2. 4. Stress-strain curves of 6061-O aluminum specimen under monotonic compression loading.

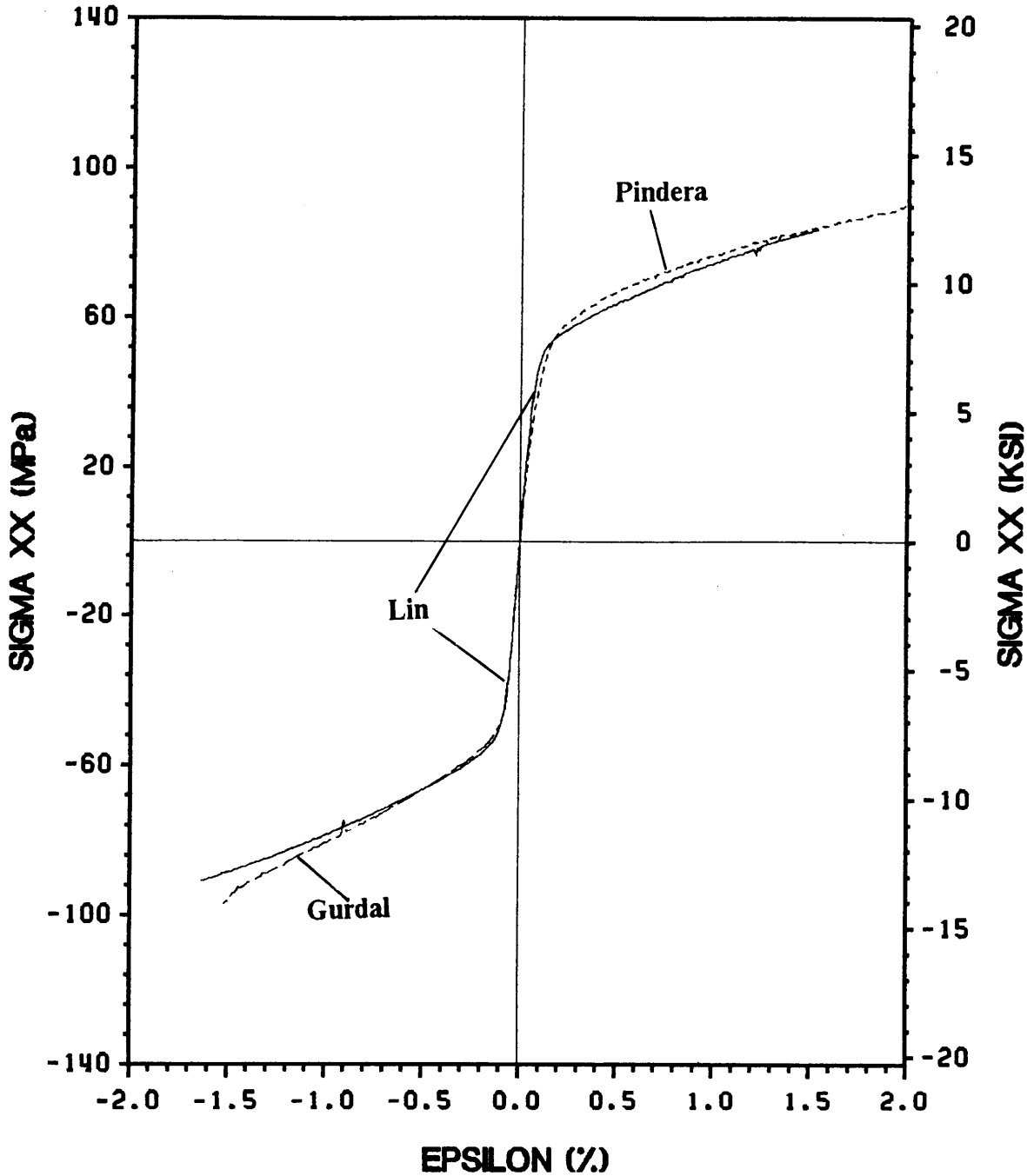

Figure 2. 5. Comparison of the test results of 6061-O aluminum specimen from different fixtures.

To characterize the performance of the fixture in combined tension-compression cyclic loading, a 1″ x 1.75″ x 0.08″ specimen was tested. The resulting stress-strain curve is presented in Fig. 2.6. It is seen in the figure that at unloading points, the curve has sharp corners and there are no kinks when the stress changes sign. Moreover, the linear portions of the resulting stress-strain curve are parallel to each other. Therefore, it is certified that the fixture can carry out the desired combined tension-compression cyclic loading without any difficulties at crucial unloading and reversal loading conditions.

On the basis of the outlined design and subsequent characterization of the developed tension-compression fixture, the following features of the fixture can be summarized:

1. The side supports give sufficient support to the specimen and appear to induce little friction.

2. Simple specimen geometry is employed; no tabbing of the specimen is required. This makes specimen preparation relatively easy.

3. Specimens of variable thickness and length can be accommodated by the fixture.

4. The applied load is aligned with the specimen by guide rods and linear bearings, both in tension and compression.

5. The results of the characterization tests illustrate the working capability of the fixture under combined tension-compression cyclic loading conditions.

These attractive features make the fixture practical in testing. However, care and some practice are needed during the set-up procedure due to the complex structure of the fixture. One shortcoming of the fixture is that the most attractive feature of Pindera's tensile fixture, specimen rotation, is inevitably sacrificed. This shortcoming requires a combined analytical-experimental methodology in interpreting test data obtained from highly anisotropic off-axis specimens with small aspect ratio due to the end-constraint effects [35].

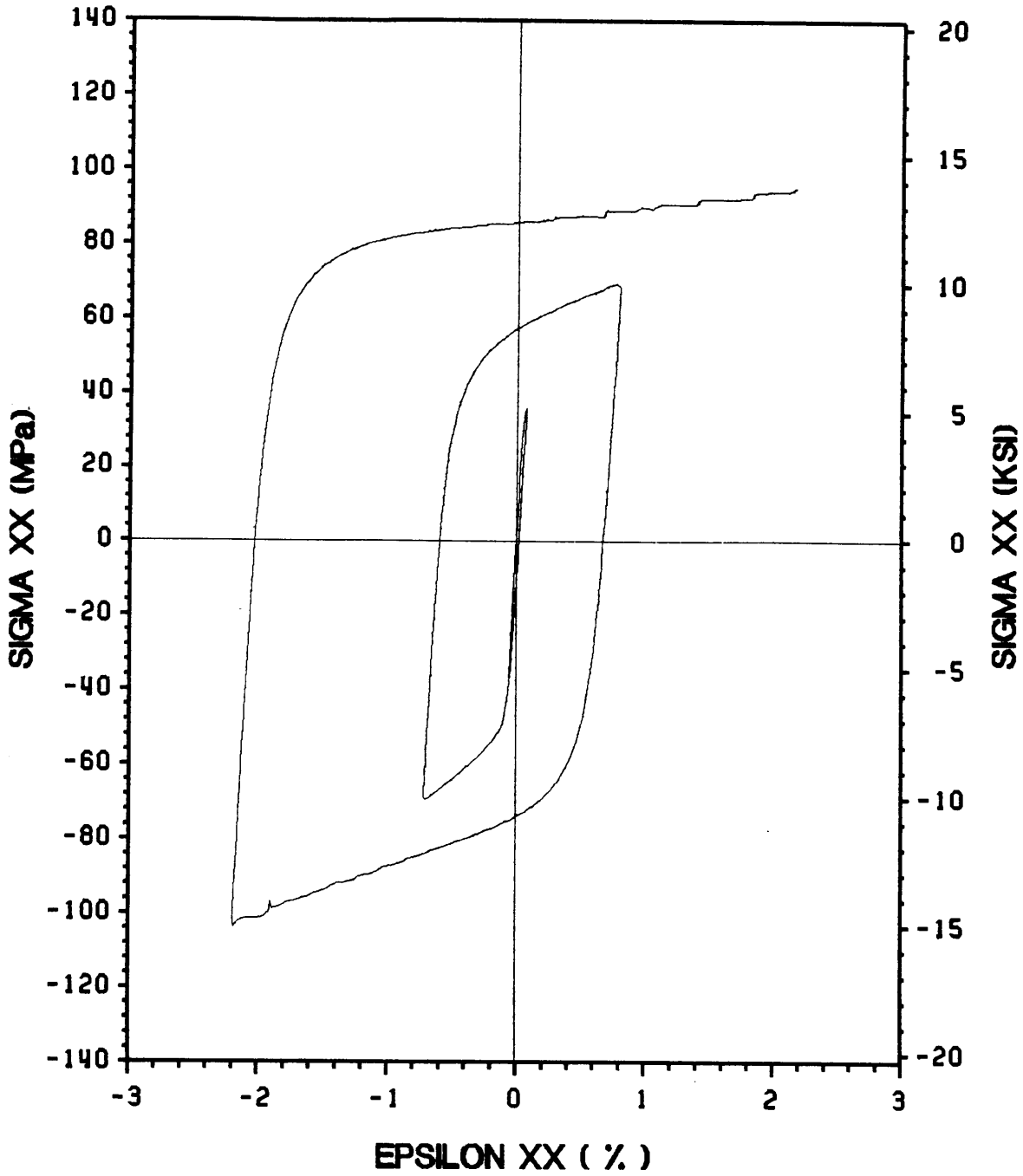

Figure 2. 6. Stress-strain curve of 6061-O aluminum specimen under combined tension-compression cyclic loading.

2.4 Material System, Specimen Preparation and Instrumentation

The material tested in this program is unidirectional P100/6061 graphite/aluminum composite which is composed of Thornel P100-2K high strength graphite fibers and 6061 aluminum matrix. The material was fabricated in panel form by liquid phase vacuum hot pressing method. The unidirectional composite panel consists of two layers of precursor wire, composed of P100-2K graphite fibers and 6061 aluminum, which are sandwiched between two 6061 aluminum sheets. The average fiber volume fraction of the panel was 47%. General description of the manufacturing process of the material was given by Fujita in reference [12].

As a first step in characterizing the material, the microstructure of the composite was examined using a metallographic microscope. A sample specimen was cut from a selected panel, polished by Al_2O_3 powder up to 0.05 μ and subsequently examined. The micrograph of the microstructure of the material in transverse section (perpendicular to fiber orientation) at 65 times magnification is shown in Fig. 2.7 (a). It is seen that very poor bonding exists at adjacent precursor wire interfaces and precursor-aluminum sheet interfaces. At the outer surface of the specimen, there are periodic indentations along the edge where two precursor wires are adjacent. The average spacing between two adjacent indentations is about 0.02 in.

The hardness of the aluminum phase within the precursor wire and along the edge was determined by Vicker's microhardness test. The results indicated that the Vicker's hardness value for the aluminum phase was about 53, with fairly close values obtained in both areas.

The microstructure of the material in the area of two adjacent precursor wires at a higher magnification is shown in Fig. 2.7 (b). It is observed that there are no visible defects at the interfaces of individual graphite fibers and aluminum matrix, and the fibers are uniformly distributed

(a)

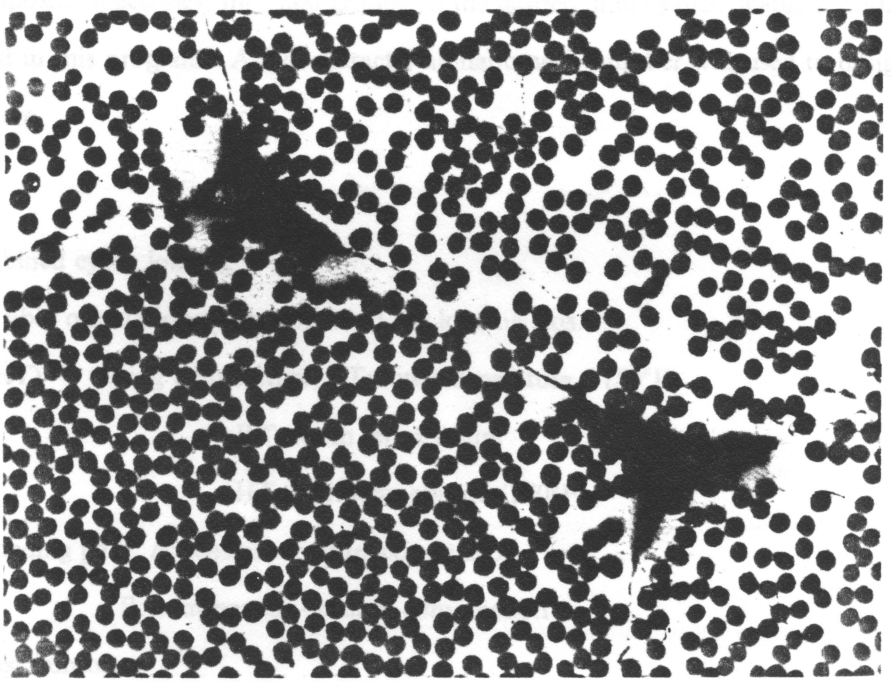

(b)

Figure 2. 7. Micrograph of the transverse cross-section of P100/6061 unidirectional graphite/aluminum composite. (a) the entire cross-section (65 X), (b) the adjacent area of precursor wires (275 X).

within the precursor wire. Voids and poor bonding at the interfaces of adjacent precursor wires are more clearly illustrated in this figure.

Since the present investigation is primarily concerned with the nonlinear response of the unidirectional graphite/aluminum composite, two specimen configurations, 15° off-axis and 90° fiber orientation, were selected due to their significant nonlinear response.

The geometry of the specimens was chosen to be 1″ x 4″ x 0.04″ with 1.75″ gage length. The chosen gage length is the same as the gage length of the 6061-O aluminum specimens for which no apparent global buckling was observed in the strain range of interest. The thickness of the specimen was dictated by the thickness of the provided panel (nominal thickness).

The specimens were cut by a band-saw from 12″ x 12″ x 0.04″ unidirectional Gr/Al panels supplied by DWA Composite Specialties, Inc., and ground to the desired dimensions. Table 2.2 outlines the specimens used in this program. A five character alphanumeric number was used to designate the specimens, where

C --- combined cyclic loading

15(90) --- fiber orientations with respect to the loading axis.

LT(RT)(HT) --- testing temperature, LT: low temperature (-150°F)
RT: room temperature
HT: high temperature (250°F)

A(B) --- loading path, A: tension-compression-tension
B: compression-tension-compression

1(2) --- Test number.

Table 2.2 Gr/Al Specimens Used in the Testing Program

Specimen Designation No.	Panel No.	Mid Cross-Sectional Area(in^2)	Average Cross-Sectional Area(in^2)
C15LTA1	G-5754	0.0407	0.0409
C15LTA2	G-5754	0.0399	0.0401
C15LTB1	G-5754	0.0386	0.0396
C90LTA1	G-5755	0.0412	0.0418
C90LTA2	G-5755	0.0402	0.0406
C90LTB1	G-5755	0.0402	0.0398
C90LTB2	G-5755	0.0401	0.0407
C15RTA1	G-5872	0.0439	0.0444
C15RTA2	G-5872	0.0441	0.0447
C15RTB1	G-5872	0.0435	0.0442
C15RTB2	G-5872	0.0433	0.0445
C90RTA1	G-5883	0.0430	0.0437
C90RTA2	G-5883	0.0440	0.0437
C90RTB1	G-5883	0.0430	0.0433
C90RTB2	G-5755	0.0401	0.0407
C15HTA1	G-5756	0.0398	0.0406
C15HTA2	G-5756	0.0400	0.0402
C15HTB1	G-5756	0.0391	0.0400
C15HTB2	G-5756	0.0407	0.0411
C90HTA1	G-5755	0.0407	0.0414
C90HTA2	G-5755	0.0397	0.0408
C90HTB1	G-5755	0.0397	0.0403
C90HTB2	G-5755	0.0387	0.0404

The mid cross-sectional area was measured at the middle of the specimen where the strain gages were mounted. The average cross-sectional area was obtained by taking the average of three different measurements of the cross-sectional area (two measurements at the each end of the specimen and one at the middle of the specimen). It is seen in Table 2.2 that the cross-section of the specimens is quite uniform.

In order to measure in-plane strains, a Micromeasurement 45° rectangular rosette (WA-13-060WR-120) was mounted at the center on one side of the specimen. On the back of the specimen, a Micromeasurement uniaxial strain gage (EA-06-062AP- 120) was installed to measure the longitudinal strain which was utilized to correct for bending effects due to initial curvature of the specimens. Fig. 2.8 shows the specimen geometry and the locations of the strain gages mounted on the specimen.

The strain gages were installed using Micromeasurement M-bond 200 adhesive following the recommended procedure of Micromeasurement Instruction Bulletin B-127-8 [41]. Because of the high anisotropy of unidirectional graphite/aluminum, the accuracy of the alignment of the strain gages mounted on the specimen becomes very important. Consequently, the misalignment of the strain gages was measured under a microscope before testing. It was found that, typically, the misalignment was less then 1° for most specimens. The small misalignment was taken into account in the course of post processing the data to obtain the actual stress-strain response.

2.5 Test Procedure, Experimental Apparatus and Data Acquisition

In the present test program, two opposite loading paths, tension-compression-tension and compression-tension-compression, were applied to each specimen configuration at three different temperatures, -150°F, room temperature, and 250°F. The reversal points for the cyclic loading tests were chosen to be 75% of the ultimate stresses of monotonic tension and compression tests generated by Fujita [12] and Starbuck [13]. The stress reversal points were above the initial yield point of each specimen orientation. Each loading condition was repeated twice except for 15° off-axis specimen under compression-tension-compression loading at the low temperature.

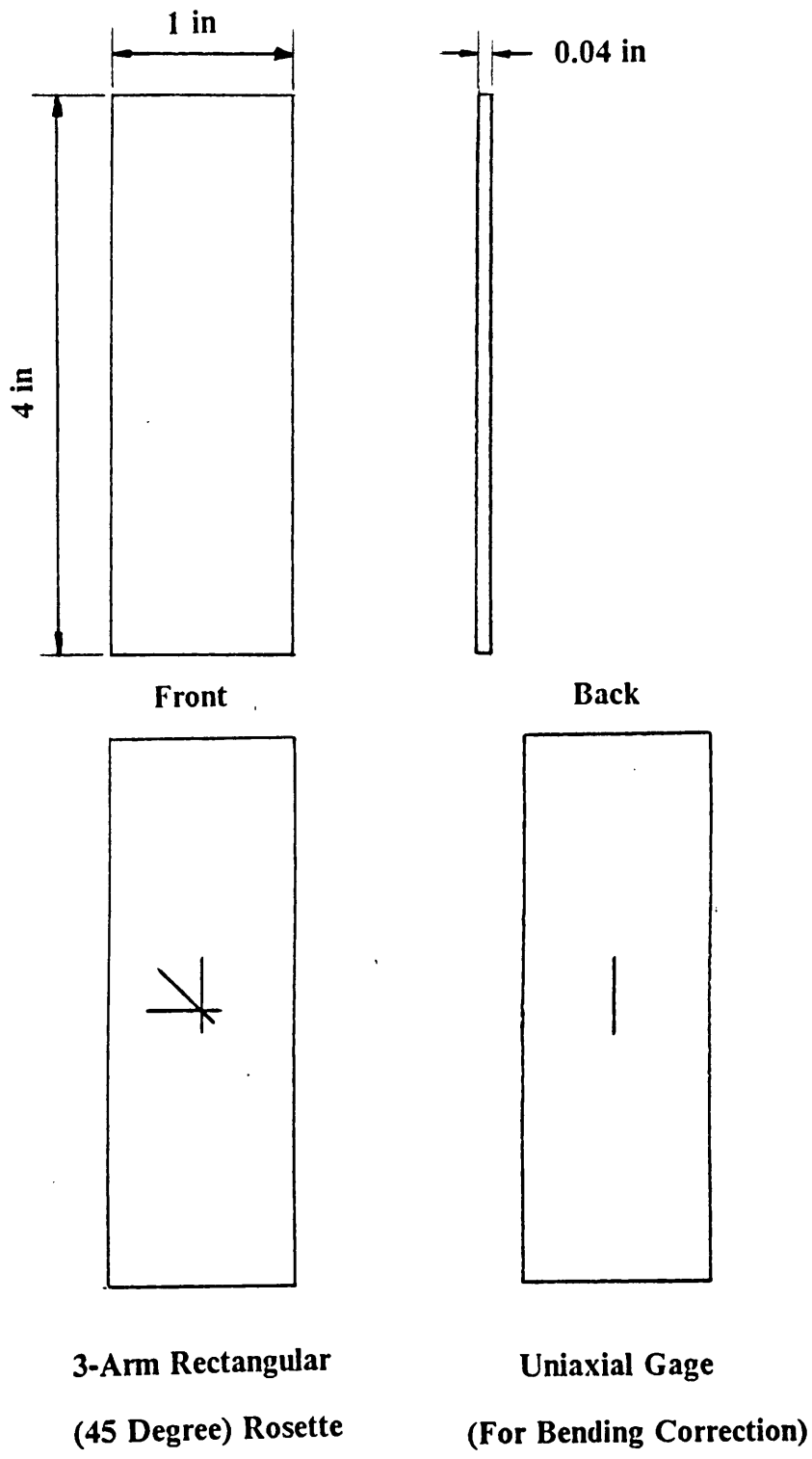

Figure 2. 8. Specimen geometry and instrumentation.

The experimental apparatus consisted of a United Testing System (UTS), Measurement Group 2120 amplifier, DATA Translation DT2805/5716 board and IBM-XT personal computer. The set-up of the apparatus is shown in Fig. 2.9. The testing machine was fully controlled by the IBM-XT personal computer. For the present tests, crosshead speed of ± 0.005 in/min was used, which yielded an average strain rate of ± 0.003 in/in/min for the employed specimen geometry.

During the test, readings from the load cell and four strain channels were recorded at the rate of three points per second per channel. The longitudinal stress, σ_{xx}, was directly calculated by dividing the applied load by the mid-point cross-sectional area of the specimen. The procedure for the calculation of the in-plane strains, ε_{xx}, ε_{yy} and γ_{xy} , is given below.

The four measured strains are ε^f_{xx}, ε^f_{yy}, γ^f_{xy} and ε^b_{xx}, where the superscript 'f' denotes the strain measurement from the rosette on the front of the specimen and 'b' denotes the strain from the uniaxial gage on the back of the specimen. Ideally, ε^f_{xx} and ε^b_{xx} should have the same values. However, due to bending and initial curvature of the specimen, these strains are usually different. Based on the assumption that the strains have a linear distribution through the thickness, bending correction is employed to determine the average in-plane strain in the following fashion:

$$\varepsilon_{xx} = \frac{1}{2}\left(\varepsilon^f_{xx} + \varepsilon^b_{xx}\right) \tag{2.1}$$

$$\varepsilon_{yy} = \frac{\varepsilon^f_{yy}}{\left(1 + \frac{B}{2}\right)} \tag{2.2}$$

$$\gamma_{xy} = \frac{\gamma^f_{xy}}{\left(1 + \frac{B}{2}\right)} \tag{2.3}$$

where $B = 2(\varepsilon^f_{xx} - \varepsilon^b_{xx})/(\varepsilon^f_{xx} + \varepsilon^b_{xx})$, is the bending correction factor.

The stresses and strains along the principal material coordinate directions are subsequently obtained by transforming the laminate stresses and strains using the following transformation relations:

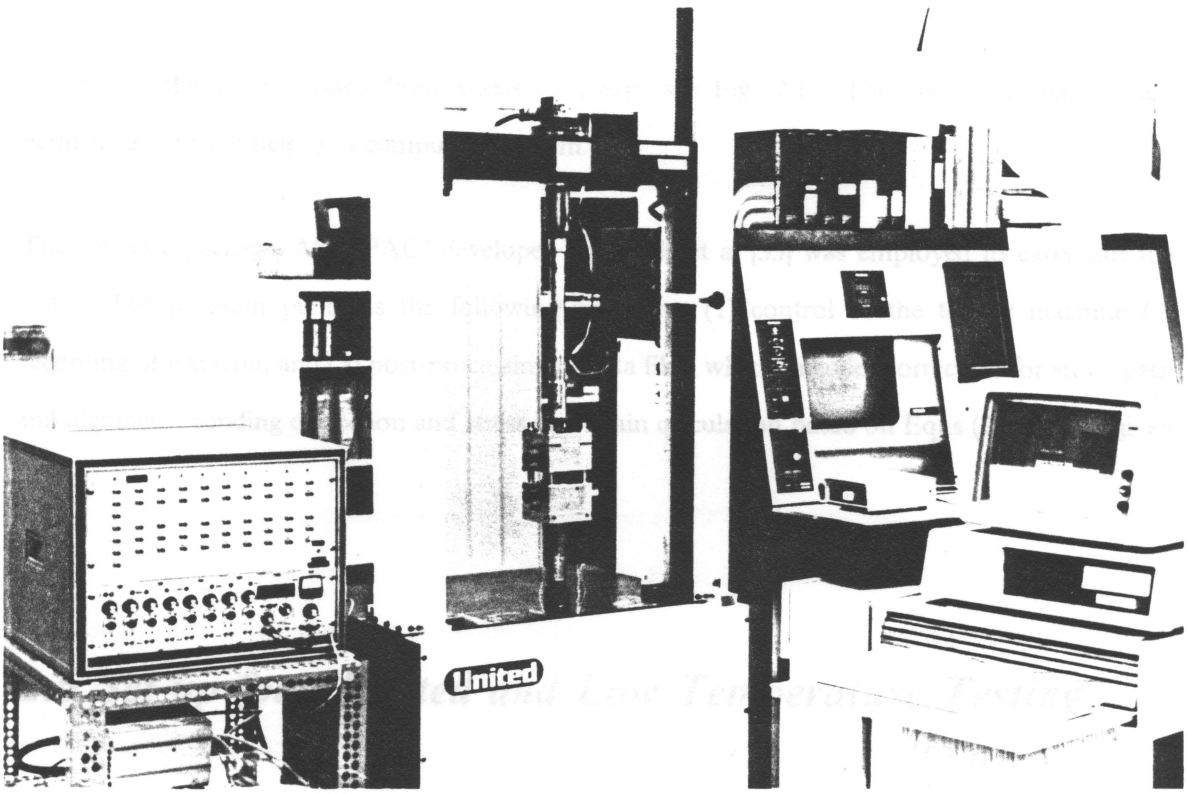

Figure 2. 9. Set-up of the experimental apparatus

$$\begin{bmatrix} \sigma_{11} \\ \sigma_{22} \\ \tau_{12} \end{bmatrix} = \begin{bmatrix} \cos^2\theta & \sin^2\theta & 2\cos\theta\sin\theta \\ \sin^2\theta & \cos^2\theta & -2\cos\theta\sin\theta \\ -\cos\theta\sin\theta & \cos\theta\sin\theta & \cos^2\theta - \sin^2\theta \end{bmatrix} \begin{bmatrix} \sigma_{xx} \\ 0 \\ 0 \end{bmatrix} \tag{2.4}$$

,and

$$\begin{bmatrix} \varepsilon_{11} \\ \varepsilon_{22} \\ \gamma_{12} \end{bmatrix} = \begin{bmatrix} \cos^2\theta & \sin^2\theta & \cos\theta\sin\theta \\ \sin^2\theta & \cos^2\theta & -\cos\theta\sin\theta \\ -2\cos\theta\sin\theta & 2\cos\theta\sin\theta & \cos^2\theta - \sin^2\theta \end{bmatrix} \begin{bmatrix} \varepsilon_{xx} \\ \varepsilon_{yy} \\ \gamma_{xy} \end{bmatrix} \tag{2.5}$$

where θ is the angle rotated from x-axis to 1-axis, see Fig. 2.1. The above calculations are performed with the help of a computer program.

The software package "MATPAC" developed by Hidde et al [33] was employed to carry out the tests. The program performs the following functions: (1) control of the testing machine (2) recording of test data, and (3) post-processing of data files, which includes correction for strain gage misalignment, bending correction and stress and strain calculation based on Eqns (2.1) - (2.5) given above.

2.6 Set-up for Elevated and Low Temperature Testing

For elevated (250°F) and low (-150°F) temperature tests, a WK-06-060WR-350 rosette and WK-06-062AP-350 uniaxial gage were used. The M-bond 600 adhesive was employed to mount the gages. The installation procedure was carried out according to Micromeasurement Instruction Bulletin B-130-10 [42]. In order to eliminate thermal effects on the strain gages and the specimen tested at elevated and low temperature, a dummy specimen with compensation gages was used [43].

An ATS 230 controller was used to control the temperature. In order to measure the temperature accurately, a thermocouple was attached to the fixture as close as possible to the specimen. Although a better set-up is to attach the thermocouple to the specimen, this set-up usually causes severe electronic noise problems. For all the tests, the temperature was controlled to within $\pm 2°F$ of the test temperature. To raise the temperature, electric heating inside the oven was used and to lower the temperature liquid nitrogen was employed.

During the heating or cooling process, the specimen, together with every element of the fixture, expands or contracts. This results in compression or tension loading of the specimen. To reduce the thermally induced loads, the IBM-XT was used to automatically move the crosshead of the machine up or down to control the thermal loading to within ± 5 lbs.

At the elevated (250°F) temperature, no binding between the specimen and the side-support plates and no binding of the linear bearings was evident. From the stress vs. time and strain vs. time plots, Fig. 2.10, it is apparent that the stress and strain increase simultaneously as the time progresses. Evidently, the loading is applied directly to the specimen, indicating that the linear bearings move smoothly along the guide rods without binding.

Unfortunately, binding problems occurred at the low (-150°F) temperature. This is shown in the stress vs. time and strain vs. time plots in Fig. 2.11. From the plots, it is apparent that the strain remains constant while the stress increases in the initial stages of loading. Apparently, the loading is not applied directly to the specimen initially. The binding takes place at two locations, one is at the contact surfaces of the guide rods and linear bearings, and the other is at the contact surfaces of the specimen and the side support plates. To solve this icing problem, two steps were taken before lowering the temperature in the oven. First, a strip of Masking tape was attached to the side support plate to prevent the specimen and side support plates from icing up. Then, the temperature in the oven was raised to 100°F and maintained for half an hour before blowing in liquid nitrogen to lower the temperature. This step reduces the moisture in the oven. From the stress vs. time and strain vs. time plots of the test which was carried out after the above steps were taken, Fig. 2.12,

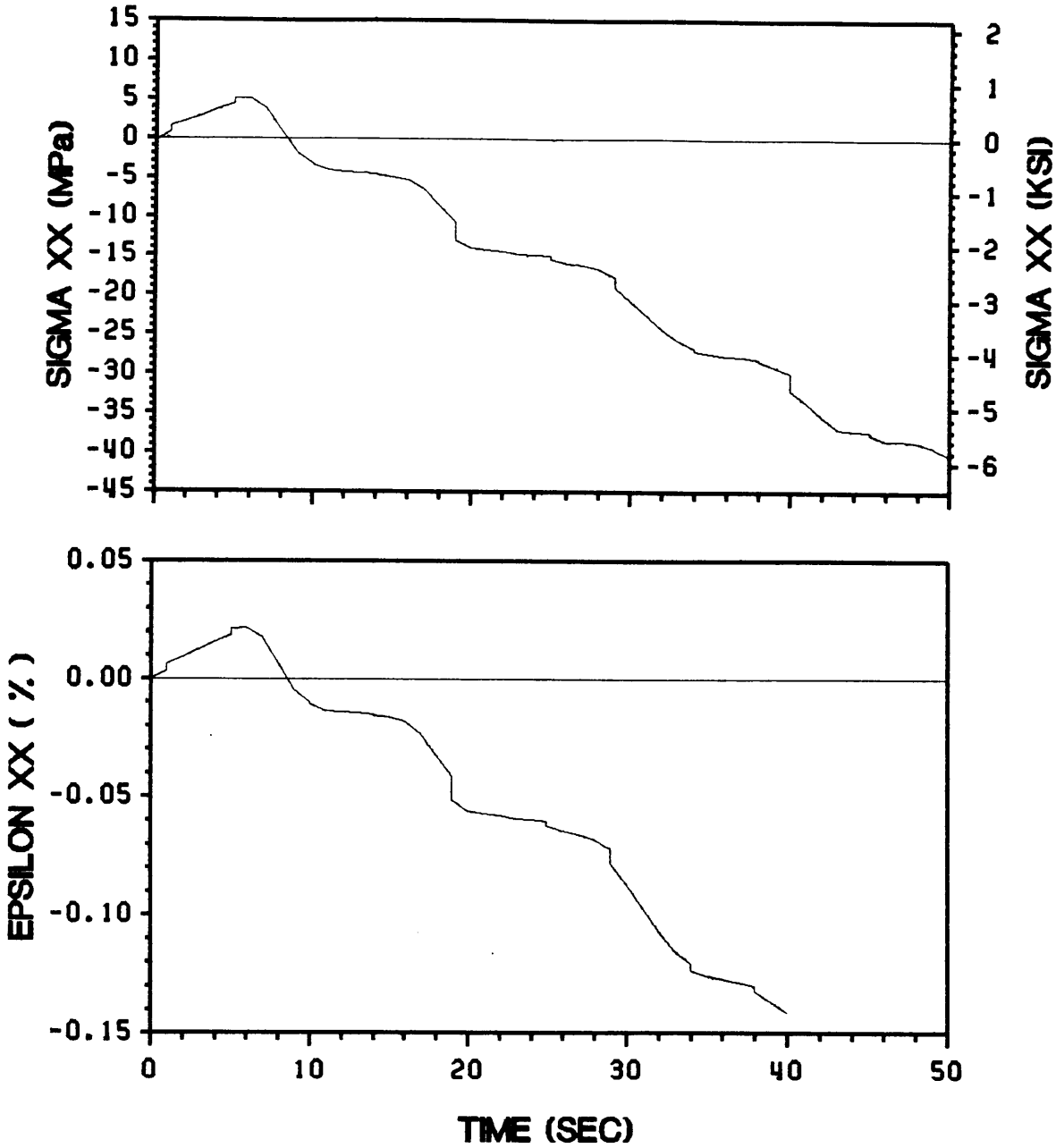

Figure 2. 10. Stress vs. time and strain vs. time plots at high temperature test

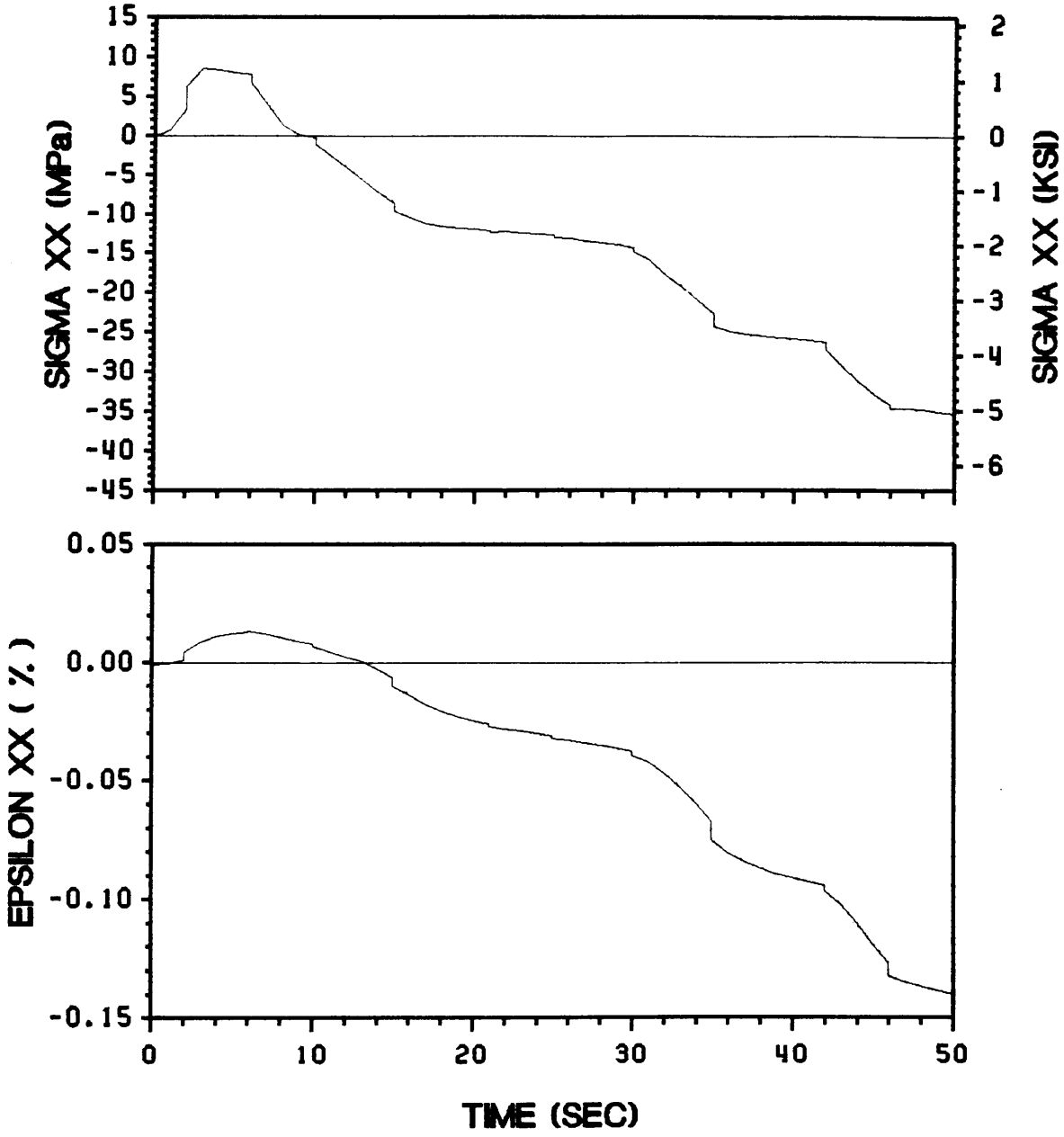

Figure 2. 11. Stress vs. time and strain vs. time plots at low temperature test with binding problem

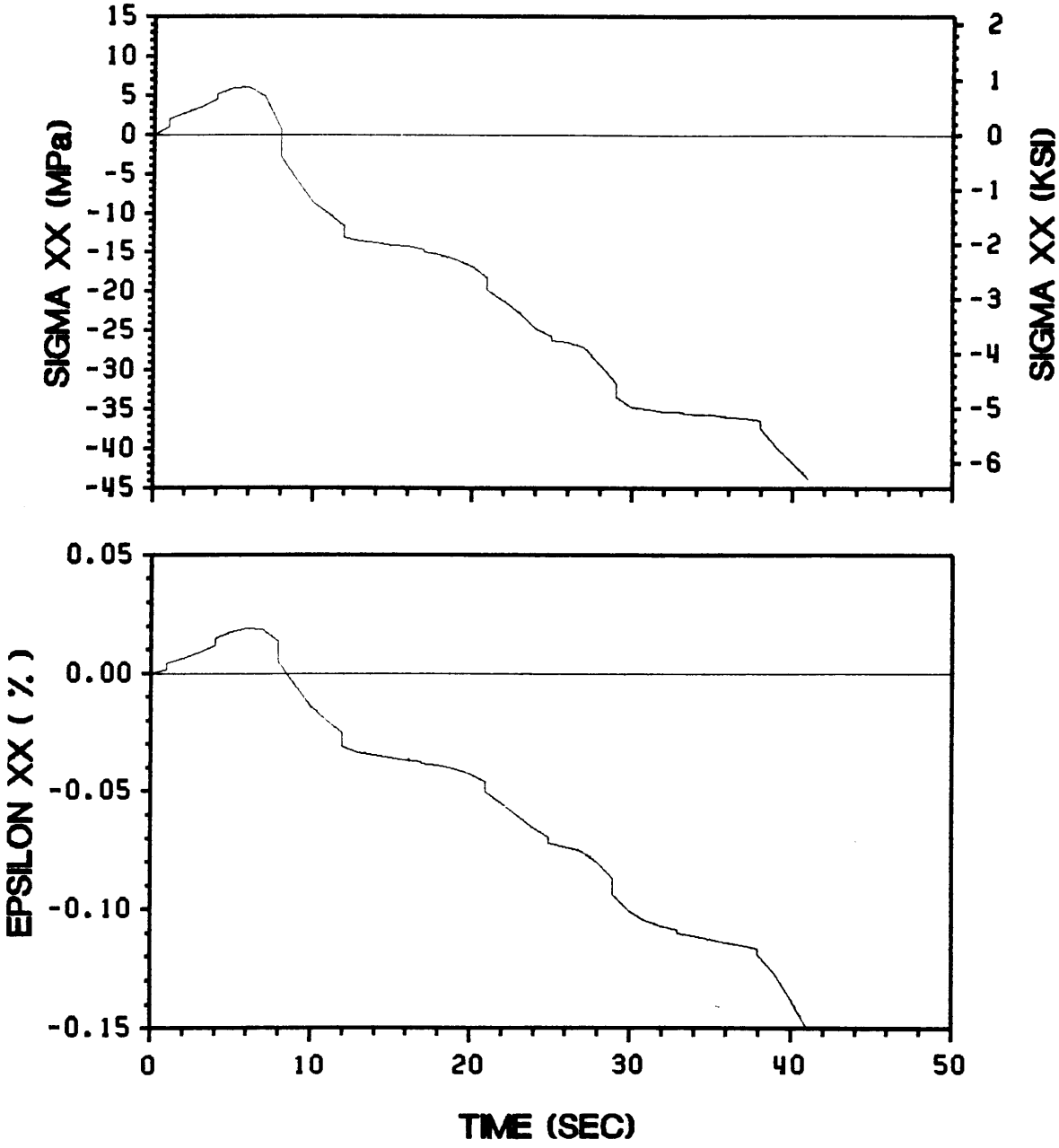

Figure 2. 12. Stress vs. time and strain vs. time plots at low temperature test without binding problem

it is seen that the stress and strain increase simultaneously, indicating that no binding is taking place. Consequently, the icing problem was overcome by the above outlined procedure.

2.7 End-Constraint Effects

For characterizing the response of a given material system, a uniform state of stress is desired in the test section of a specimen. In the case of isotropic materials, uniform states of stress can be obtained at a distance of one or two specimen widths from the clamped end [40]. However, in the case of off-axis unidirectional composites, due to the additional moment and shear forces induced by the rigid clamping, a nonuniform state of stress always exists in the specimen, Fig. 2.13. The end-constraint effects were first discussed by Pagano and Halpin [35]. Using an assumed distribution of τ_{xy} and approximate boundary conditions, Pagano and Halpin developed a model to estimate the error in determining the off-axis Young's modulus $E_{xx}(\theta)$. Due to the low aspect ratios of the specimens employed in the present study, end-constraint effects need to be carefully analyzed. In the following, the axial stress distribution across the mid-section of the specimen where the strain gages are mounted will be first examined using finite element analysis. Then, the apparent elastic constants of the tested materials will be computed. For off-axis unidirectional composites, Pagano-Halpin model prediction will also be employed to examine the apparent elastic constants.

The FORTRAN code "ANFRAC" developed at Virginia Tech was used for the finite element analysis [34]. This code is based on a standard displacement formulation using isoparametric elements. It has been developed for modeling anisotropic materials. The mesh used in modeling the tension-compression coupon is shown in Fig. 2.14. It consists of 240 elements and 525 nodes.

In order to simulate the stiffest and softest griping condition of the specimen during the test, two types of boundary conditions were applied in the FEM analysis. The first boundary condition was

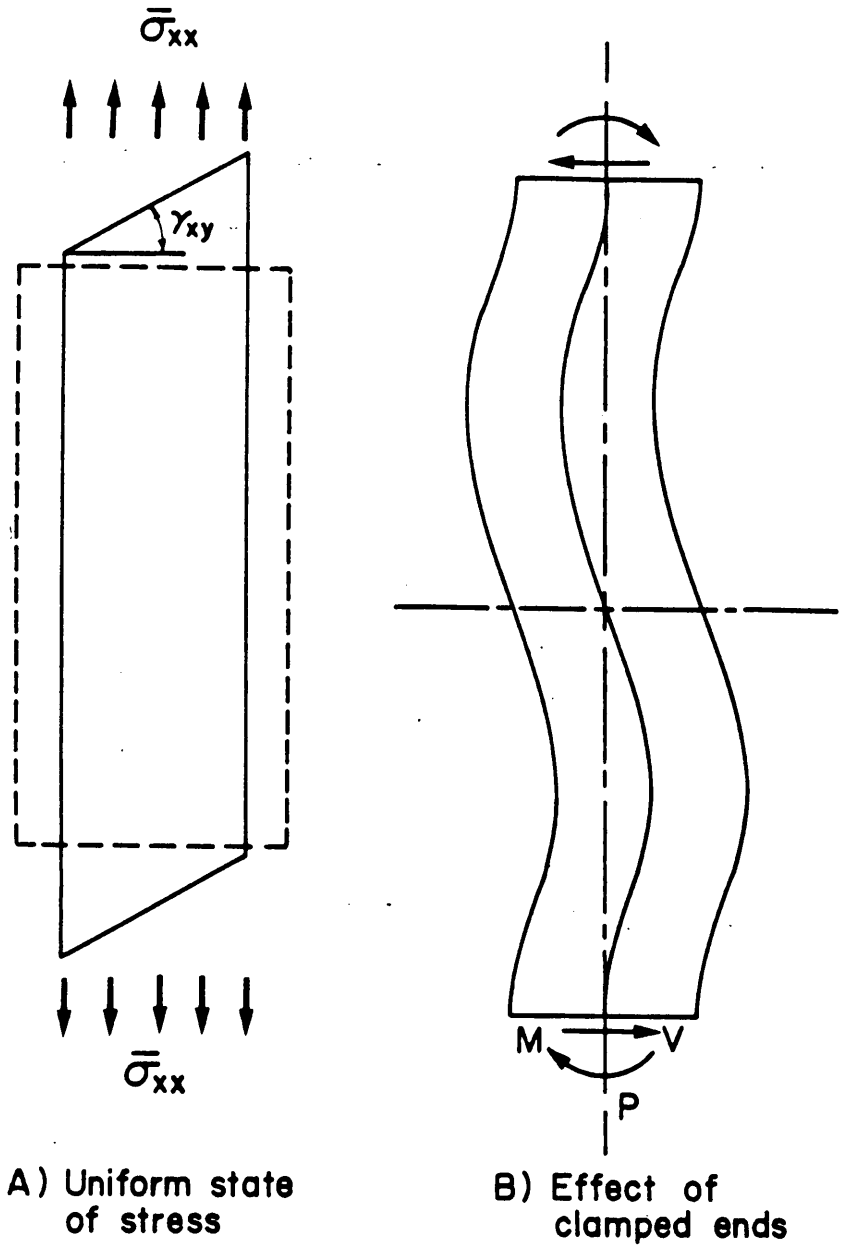

Figure 2. 13. End-constraint effects on off-axis coupon, reference [35].

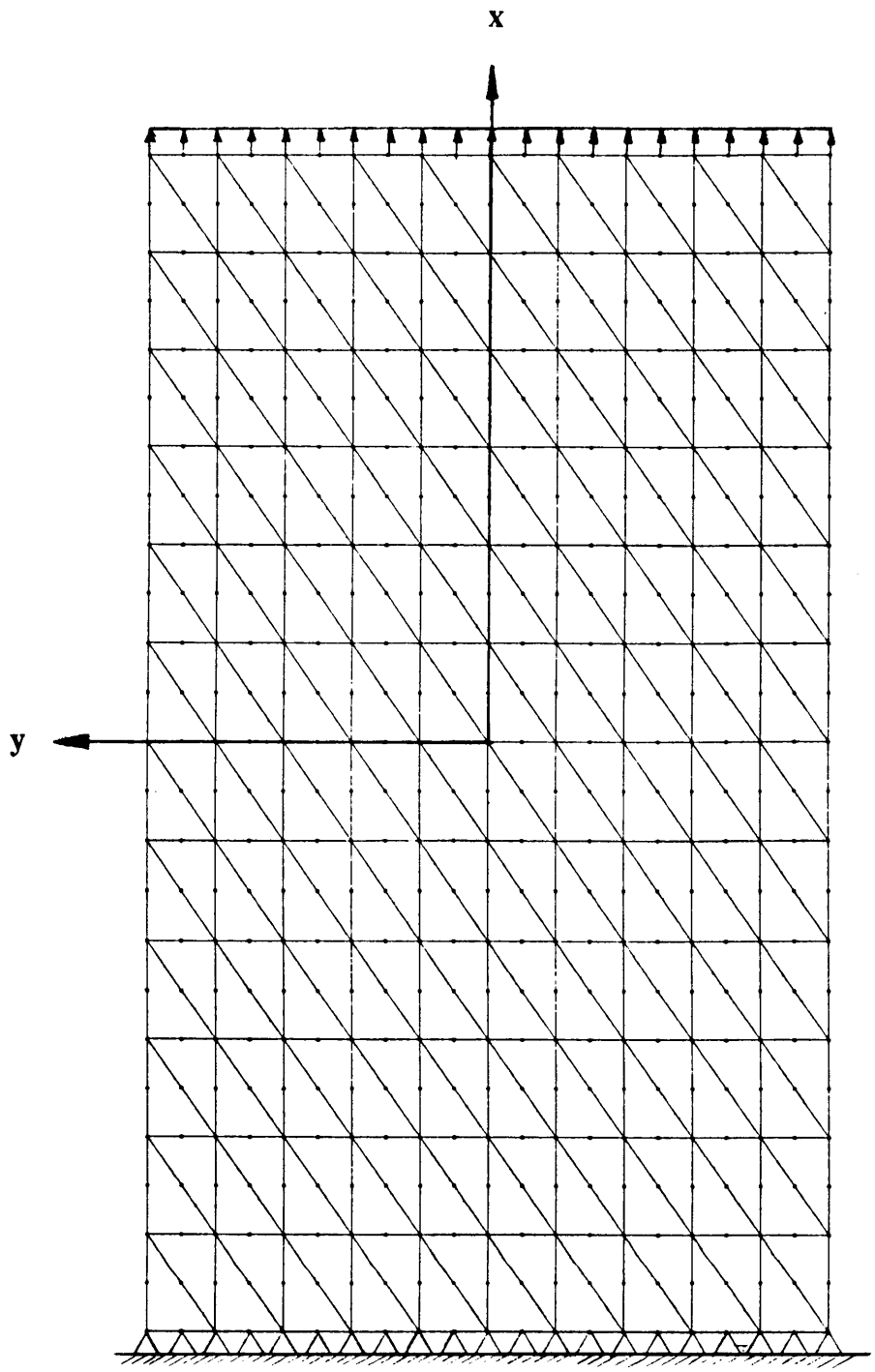

Figure 2. 14. Mesh used in the finite element analysis.

applied as follows. At the bottom, the displacements in the x- and y- direction are fixed for all 21 nodes. At the top, the displacements in y-direction for all 21 nodes are also fixed. To model the applied loading, a uniform displacement in x-direction is specified for all 21 nodes at the top of the specimen. The second boundary condition is similar to the first one except that the displacement in the y-direction both at the top and bottom are fixed only for the mid node instead of for all 21 nodes

The input material properties are listed in Table 2.3. The data were obtained from monotonic tensile tests using specimens with long aspect ratios. For the 6061-O aluminum specimen, it was generated by the author, and for Gr/Al specimens, it was generated by Fujita [12]. The in-plane shear modulus G_{12} of Gr/Al was obtained from a 45° off-axis tension coupon, because it is believed to provide a very accurate value of G_{12} [31].

Table 2.3 Input Data for End-Constraint Analysis

Tested Specimens	E_{11} (msi)	E_{22} (msi)	ν_{12}	G_{12} (msi)
6061-O Aluminum	10.0	10.0	0.33	3.14
P100/6061 Gr/Al*	58.4	3.5	0.291	2.43

* Reference [12]

The longitudinal stress distribution across the mid-section of the specimen using the two types of boundary conditions are illustrated in Fig. 2.15, where the stress has been normalized by the applied longitudinal average stress. It is clearly shown that for the 15° off-axis Gr/Al specimens, the stress distribution is highly nonuniform, whereas for the isotropic aluminum and orthotropic (90°) Gr/Al specimens uniform distribution is obtained.

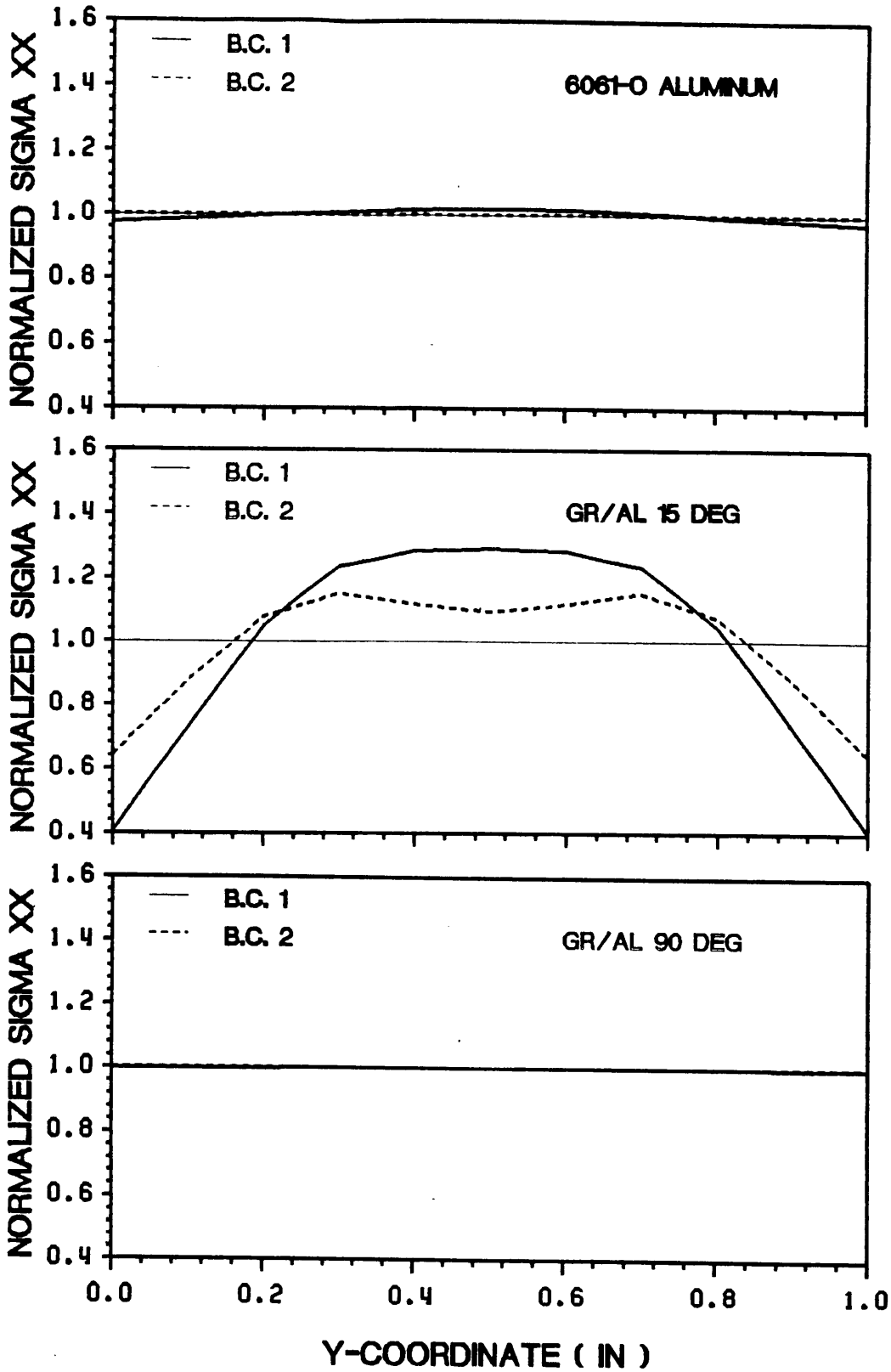

Figure 2. 15. Stress distribution along the gage section of the tested specimens.

The apparent elastic moduli of Gr/Al specimens were also computed using the same FORTRAN code. In order to simulate the actual test, the average stress was obtained by summing the applied forces at the top nodes of the specimen and dividing the resultant force by the cross sectional area of the specimen. The strains used in the calculation of the apparent moduli are the strains at the mid-point of the test section. The calculation was performed for 15° off-axis Gr/Al specimens. The results for the apparent moduli obtained from the finite element analyses using two types of the boundary conditions are presented in Section 3.2 and correlated with the experimental results.

The end-constraint effects in the off-axis tension-compression coupon were also analyzed using the Pagano-Halpin model [35]. Employing the results of Pagano and Haplin, Pindera and Herakovich [31] have shown that the error in the determination of $E_{xx}(\theta)$, $\nu_{xy}(\theta)$ and G_{12} can be expressed by the following ratios if the nonuniformity in the stress field caused by the end-constraint is neglected:

$$\frac{E_{xx}}{E_{xx}^{*}} = \frac{1-\eta}{1-\frac{2}{3}\eta} , \tag{2.6}$$

$$\frac{\nu_{xy}}{\nu_{xy}^{*}} = \frac{1+\beta\frac{\bar{S}_{16}}{\bar{S}_{11}}}{1+\beta\frac{\bar{S}_{26}}{\bar{S}_{12}}} \tag{2.7}$$

and

$$\frac{G_{12}}{G_{12}^{*}} = \frac{1}{1-\frac{2}{3}\eta}\left[1-\beta\frac{(\cos^2\theta-\sin^2\theta)}{\sin\theta\cos\theta}\right] \tag{2.8}$$

where

$$\beta = -\frac{6\left(\frac{h}{l}\right)^2\frac{\bar{S}_{16}}{\bar{S}_{11}}}{1+6\left(\frac{h}{l}\right)^2\frac{\bar{S}_{66}}{\bar{S}_{11}}} \tag{2.9}$$

and

$$\eta = -\frac{6\left(\frac{h}{l}\right)^2\left(\frac{\bar{S}_{16}}{\bar{S}_{11}}\right)^2}{1+6\left(\frac{h}{l}\right)^2\frac{\bar{S}_{66}}{\bar{S}_{11}}} \tag{2.10}$$

In the above, $\bar{S}_{ij}$ are the transformed compliances in the laminate coordinate system and l and h are the length and half-width of the specimen, respectively. Numerical results of the above equations indicate that the determination of the in-plane shear modulus G_{12} is affected more adversely by end-constraint effects than the off-axis Young's modulus $E_{xx}(\theta)$ and the Poisson's ratio $\nu_{xy}(\theta)$, especially for small off-axis orientations. This has significant implications with regard to the determination of the true shear stress-strain response using short specimens in the low off-axis range.

For the present Gr/Al off-axis tension-compression coupon with an aspect ratio of 1.75, the values of $E^*_{xx}(\theta)$, $\nu^*_{xy}(\theta)$ and $G^*_{12}(\theta)$ as a function of the fiber orientation are shown in Fig. 2.16. The values obtained from transformation theory [44] are also included for comparison. The input material properties, generated from tensile coupon tests, are listed in Table 2.3. Fig. 2.16 demonstrates the adverse influence of the end-constraint effects on the elastic moduli. Comparing the apparent value (with superscript '*') with true value, it is seen that $E^*_{xx}(\theta)$ is higher in the 10° - 40° off-axis range. The value of G^*_{12} is higher than G_{12} when fiber orientation is less than 30°, and the difference is more significant at small fiber orientation. The apparent Poisson's ratio, ν^*_{xy} is also higher than ν_{xy}, and the largest ratio of ν^*_{xy}/ν_{xy} can be as high as 4.7 at 23°. Detailed correlation with experimental results will be presented in Section 3.2.

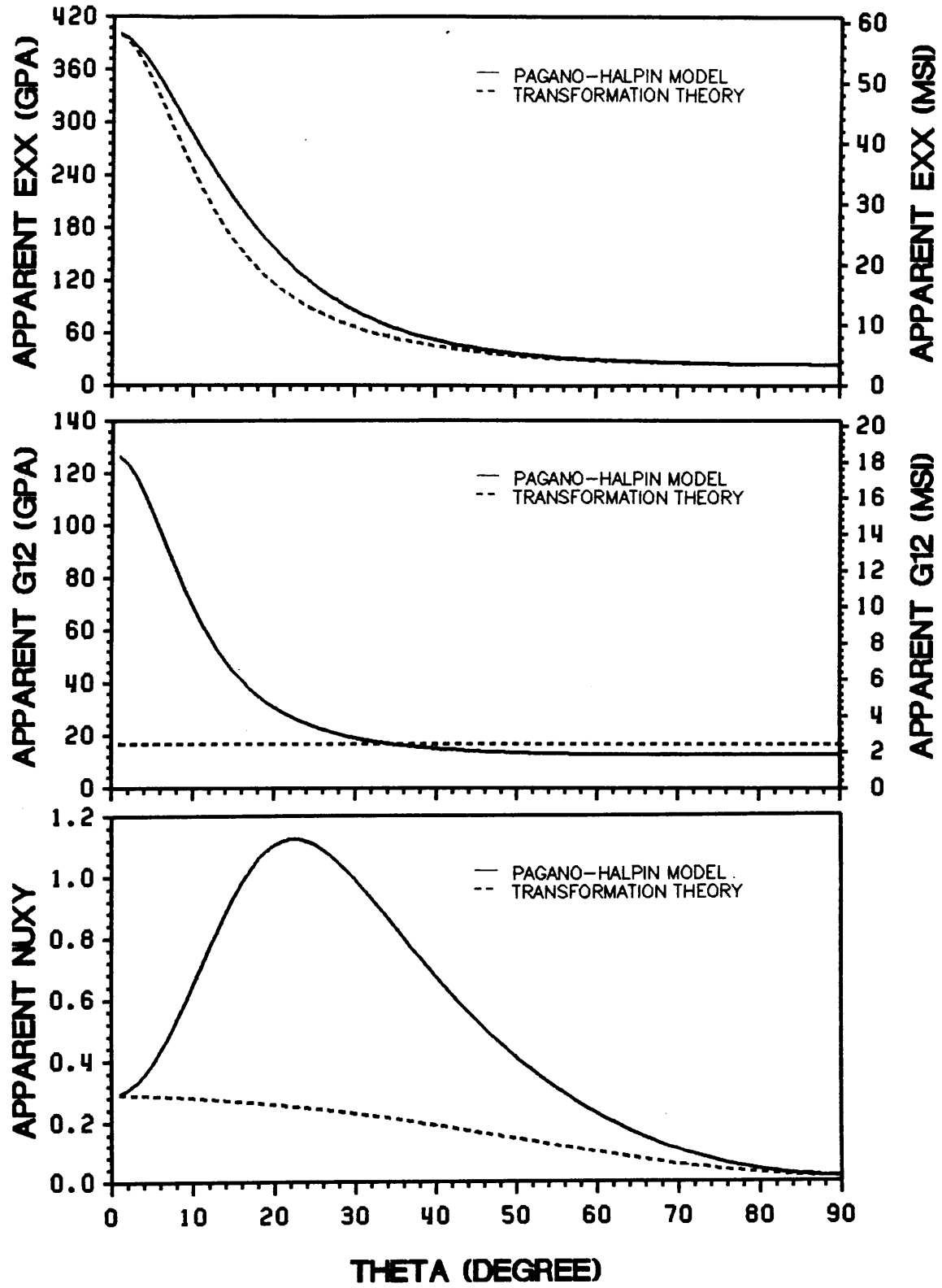

Figure 2. 16. Apparent elastic moduli as a function of fiber orientation.

Chapter 3 Experimental Results

3.1 Introduction

The experimental results are presented in the following sections. These results include: (1) the response of tension-compression-tension cyclic tests at three test temperatures; (2) the response of compression-tension-compression cyclic tests at three test temperatures; (3) the comparison of the two opposite cyclic loading paths. In addition, the results of monotonic tension and compression tests generated by Fujita [12] and Starbuck [13] are reviewed and compared with the results presented in (1) and (2), respectively. It should be mentioned that scatter in the experimental results exists because of different source panels of the specimens. The results presented in this chapter are typical responses for each loading condition. The individual test results are included in Appendix A. The results of monotonic tension and compression tests used for comparison are also typical responses.

The elastic moduli for tension-compression cyclic loading were obtained from the initial response, and the yield stress was determined from the linear proportional limit of the longitudinal stress-strain curves. The values presented here are the average values obtained from monotonic and

cyclic tests. For the convenience of comparison, the response curves at the three test temperatures are depicted in the same figure. In order to clearly show these curves in the same figure, some of the response curves were shifted along the horizontal (strain) axis.

3.2 Review and Discussion of Tension and Compression Results Generated in the Previous Studies

In the previous investigations, the elastic response, initial yielding, nonlinear behavior and the influence of test temperatures under tension and compression loading conditions have been discussed in an independent manner, [12] and [13]. In order to review and compare the behavior of the specimens loaded in tension and compression, the stress-strain curves generated in the previous studies are depicted here in the same figure. Fig. 3.1 and Fig. 3.2 illustrate the monotonic tension and compression response of 15° and 90° off-axis specimens, respectively, at three test temperatures. It is seen that for both specimen configurations, the elastic response in tension and in compression is not significantly different, but apparent differences in initial yielding and nonlinear response are observed. Comparing the magnitude of tensile and compressive yield stress for the 15° specimens, it is seen that at -150°F the ratio is about 2.3/11.7, and at room temperature it is about 5.1/7.0. At 250°F, since the compressive test exhibits a stiffening phenomenon, the compressive yield stress could not be easily obtained. For the 90° specimens, it is seen that the material response remains almost elastic up to failure in tension, while significant nonlinear response is observed in compression.

Generally speaking, initial yielding in tension increases with increase of the temperature, while in compression the magnitude of yield stress decreases with increase of the temperature. For the 15° off-axis specimens, the difference in tensile and compressive strength is not significant. It is seen

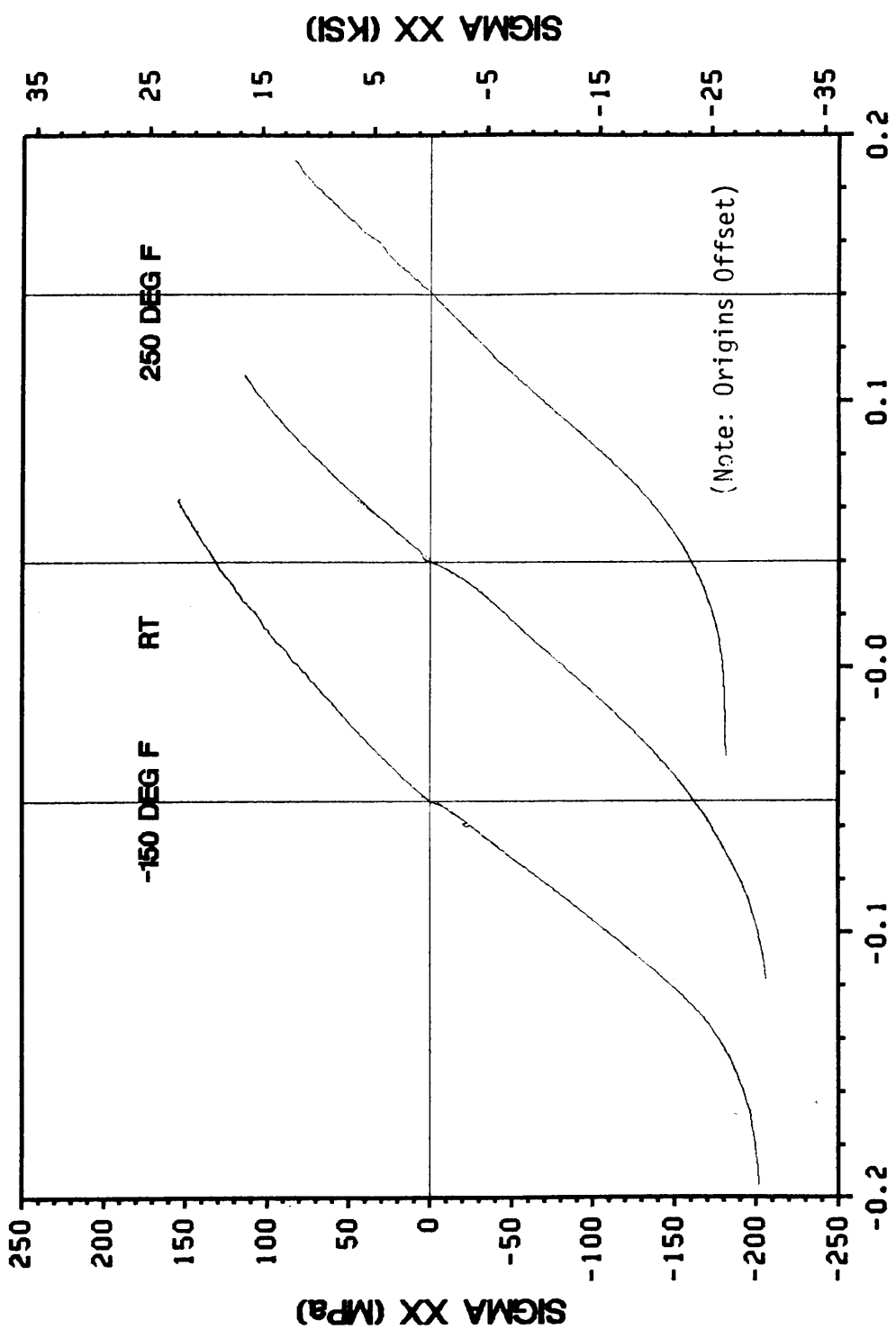

Figure 3. 1. Longitudinal response of 15° specimens under monotonic tensile and compressive loading at three different temperatures, reference [12,13]

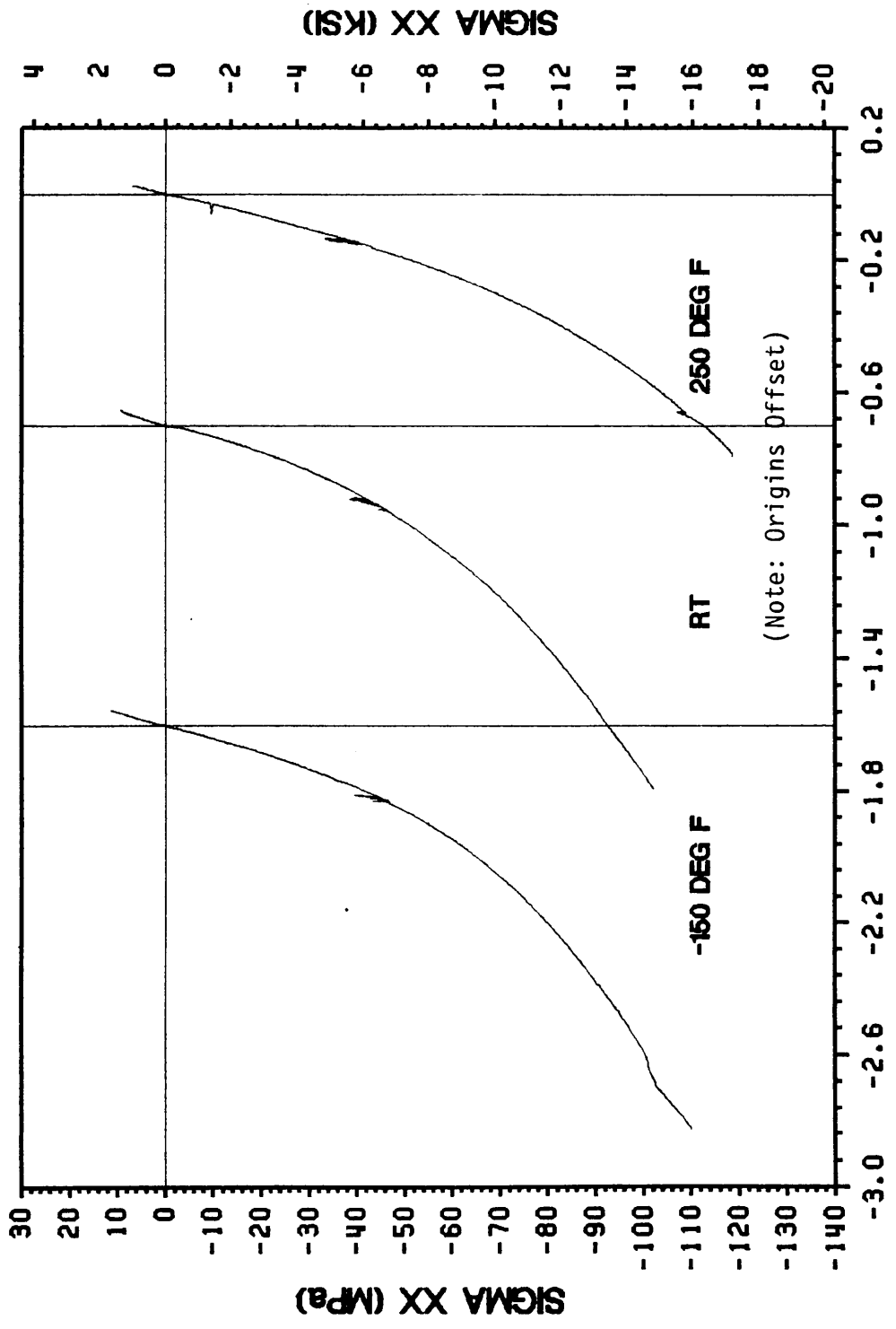

Figure 3. 2. Longitudinal response of 90° specimens under monotonic tensile and compressive loading at three different temperatures, reference [12,13]

that at -150°F, the material has almost the same tensile and compressive strength. However, for the 90° off-axis specimens, the material has very low tensile strength. The ratio of the tensile to compressive strength is about 1:14 for this configuration. This phenomenon is believed to be caused by the poor interfaces between adjacent precursor wires and the resulting inherent defects. Further discussion pertaining to the influences of the poor interface is presented in Chapter 5.

Fig. 3.3 and Fig. 3.4 illustrate the cyclic tension and compression response of 15° and 90° off-axis specimens, respectively, at three test temperatures. Due to the lack of experimental data, the stress-strain curves of cyclic compression at 250°F are not included. In these figures, the differences in initial yielding and nonlinear response between tension and compression loading conditions are more evident.

In the cyclic tension stress-strain curves of the 15° specimens, Fig. 3.3, it is seen that the unloading and reloading paths are essentially parallel to the initial linear response. Plastic strain accumulation is observed at zero load after unloading when the specimen is loaded past the proportional limit (at -150°F and room temperature). The small hysteresis loop observed at -150°F could be caused by energy dissipation or damage of the material microstructure. The material response under tensile loading appears to be predominantly elastoplastic.

In the cyclic compression stress-strain curves of the 15° specimens, Fig. 3.3, it is seen that significant hysteresis loops exist in the unloading-reloading cycle. These hysteresis loops become bigger with increasing temperature. A linear portion of response curve can be found for the unloading as well as reloading path, but the slope is different from that of the initial response. Both in unloading and reloading, apparent nonlinear response is observed after an initial linear portion. After unloading to zero load, significant plastic strain accumulation was exhibited at -150°F and room temperature with a tendency to increase with increasing temperature. Examining the entire cyclic response at each temperature, the subsequent yield stress appears to be translated. However, due to the slope change in unloading and reloading and the noticeable hysteresis rounding at the reversal points, the subsequent yield point cannot be easily defined. Thus, the classical plasticity theory cannot be

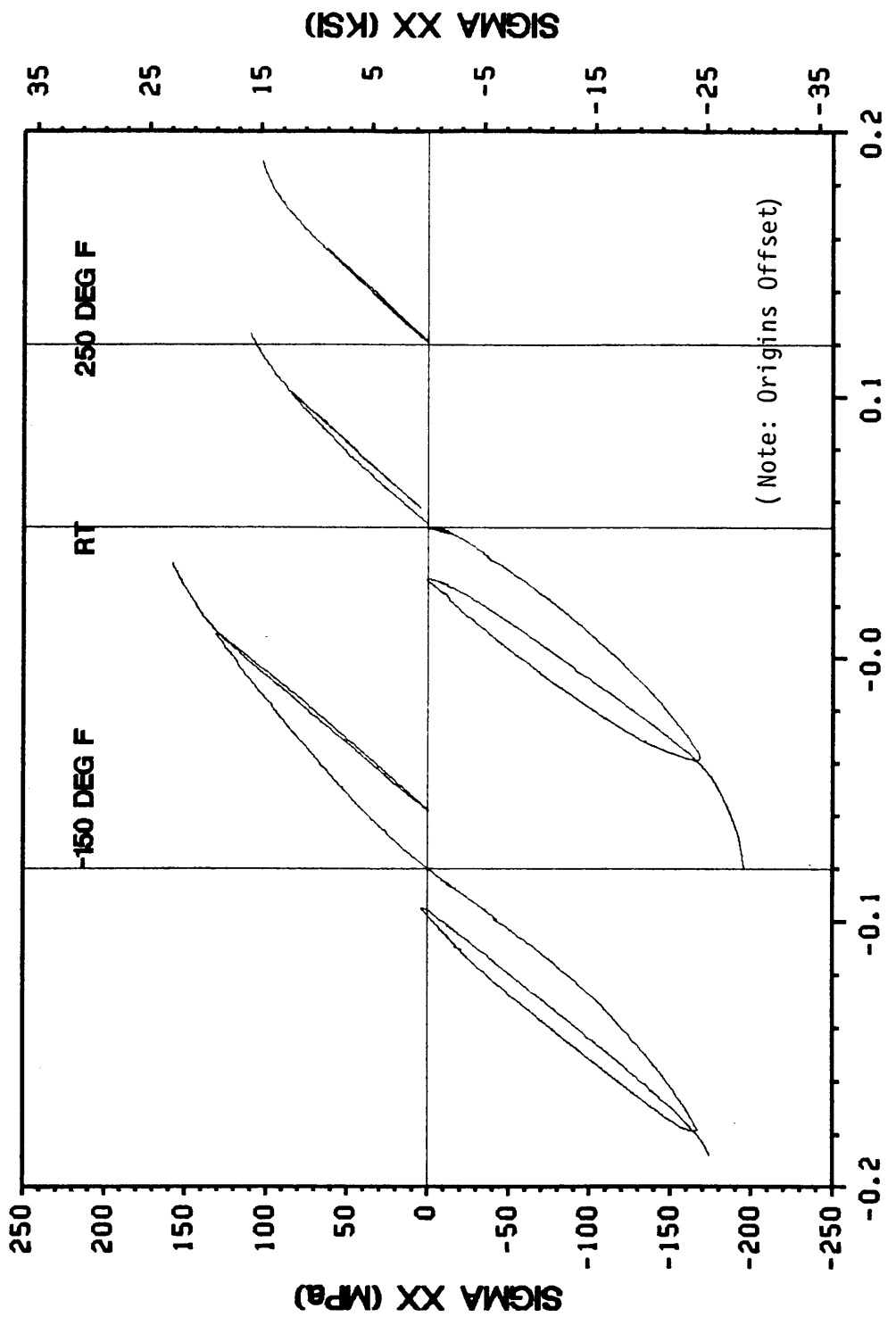

Figure 3. 3. Longitudinal response of 15° specimens under cyclic tensile and compressive loading at three different temperatures, reference [12,13]

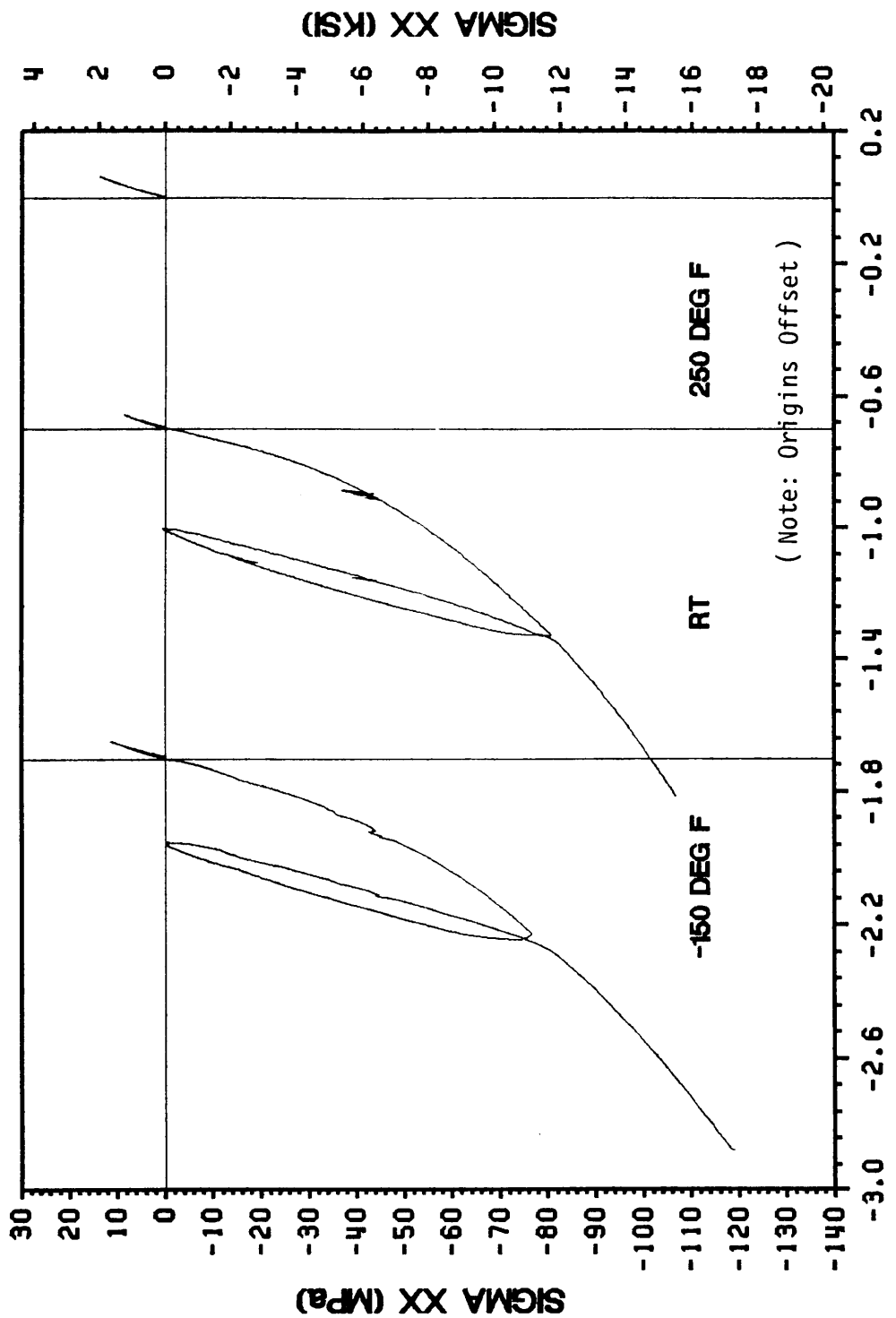

Figure 3. 4. Longitudinal response of 90° specimens under cyclic tensile and compressive loading at three different temperatures, reference [12,13]

employed exclusively to characterize the observed material response under this loading condition. It is evident that secondary mechanisms other than those of the plasticity theory are operative. The secondary mechanisms might involve material damage, deformation of wire-to-wire interface resulting in the closure of the voids, Fig. 2.7, interfacial slippage and friction or local buckling of the individual wires.

In Fig. 3.4, it is seen that the hysteresis phenomenon observed in the response of the 15° off-axis specimens in cyclic compression is also present in the unloading-reloading cycle of the 90° specimens subjected to compressive loading.

It can be concluded from the above discussion that under compression loading the elastoplastic behavior of the material is strongly influenced by secondary dissipative mechanisms. The actual nature of these mechanisms may be very complicated, and is believed mostly to be caused by the inherent defects of the material. On the other hand, under tension loading the influence of the secondary mechanisms is not pronounced, and the material response appears to be predominantly elastoplastic.

3.3 Tension-Compression-Tension Results

3.3.1 15° Specimen

The longitudinal stress-strain curves, Poisson's responses and axial shear stress-strain curves along material principal directions of typical 15° off-axis specimens at the three test temperatures under tension-compression-tension cyclic loading are presented in Fig. 3.5, Fig. 3.6 and Fig. 3.7,

respectively. For comparison, the results of monotonic tension tests are also included in the same figures (dashed lines).

3.3.1.1 Initial Elastic Response

The initial elastic moduli of tension-compression-tension and monotonic tension tests are summarized in Table 3.1.

Table 3.1 Initial Elastic Moduli of 15° Specimens (Tension-Compression-Tension and Monotonic Tension)

Apparent Elastic Constants	Tension Compression Tension Test	Monotonic Tension Test*
-150°F		
E^*_{xx}(msi)	27.3	27.1
ν^*_{xy}	0.353	0.288
G^*_{12}(msi)	2.82	2.96
RT		
E^*_{xx}(msi)	28.6	28.0
ν^*_{xy}	0.369	0.267
G^*_{12}(msi)	3.24	2.78
250°F		
E^*_{xx}(msi)	27.4	26.0
ν^*_{xy}	0.267	0.161
G^*_{12}(msi)	2.91	2.70

* Reference [12]

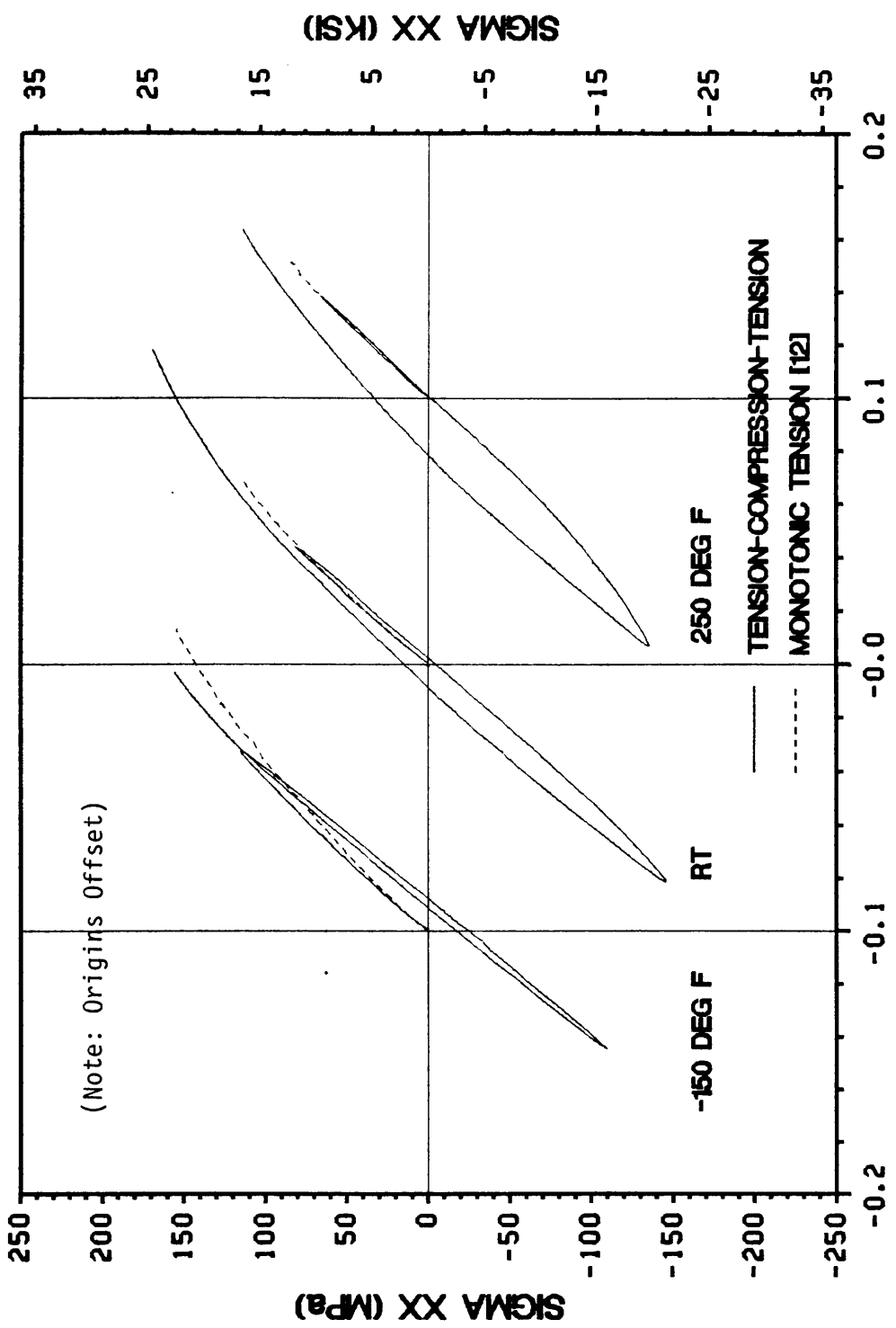

Figure 3. 5. Longitudinal response of 15° specimens under tension-compression-tension cyclic loading at three different temperatures.

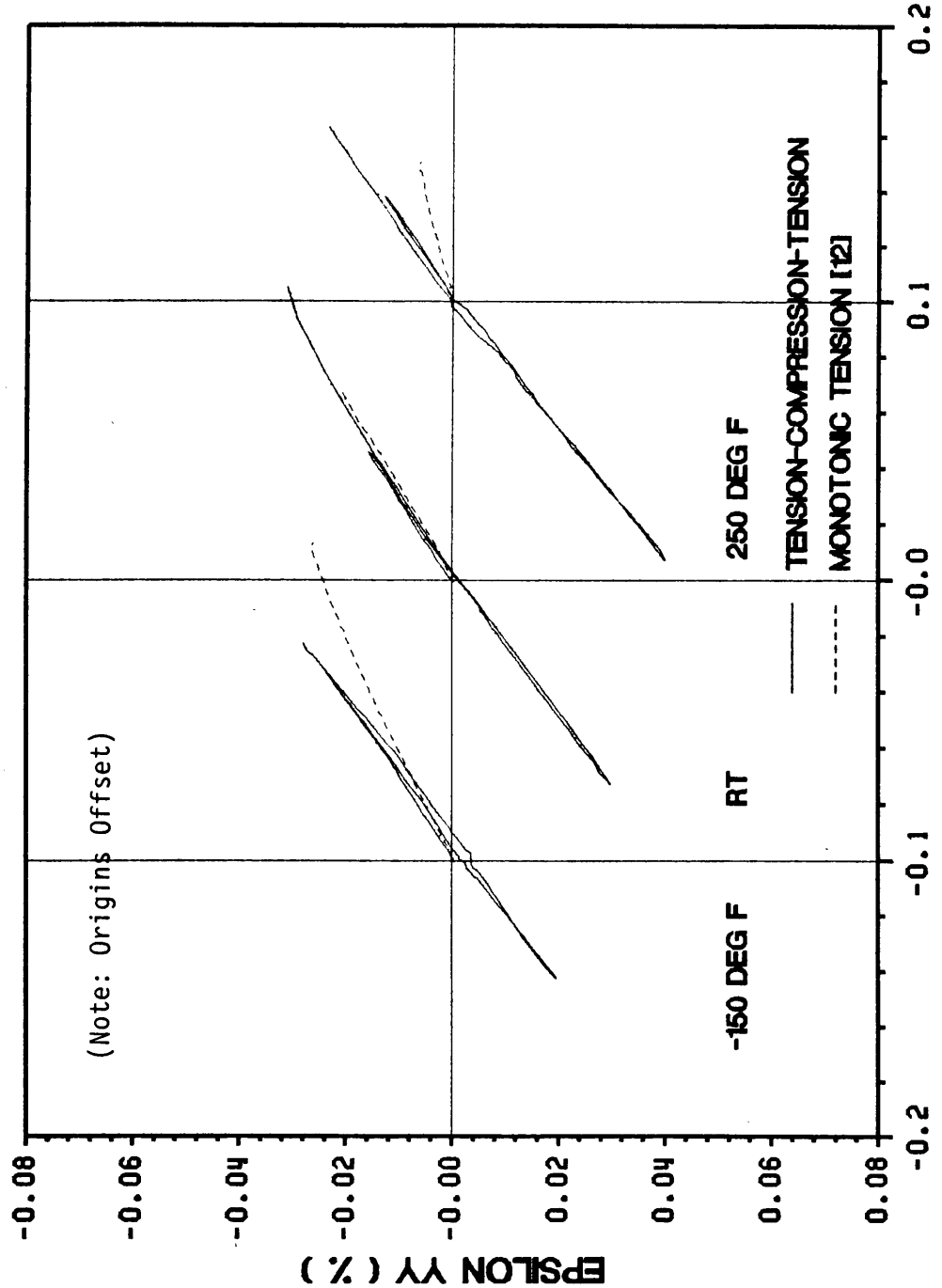

Figure 3. 6. Poisson's response of 15° specimens under tension-compression-tension cyclic loading at three different temperatures.

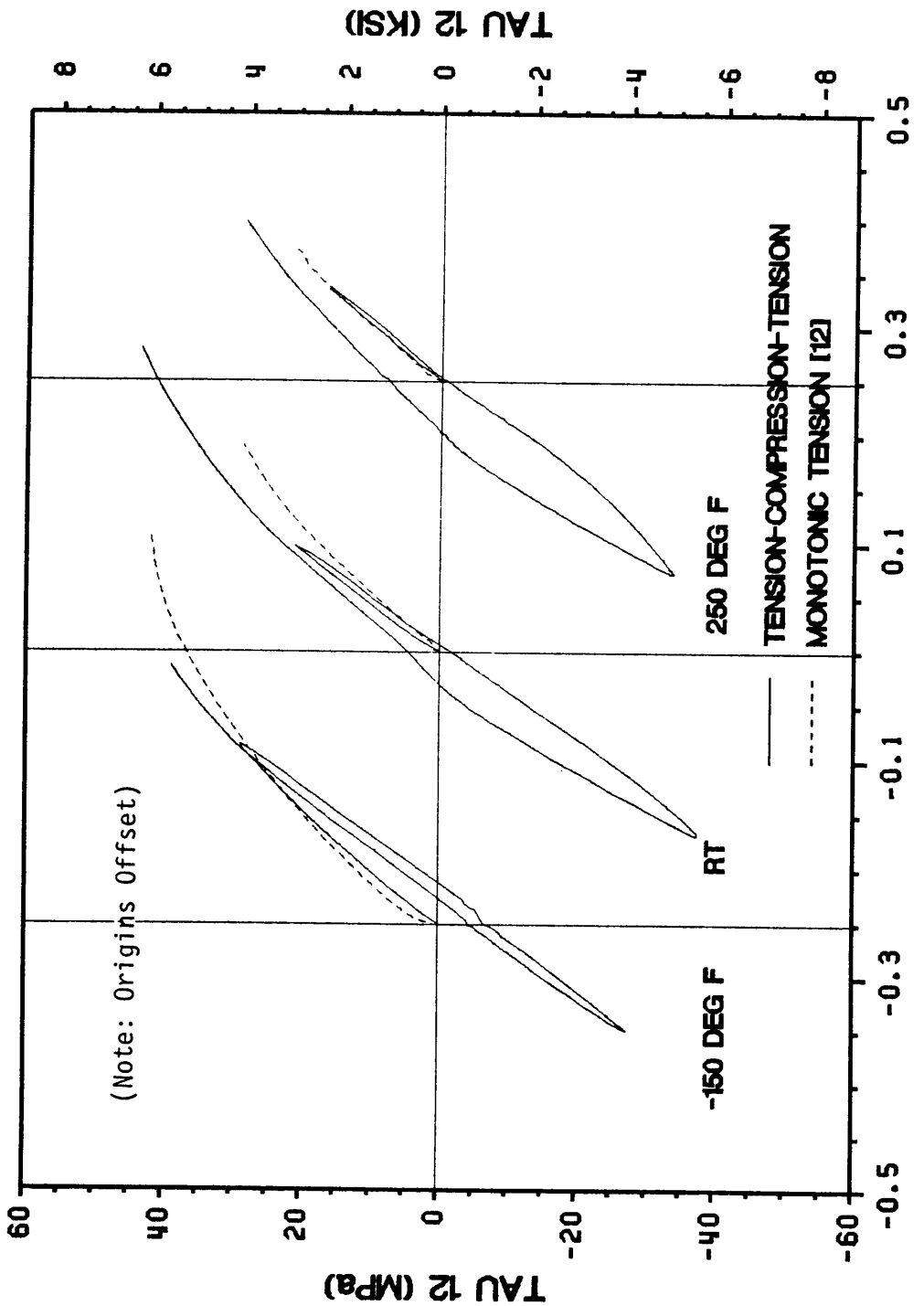

Figure 3. 7. Shear response of 15° specimens under tension-compression-tension cyclic loading at three different temperatures.

Comparing the elastic moduli of cyclic tests at the different temperature, it is seen that E^*_{xx} was not significantly affected by the test temperatures. This result was also observed in the monotonic tension tests. For ν^*_{xy} and G^*_{12}, no systematic trend of the influence of the temperature is evident. However, a slight decrease with increase of the temperature was observed in the monotonic test results.

Comparing the elastic moduli obtained from the two types of tests, it is seen that E^*_{xx} of the cyclic tests are slightly higher than those of the monotonic results. For ν^*_{xy}, the cyclic test results are noticeably higher at all the test temperatures. The value of G^*_{12} obtained in the cyclic test at -150°F is slightly lower than that of the monotonic test, but at room temperature and 250°F, higher values of G^*_{12} are observed in the cyclic results. Accordingly, it can be concluded that in general, the elastic moduli of the cyclic results are higher than those of the monotonic results. According to the end-constraint effects analysis [35], this trend is quite reasonable because tension-compression coupon has a lower aspect ratio.

The apparent elastic moduli of the 15° off-axis tension-compression coupons at room temperature obtained from Pagano-Halpin and FEM (with two types of boundary conditions) end-constraint analysis (see Section 2.7) are listed in Table 3.2. The values obtained from the transformation theory are also included for reference. Comparing E^*_{xx}, it is seen that excellent agreement was obtained between FEM analysis with the second boundary condition and the Pagano-Halpin model. The experimental results exhibit a slightly lower value. The FEM analysis with the fully clamped boundary condition appears to over-estimate the end-constraint effects and predicted a significantly higher value of E^*_{xx}.

For ν^*_{xy}, the FEM analysis with the two different boundary conditions yielded the same value. The experimental result exhibits a lower value of ν^*_{xy} in comparison with FEM results. A significantly higher value of ν^*_{xy} was predicted by the Pagano-Halpin model. Comparing the value of G^*_{12}, it is seen that the FEM analysis with the second boundary condition predicted a value fairly close to the experimental results. The difference is about 20%. Significantly higher values were predicted by

the Pagano-Halpin model and the FEM analysis with the fully clamped boundary condition. It appears that the Pagano-Halpin solution for v_{xy}^{*} and G_{12}^{*} may be not applicable for highly anisotropic specimens with small aspect ratios as is the case in the present investigation.

From the above comparison, it is seen that the FEM numerical results with the second boundary condition yield the best correlation with the experimental results. However, the experimental values appear to be lower than the analytical results. It is possible that the material might not appear to be transversely isotropic when relatively small specimens are tested due to the inherent defects in the microstructure. It will be recalled that the numerical analysis of the stress fields in the employed specimens was carried out under the assumption of a transversely isotropic continuum model. Another cause for the discrepancy may lie in the uncertainty associated with modelling analytically the actual boundary conditions.

Table 3.2 Comparison of Apparent Elastic Moduli of 15° Off-Axis Tension-Compression Coupon at Room Temperature

Apparent Elastic Moduli	FEM analysis		Pagano-Halpin Model	Experimental Results	Transformation Theory***
	B.C. 1*	B.C. 2**			
E_{xx}^{*}(msi)	40.7	31.0	31.2	28.6	24.2
v_{xy}^{*}	0.45	0.455	0.932	0.369	0.27
G_{12}^{*}(msi)	15.8	4.08	6.54	3.24	2.43

* Fully clamped
** Mid node at the ends constrained in y-direction
*** From material properties listed in Table 2.3

3.3.1.2 Yielding and Subsequent Response

The yielding and nonlinear response observed in the longitudinal stress-strain curves presented in Fig. 3.5 are discussed in the following.

At -150°F, the material initially yielded at 2.3 ksi. A relatively significant amount of strain hardening is observed in the post yielding response. During unloading, the response is essentially linear and a relatively significant plastic strain accumulation is observed at zero load. During subsequent compressive loading the material responded linearly down to -12 ksi. Very little strain hardening was observed past the proportional limit and the second reversal point. After the second reversal point, the subsequent unloading response was linear with a relatively small amount of strain recovery at zero load. Following the same linear behavior, the stress-strain curve during reloading in tension almost returned to the first reversal point and continued with similar strain hardening as observed in the initial tensile response up to failure.

At room temperature, the material yielded at 4.3 ksi, and the post yielding response did not show significant strain hardening. During unloading, the response was essentially linear and a relatively small amount of strain accumulation was observed at zero load. The material responded linearly during subsequent compressive loading down to -4 ksi. Noticeable strain hardening was observed past the above proportional limit and the second reversal point. During subsequent unloading, the response was initially linear and deviated from linearity at -5.5 ksi. At zero load after unloading, a noticeable amount of negative strain accumulation was observed. During subsequent reloading in tension, the specimen continued to respond in a nonlinear fashion up to failure. A negative strain off-set at the first stress reversal level is evident in the reloading response. It is clearly seen that the specimen failed at a higher stress level than the specimen tested in monotonic tension.

At 250°F, the material response during initial tensile loading was almost linear up to the first reversal point at 9 ksi. The unloading response was very close to the response of the initial loading and almost returned to the origin. During subsequent compressive loading, the material responded linearly down to -4 ksi. Significant strain hardening was observed past the proportional limit. During subsequent unloading, the response was initially linear and deviated from linearity at -4 ksi. At zero load, significant negative plastic strain accumulation was observed. The reloading response in tension followed the previous nonlinear trend up to failure and resulted in a significant negative

strain off-set at the first stress reversal level. Again, the specimen failed at a higher ultimate strength than that tested in monotonic tension.

Comparing the stress-strain curves of the 15° off-axis specimens at different temperatures, the following influence of temperature on material behavior was observed:

1. The initial tensile yield stress increases with increasing temperature. This phenomenon was also observed by Fujita in reference [12].

2. In the initial tensile loading more nonlinear response was observed at lower temperature, while more nonlinear response was seen at higher temperature in the subsequent compressive loading.

3. After subsequent compressive loading-unloading cycle, positive plastic strain accumulation was observed at -150°F, while it became negative at room temperature and was more significant at 250°F.

4. After reloading in tension, no off-set from the first reversal point was observed at -150°F, while off-set existed at room temperature and was more significant at 250°F.

The above observed phenomena indicate that the initial yield stress translates under the influence of the test temperature. The translation of the yield stress might be caused by the residual stresses in the each phase of the composite due to the mismatch of the thermal expansion coefficients of the constituents. The tensile strength at room temperature and 250°F appears to increase (compared with the monotonic results) after plastic deformation in compression. However, it is noted that in the short 15° off-axis specimens employed in the present investigation, there are some fibers that span the length of the specimen between the upper and lower grips.

In the stress-strain curves discussed above, it is seen that hysteresis rounding exists at the reversal points, and the linear portion in the unloading response in compression is not parallel to that of the

initial loading. Due to this phenomenon, subsequent yielding in the response curves is difficult to define. Thus, the discussion of the dissipative response of this material cannot be conducted exclusively in terms of the classical plasticity characteristics such as subsequent yield surface evolution. The observed phenomenon strongly implies that in addition to the mechanism of classical elastoplastic theory, secondary dissipative mechanisms were operative during the test.

3.3.1.3 Poisson's and Shear Response

In Fig. 3.6, it is seen that the transverse strain response is similar to the longitudinal strain response. Since a relatively small magnitude in transverse strain was measured, yielding and nonlinear response in Poisson's response are difficult to analyze.

In Fig. 3.7, it is seen that the shear response exhibits exactly the same trends as those observed in the longitudinal response. At the transition of the tension and compression loading, apparent slope changes in the shear stress-strain curves are observed. This could be caused by pull-out of the specimen when it is subjected to tensile loading. In tension, if the specimen is pulled out from the grips, the end-constraint effects is reduced. On the other hand, the specimen is in firm contact with the base of the grips in compression, and it can not be pushed out from the grips. Thus the slope of the shear response curves in tension is smaller than that in compression.

3.3.2 90° Specimen

The longitudinal stress-strain curves and Poisson's responses of typical 90° specimens at the three test temperatures under tension-compression-tension cyclic loading are presented in Fig. 3.8 and Fig. 3.9, respectively. For comparison, the results of monotonic tension tests are also included in the same figures.

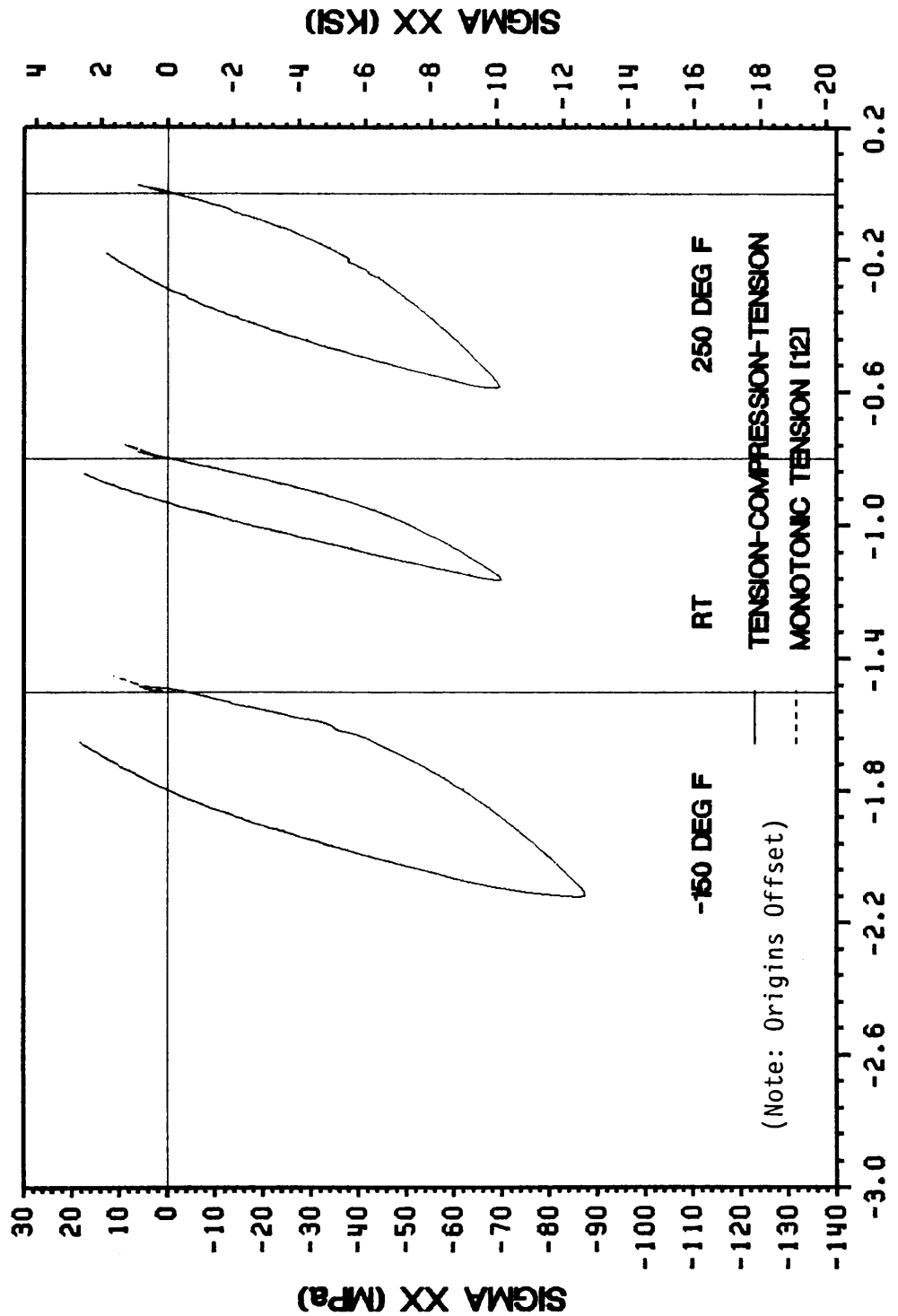

Figure 3. 8. Longitudinal response of 90° specimens under tension-compression-tension cyclic loading at three different temperatures.

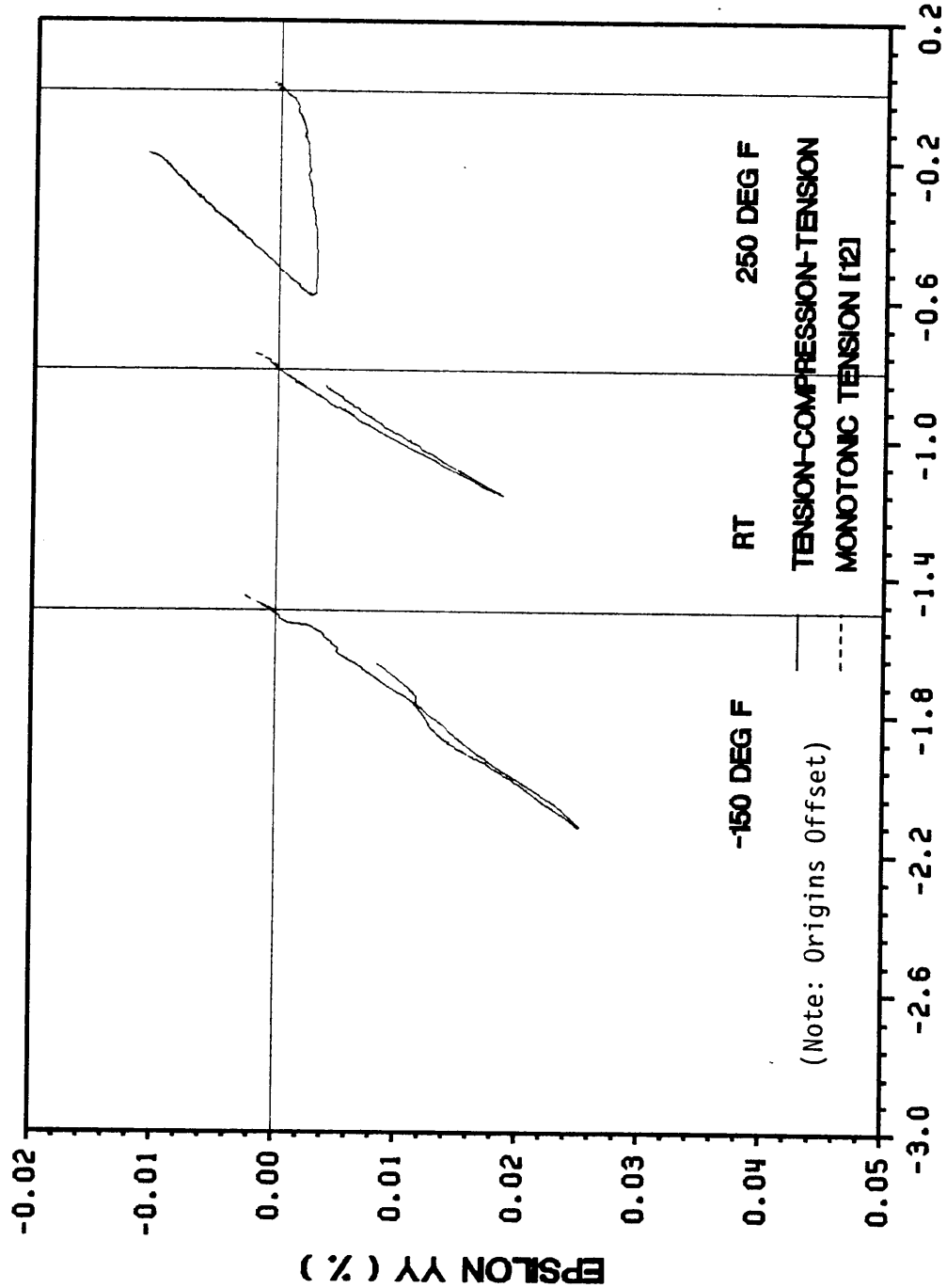

Figure 3. 9. Poisson's response of 90° specimens under tension-compression-tension cyclic loading at three different temperatures.

3.3.2.1 Initial Elastic Response

The initial elastic moduli of tension-compression-tension cyclic loading and monotonic tension tests are summarized in Table 3.3. Comparing the elastic moduli of cyclic loading at the different test temperatures, it is seen that $E_{22}^{\bullet}$ was not significantly affected by temperature, while a noticeable decrease in $\nu_{21}^{\bullet}$ with increase of the temperature is seen. These phenomena were also observed in the monotonic tests.

Comparing the elastic moduli obtained from the two types of tests, it is seen that the results are quite close. This observation is reasonable, because no end-constraint effects in 90° specimens are expected as shown by end-constraint analyses.

Table 3.3 Initial Elastic Moduli of 90° Specimens
(Tension-Compression-Tension and Monotonic Tension)

Apparent Elastic Constants	Tension Compression Tension Test	Monotonic Tension Test*
-150°F		
$E_{22}^{\bullet}$(msi)	4.3	4.4
$\nu_{21}^{\bullet}$	0.044	0.053
RT		
$E_{22}^{\bullet}$(msi)	4.3	3.5
$\nu_{21}^{\bullet}$	0.030	0.028
250°F		
$E_{22}^{\bullet}$(msi)	3.9	4.2
$\nu_{21}^{\bullet}$	0.025	0.024

* Reference [12]

3.3.2.2 Yielding and Subsequent Response

The yielding and nonlinear response observed in the longitudinal stress-strain curves presented in Fig. 3.8 are discussed in the following.

At -150°F, the material yielded at a very low stress level, 0.2 ksi, and the post yielding response exhibited apparent strain hardening. During unloading, rounding of the hysteresis loop at the reversal point was observed and an apparent plastic strain accumulation is evident at zero load. Subsequent compressive loading exhibits kinks in the response curve. This could be a local effect caused by folding of the indentations in the aluminum layer. Disregarding these kinks, a linear portion can be found in the initial response with a linear limit point at -4.3 ksi. Past the linear limit point, significant nonlinear response is observed. During subsequent unloading, a significant hysteresis rounding is seen at the reversal point, and a noticeable negative strain accumulation is present at zero load. The stress-strain response exhibits an elliptic curve during this unloading condition. Only a small portion of linear response is seen and the slope is different from the initial response. The reloading response in tension essentially follows the nonlinear trend seen in the unloading portion of the stress-strain curve. It is clearly seen that the specimen failed with a noticeable amount of negative plastic strain accumulation, and a noticeable increase of the ultimate stress compared with the monotonic test result.

At room temperature, the material yielded at 0.4 ksi, and the post yielding response did not exhibit significant strain hardening. During unloading, the response was essentially linear and a relatively small amount of plastic strain accumulation was observed at zero load. The subsequent compressive response was initially linear up to -3.8 ksi with the same slope as the unloading response. Past the linear limit point, an apparent nonlinear response was observed. In the subsequent unloading, some hysteresis rounding is seen at the reversal point, and a negative plastic strain accumulation is observed at zero load. The reloading response in tension essentially follows the nonlinear trend observed in the unloading cycle. It is clearly seen that the specimen failed with

a significant amount of negative strain accumulation, and with a higher ultimate stress than that of the monotonic test result. The increase of the ultimate stress after the loading cycle is believed to be caused by the closure of the inherent voids during the subsequent compressive loading.

The response at 250°F exhibited the same trend as the response at room temperature. The material initially yielded at 0.5 ksi and did not strain harden significantly up to the reversal point. During subsequent compressive loading, the response curve deviated from linearity at -1.8 ksi with a significant nonlinear response past the linear limit point. After subsequent unloading and reloading in tension, a significant negative strain accumulation was seen at zero load and at failure. A higher ultimate stress than that of monotonic test result is also observed.

Comparing the stress-strain curves of the 90° specimens at different temperatures, the following influence of temperature on the material behavior was observed:

1. The initial yield stress increases with increasing temperature. This trend was also observed by Fujita in reference [12].

2. In subsequent compressive loading, the magnitude of the linear limit stress decreases with increasing temperature.

3. It is seen that negative plastic strain accumulation at 250°F is larger than that at room temperature; the response at -150°F also exhibits a relatively larger negative plastic strain accumulation. However, it is noted that the second reversal point at -150°F is at a higher stress level than that at room temperature and 250°F. If the second reversal point for all the temperatures were hypothetically at the same stress level, the negative plastic strain accumulation would most likely increase monotonically with increasing temperature.

In the stress-strain curves discussed above, it is seen that significant rounding of the hysteresis loops exists at the reversal points, and the linear response of the compressive unloading cycle is not parallel to the initial tensile loading. Similar phenomena were also observed in the response of the

15° specimens. Thus, the exact subsequent yield point cannot be easily defined in the response curves. This indicates that the secondary dissipative mechanisms also have significant influence on the compressive response of the 90° configuration. Therefore, further investigations in the yield surface evolution cannot be discussed from the present test results.

3.3.2.3 Poisson's Response

In Fig. 3.9, it is seen that an unusual phenomenon occurs at 250°F. The Poisson's response at 250°F exhibits a significant change in slope in the subsequent compressive loading. This indicates that the specimen contracted with a relatively small amount of strain in the transverse direction when it was subjected to subsequent compressive loading. This cannot be explained by scatter of the experimental data or strain gage problem, since the same result was also obtained from the other tested specimen.

3.4 Compression-Tension-Compression Results

3.4.1 15° Specimen

The longitudinal stress-strain curves, Poisson's responses and axial shear stress-strain curves along material principal directions of typical 15° off-axis specimens at the three test temperatures under compression-tension-compression cyclic loading are presented in Fig. 3.10, Fig. 3.11 and Fig. 3.12, respectively. For comparison, the results of monotonic compression tests are also given by dashed lines in the same figures.

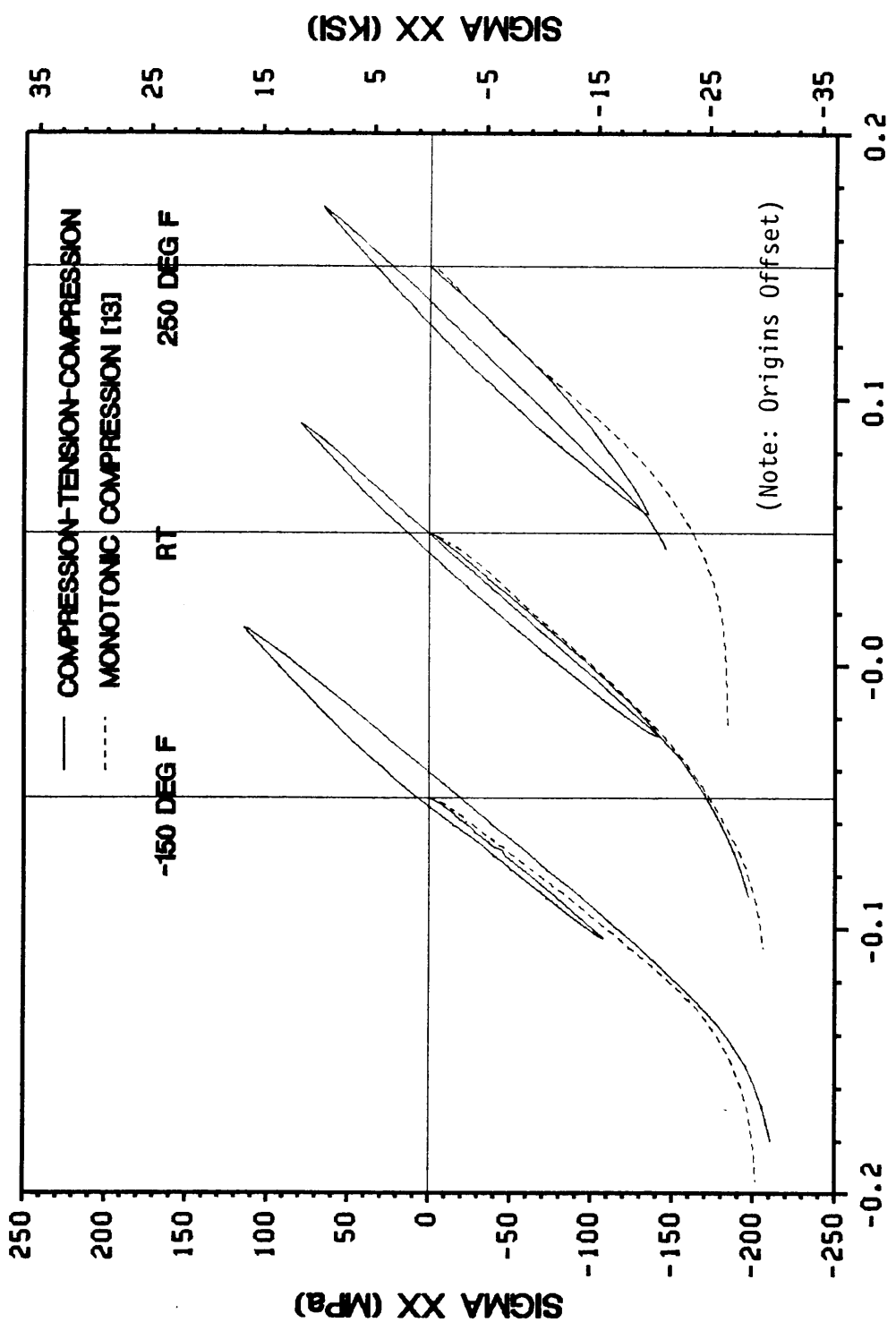

Figure 3. 10. Longitudinal response of 15° specimens under compression-tension-compression cyclic loading at three different temperatures

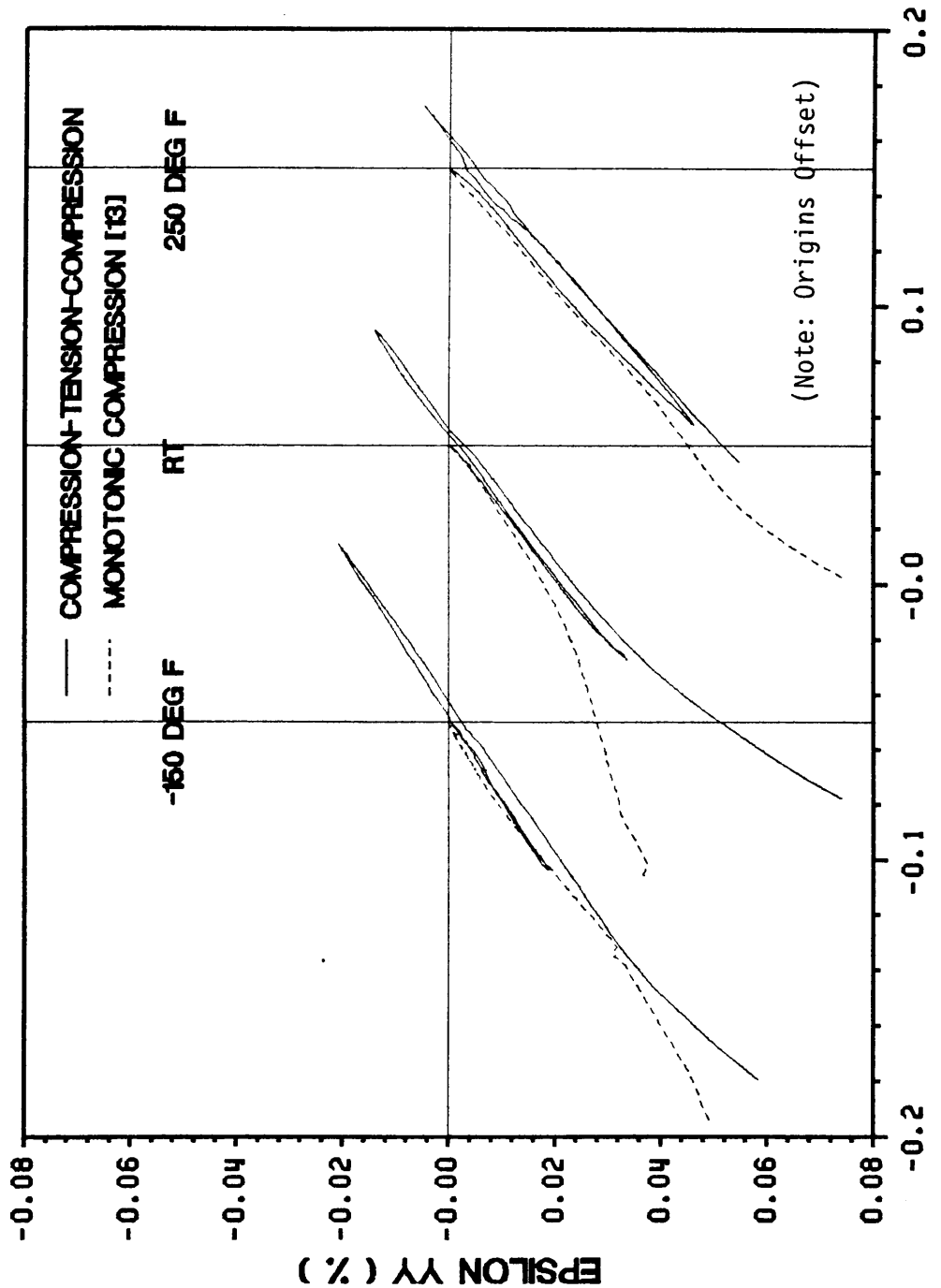

Figure 3. 11. Poisson's response of 15° specimens under compression-tension-compression cyclic loading at three different temperatures.

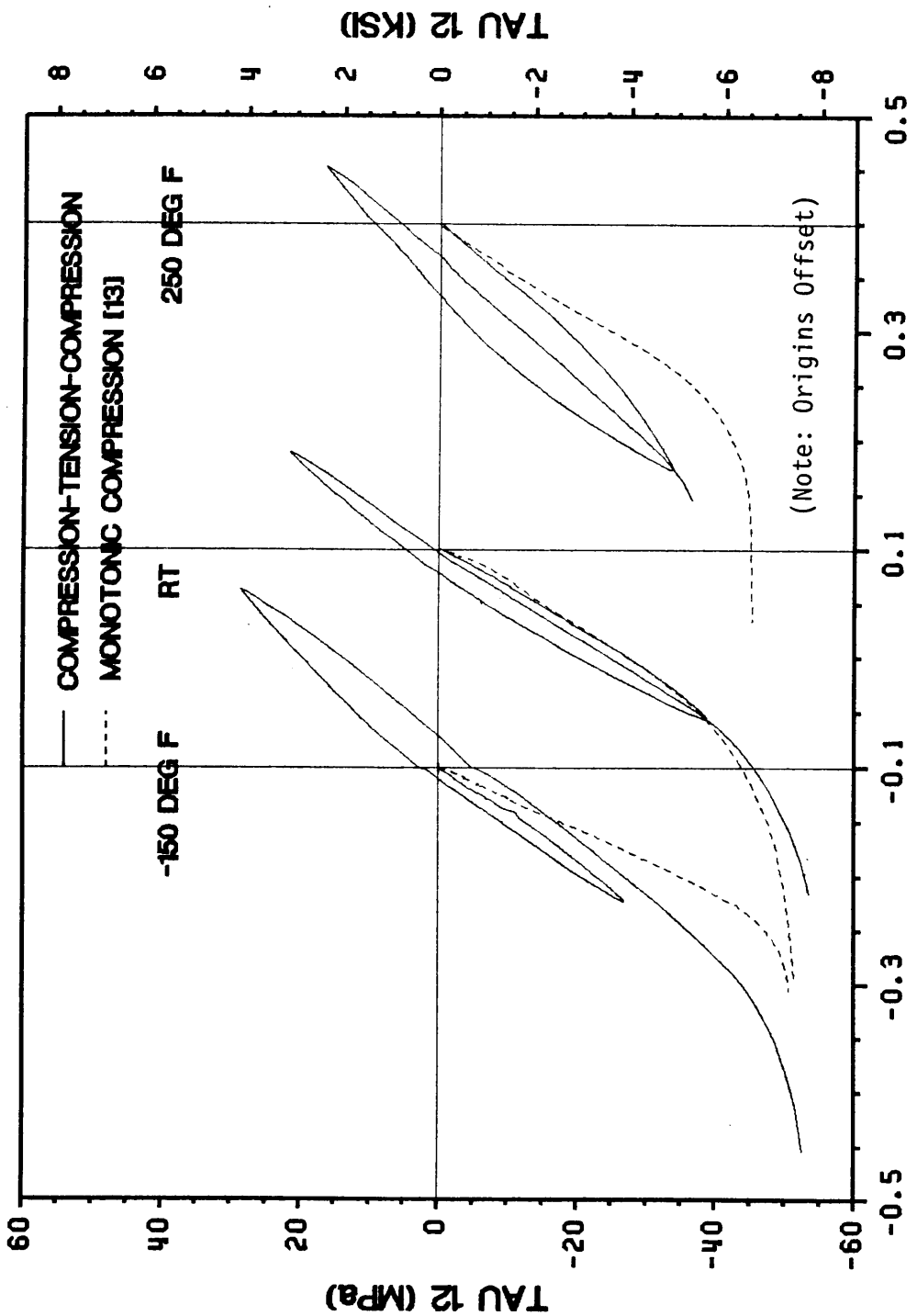

Figure 3. 12. Shear response of 15° specimens under compression-tension-compression cyclic loading at three different temperatures.

3.4.1.1 Initial Elastic Response

The initial elastic moduli of compression-tension-compression cyclic loading and monotonic compression tests are summarized in Table 3.4. Comparing the elastic moduli of cyclic loading at the different test temperatures, it is seen that E^*_{xx} was not significantly affected by the test temperatures, although the value at 250°F was a little lower than those at -150°F and room temperature. For v^*_{xy} the value increased with increase of temperature, but the largest difference was within 10%. For G^*_{12} , it is seen that there is no systematic trend for the effects of the test temperature.

Table 3.4 Initial Elastic Moduli of 15° Specimens (Compression-Tension-Compression and Monotonic Compression)

Apparent Elastic Constants	Compression Tension Compression Test	Monotonic Compression Test*
-150°F		
E^*_{xx}(msi)	28.3	32.0
v^*_{xy}	0.435	0.318
G^*_{12}(msi)	3.34	4.21
RT		
E^*_{xx}(msi)	30.2	36.9
v^*_{xy}	0.460	0.300
G^*_{12}(msi)	4.00	3.42
250°F		
E^*_{xx}(msi)	26.0	25.1
v^*_{xy}	0.475	0.450
G^*_{12}(msi)	2.72	3.78

* Reference [13]

Comparing the elastic moduli obtained from the two types of tests, it is seen that for E^*_{xx}, good agreement is obtained at 250°F, but at -150°F and room temperature the cyclic results are lower than those of the monotonic results. The highest difference is about 18%. For ν^*_{xy}, the results of two types of tests are quite close at 250°F, while apparently higher values in the cyclic results are observed at -150°F and room temperature. Poor agreement was obtained for G^*_{12} for all the test temperatures. The highest difference is about 30%. This discrepancy could be caused by the different boundary conditions in the cyclic and monotonic tests and scatter of the experimental data.

3.4.1.2 Yielding and Subsequent Response

The yielding and nonlinear response observed in the longitudinal stress-strain curves presented in Fig. 3.10 are discussed in the following.

At -150°F, the material yielded at -11 ksi. Little nonlinear response was observed up to the first reversal stress level. The unloading response was essentially linear with an apparent rounding at the reversal point. In the unloading curve, a kink was seen at -3.5 ksi stress level. At zero load, a small amount of negative plastic strain accumulation was observed. During subsequent tensile loading, significant nonlinear response is evident. The subsequent unloading response was essentially linear with some hysteresis rounding at the reversal point and with a noticeable positive plastic strain accumulation at zero load. The reloading response in compression followed the same linear trend of the unloading response down to -16 ksi. However, the slope of the linear response was smaller than the slope of the initial compressive response. A positive strain off-set at the first reversal stress level exists after the unloading-reloading cycle.

At room temperature, the material yielded at -6.5 ksi. The unloading response was initially linear with a significant hysteresis rounding at the reversal point, and the linear limit point was at -6 ksi. A significant negative strain accumulation was present after unloading. During the subsequent

tensile loading and unloading cycle, most of the previous strain accumulation was recovered. In reloading in compression, the response curve almost passed through the first reversal point.

The response at 250°F exhibited the same trends as those observed at room temperature, but with more nonlinearity in the entire loading cycle, and a larger amount of negative strain accumulation at zero load. Comparing the stress-strain curves at the different temperatures, the following influence of temperature on the material behavior was observed:

1. The magnitude of the initial yield stress decreases with increasing temperature.

2. The extent of nonlinearity observed in the initial compressive response increases with increasing temperature.

3. After the subsequent tensile loading-unloading cycle, positive plastic strain accumulation was observed at -150°F, while at room temperature it became negative, and increased in magnitude at 250°F.

4. After reloading in compression, a positive strain off-set from the first reversal point was seen at -150°F, while no off-set was observed at room temperature and 250°F.

The same phenomena observed at tension-compression-tension cycle test, namely, slope changes at stress reversal points and hysteresis rounding, were also seen in the stress-strain curves discussed above.

3.4.1.3 Poisson's and Shear Response

In Fig. 3.11, it is seen that the transverse response is similar to the longitudinal strain response. Since a relatively small magnitude in transverse strain was measured, yielding and nonlinear response in Poisson's response are difficult to analyze.

In Fig. 3.12, the shear response exhibits the same trend as that observed in the longitudinal response. Slope changes and hysteresis rounding were more significant in the shear stress-strain behavior. As observed in the tension-compression-tension cycle, the slope changes in the stress-strain curves are especially apparent during transition between tension and compression loading. This discontinuous behavior might be caused by end-constraint effects or pull-out of the specimen when it is subjected to tensile loading.

3.4.2 90° Specimens

The longitudinal stress-strain curves and Poisson's responses of typical 90° specimens at the three test temperatures under compression-tension-compression cyclic loading are presented in Fig. 3.13 and Fig. 3.14, respectively. For comparison, the results of monotonic compression tests are also included in the same figures (dashed lines).

3.4.2.1 Initial Elastic Response

The initial elastic moduli of compression-tension-compression cyclic and monotonic compression tests are summarized in Table 3.5. Comparing the elastic moduli of cyclic loading at the different temperatures, it is seen that the influence of the temperature on E_{22}^{*} is not significant, while an apparent decrease in ν_{21}^{*} with increase of temperature is seen. These phenomena were also observed in the monotonic tests.

Comparing the elastic moduli obtained from the two types of tests, it is seen that the results are quite close. This observation is reasonable for 90° configuration since it is not affected by the end-constraint effects.

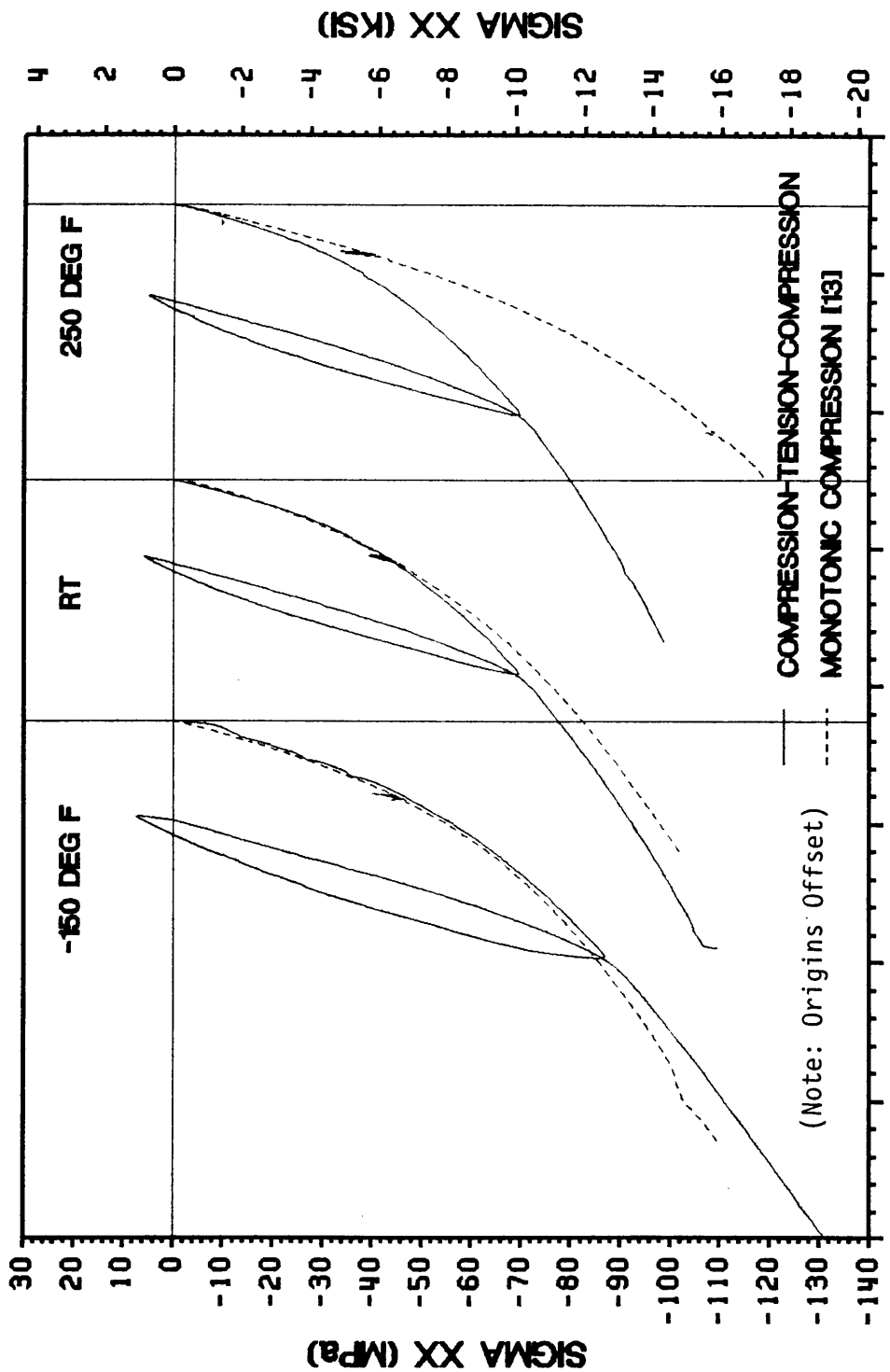

Figure 3. 13. Longitudinal response of 90° specimens under compression-tension-compression cyclic loading at three different temperatures

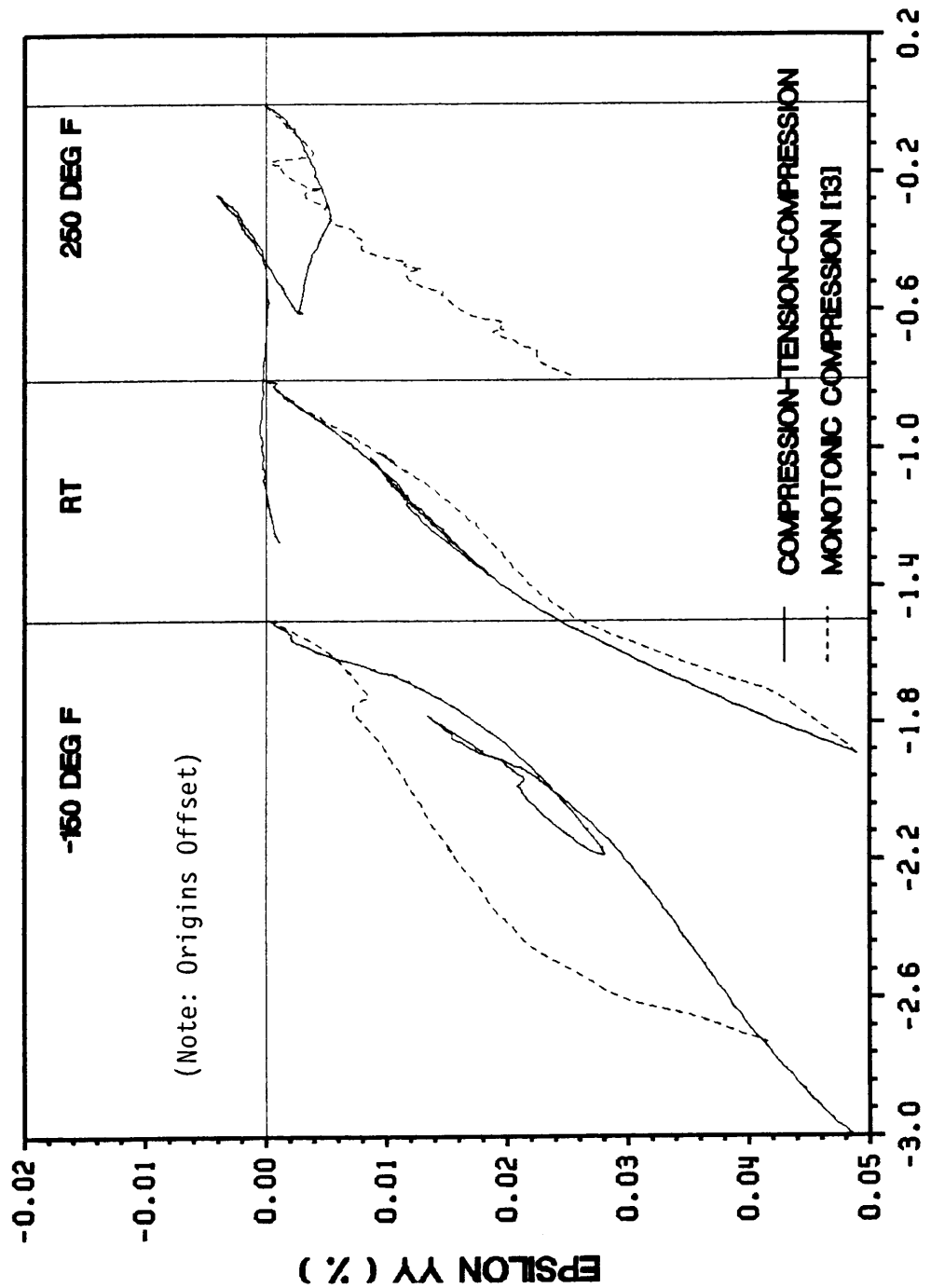

Figure 3. 14. Poisson's response of 90° specimens under compression-tension-compression cyclic loading at three different temperatures

Table 3.5 Initial Elastic Moduli of 90° Specimens
(Compression-Tension-Compression and Monotonic Compression)

Apparent Elastic Constants	Compression Tension Compression Test	Monotonic Compression Test*
-150°F		
E_{22}^{*}(msi)	3.5	3.6
ν_{21}^{*}	0.048	0.047
RT		
E_{22}^{*}(msi)	4.1	3.8
ν_{21}^{*}	0.035	0.046
250°F		
E_{22}^{*}(msi)	3.6	4.0
ν_{21}^{*}	0.025	0.026

* Reference [13]

3.4.2.2 Yielding and Subsequent Response

The yielding and nonlinear response observed in the longitudinal stress-strain curves presented in Fig. 3.13 are discussed in the following.

At -150°F, the stress increased significantly with a small amount of strain increment during the initial compressive loading. This response is believed to be caused by the icing problem of the test fixture (as indicated by the stress vs. time and strain vs. time plots). It should be disregarded in dealing with the material behavior. Despite the initial binding, good agreement with the monotonic test result is seen. The material yielded at approximately -4.8 ksi during the initial compressive loading. During the unloading cycle, significant hysteresis rounding exists at the reversal point, and

an elliptic response curve is observed. The subsequent tensile loading exhibits essentially the nonlinear trend observed during unloading. At the second reversal point, significant hysteresis rounding is also observed. The stress-strain reloading response in compression passes through the first reversal point and follows the nonlinear trend of the initial compression loading. The unloading-reloading response has the shape of an ellipse with some hysteresis rounding at the reversal points.

The response at room temperature and 250°F exhibits essentially the same trend as that observed at -150°F. Comparing the stress-strain curves at the different temperatures, it is seen that the magnitude of the initial yield stress decreased with increasing temperature. As observed in the tension-compression-tension loading cycle, if the first reversal points were at the same stress level for all the temperatures, the negative plastic strain accumulation would tend to increase with increasing temperature.

3.4.2.3 Poisson's Response

In Fig. 3.14, it is seen that an unusual phenomenon occurs at 250°F. As observed in the tension-compression-tension loading cycle, a significant slope change in initial compressive loading is present.

3.5 Comparison of Two Opposite Cyclic Loading Paths

The elastoplastic response of the material under two opposite cyclic paths, i.e. tension-compression-tension and compression-tension-compression, is compared and discussed in the following sections.

3.5.1 15° Specimen

The longitudinal stress-strain curves of the 15° off-axis specimens obtained from the two opposite cyclic paths are compared in Fig. 3.15. Comparing the two curves at the same temperature, it is seen that the loading history had no effect on the subsequent response past the second reversal point (i.e. terminal response follows the same trend of the initial loading). At room temperature and 250°F, it is seen that the tensile prestrain in the tension-compression-tension path had no significant influence on the subsequent compressive response. However, it is noted that no significant nonlinear response occurred during the initial prestraining at these two temperatures.

In the above figure, the influence of the temperature on the material behavior is more clearly exhibited. The initial yield stress, both in tension and compression, was translated up in the tensile direction when the temperature was increased. Following this trend, more nonlinear response was observed at lower temperature in tensile direction, while more nonlinear response was seen at higher temperature in compressive direction. This tendency implies that the residual stresses in the constituents of the composite have a significant effect on the material behavior. Further discussion is presented in Chapter 5.

3.5.2 90° Specimen

For comparison, the longitudinal stress-strain curves of 90° off-axis specimens under the two opposite cyclic loading paths are given in Fig. 3.16. Comparing the two curves at the same temperature, it is seen that at room temperature and 250°F the effect of tensile prestrain in the tension-compression-tension loading path is negligible, since the subsequent compressive response exhibited almost the same behavior as the initial compressive response of the opposite loading path.

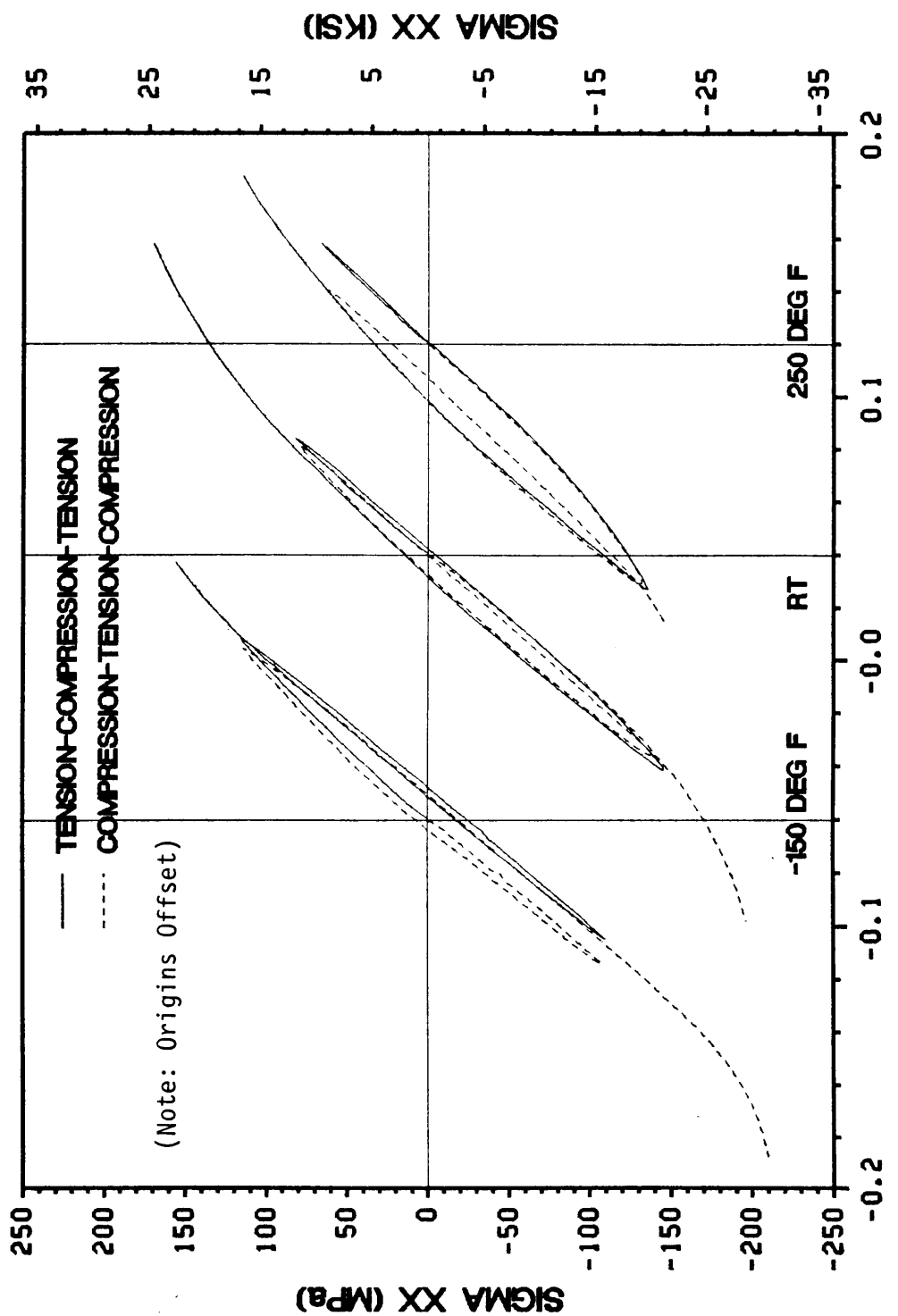

Figure 3. 15. Longitudinal response of 15° specimens under two opposite cyclic loading at three different temperatures.

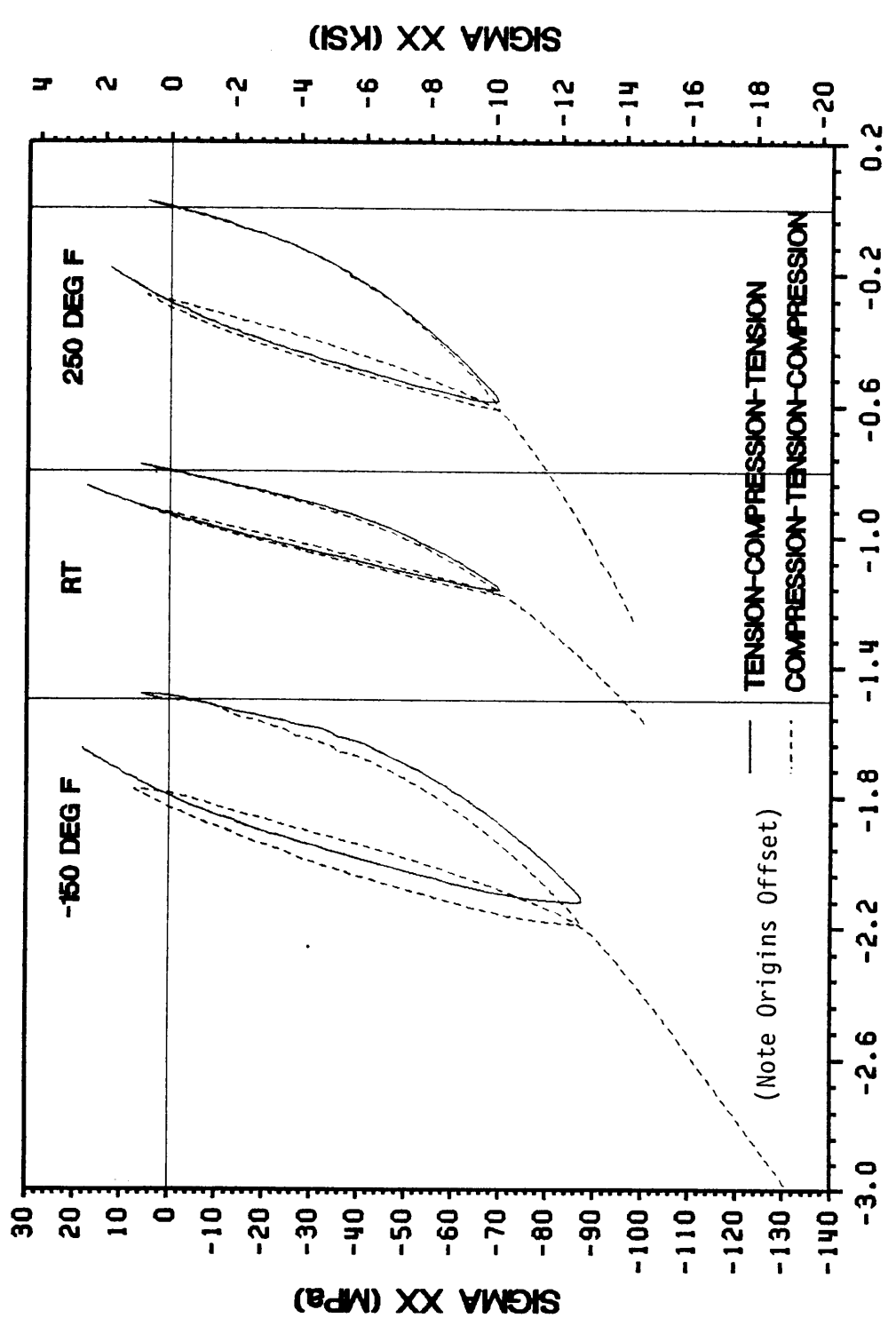

Figure 3. 16. Longitudinal response of 90° specimens under two opposite cyclic loading at three different temperatures.

At -150°F, the tensile prestrain in the tension-compression-tension loading path exhibits a small amount of plastic strain accumulation; thus the subsequent compressive response shows a little off-set when comparing with the initial compressive response of the opposite loading path.

The influence of the test temperature on the material behavior is more clearly shown in the above figure. In the same fashion as observed in the 15° specimens, the initial yield stress both in tension and compression was shifted in the tensile direction with increasing temperature. This indicates that the residual stresses also have significant effects on material behavior for the 90° configuration.

3.6 Summary

The experimental results described above are summarized in the following:

1. No significant temperature effects on $E^{\bullet}_{xx}$ ($E^{\bullet}_{22}$ for 90° specimen) and $G^{\bullet}_{12}$ was observed, and a slight decrease in $\nu^{\bullet}_{xy}$ ($\nu^{\bullet}_{21}$ for 90° specimen) with increase of temperature was seen.

2. The influence of end-constraints on the elastic moduli of the 15° off-axis specimens was observed in the experiment, but no quantitative agreement was obtained between the experimental and analytical results.

3. For the 90° specimen, the monotonic test results exhibited significantly different ultimate stress in tension and compression. The ratio of the tensile to compressive strength is about 1:15. In the tension-compression-tension cyclic loading, the tensile strength increased (compared with monotonic results) after the plastic deformation in compression.

4. The initial yield stress both in tension and compression was translated in the tensile direction with increasing temperature.

5. The strain hardening in tensile loading decreases with increasing temperature, while the strain hardening in compressive loading increases with increasing temperature.

6. For the 15° specimen, positive plastic strain accumulation was observed at the low temperature, while negative plastic strain accumulation was present at high temperature for both tension-compression-tension and compression-tension-compression loading path.

7. Under tension loading, the material response appears to be predominantly elastoplastic; under compressive loading, the influence of the secondary dissipative mechanisms was observed in the material response, thus classical plasticity theory cannot be employed exclusively to characterize the observed material behavior.

8. Under compression loading, more plastic strain and larger hysteresis loop were observed for the 90° specimens than for the 15° specimens.

9. Hysteresis rounding and slope changes of the compressive response at reversal points result in difficulty when defining subsequent yield stresses, thus further investigations of the yield surface evolution cannot be discussed from the present test results.

Chapter 4 Correlation of Micromechanics Model Predictions and Experimental Results

4.1 Introduction

The micromechanics model proposed by Aboudi [24-28] is employed in the present investigation to predict the elastoplastic response of unidirectional Gr/Al composites under combined tension-compression cyclic loading, and to correlate the analytical predictions with the experimental data. This model has been chosen due to the following features: (1) straightforward formulation which provides explicit closed form expressions for the effective response in terms of the constituent properties; (2) applicability to arbitrary loading paths, especially for the desired combined tension-compression cyclic loading, when it is incorporated with Bodner's unified theory of plasticity; (3) cost-effective computer programming and computation. In addition, good agreement between the predictions of this model and finite element analysis as well as experiments has been demonstrated in previous investigations [25,29].

In order to be able to predict the effective properties of heterogeneous media with sufficient accuracy using the micromechanics approach, the properties of the individual constituents must be well characterized. However, the complicated manufacturing process that fiber-reinforced metal matrix composites undergo often results in chemical and physical property changes in the constituents as well as residual stresses in each of the phases due to the mismatch of thermal expansion coefficients. Therefore, the actual in-situ properties need to be determined and taken into account in correlating the predictions of a micromechanics model with the experimental results. The detailed discussion of the correlation procedure employed in the present investigation will be presented in the following sections.

In Section 4.2, the derivation of the employed micromechanics model is briefly reviewed. The procedure of determining the in-situ properties and residual stresses is discussed in Section 4.3. In Section 4.4, the comparison of the analytical and experimental results is presented.

4.2 Review of Aboudi's Micromechanics Model Analysis

The micromechanics model proposed by Aboudi predicts the elastoplastic thermomechanical response of transversely isotropic composites from the provided properties of the constituents and fiber reinforcement ratio. In this model, the effective overall behavior of the composite is established on the basis of average stress-strain relations of the representative volume element. The derivation of these relations are outlined as follows.

4.2.1 Geometry

The model used in Aboudi's micromechanics analysis for unidirectional fiber-reinforced composites is shown in Fig. 4.1a. It consists of unidirectional fibers with rectangular cross section embedded in the matrix phase. The fibers extend along the x_1 direction and form a doubly periodic array in the x_2 and x_3 directions.

Due to the periodical arrangement of the fibers, it is sufficient to consider only the representative unit cell shown in Fig. 4.1b. The representative unit cell consists of four subcells designated by β , $\gamma = 1,2$, in which (11) represents the fiber subcell and the other three designations, (12), (21) and (22), represent the three matrix subcells. The dimensions of the rectangular cross section of the fibers are denoted by h_1 and l_1 , and the spacings between the adjacent fibers are given by h_2 and l_2. For convenience of the analysis, four local coordinate systems (x_1, $\bar{x}_2^{(\beta)}$, $\bar{x}_3^{(\gamma)}$) are introduced in each of the subcell with the origin at the center of each subcell.

4.2.2 Displacement Field

The displacement vector at any point within the given subcell ($\beta\gamma$) is approximated by the first order expansion in the local coordinates $\bar{x}_2^{(\beta)}$ and $\bar{x}_3^{(\gamma)}$ as follows:

$$u_i^{(\beta\gamma)} = w_i^{(\beta\gamma)} + \bar{x}_2^{(\beta)}\, \phi_i^{(\beta\gamma)} + \bar{x}_3^{(\gamma)}\, \psi_i^{(\beta\gamma)} \qquad i = 1, 2, 3 \tag{4.1}$$

where $w_i^{(\beta\gamma)}$ are the displacement components of the center of each subcell, and $\phi_i^{(\beta\gamma)}$ and $\psi_i^{(\beta\gamma)}$ give the linear dependence of the displacements on the local coordinates of the subcell. The microvariable $w_i^{(\beta\gamma)}$ is a function of global coordinates (x_1 , x_2 , x_3), and $\phi_i^{(\beta\gamma)}$ and $\psi_i^{(\beta\gamma)}$ are functions of x_2 and x_3 only. The superscripts β , γ indicate that the specified quantities belong to one of the subcells. No summation is implied by the repeated superscripts β or γ.

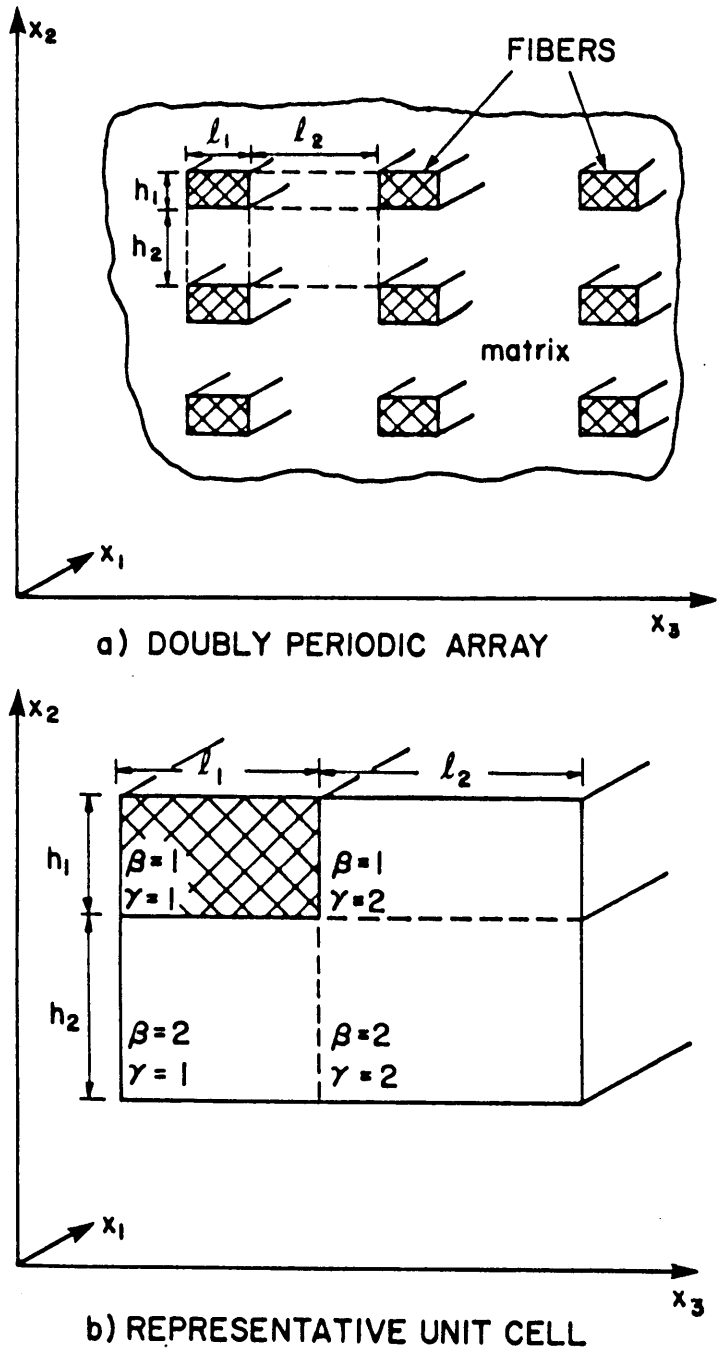

Figure 4. 1. The geometry and coordinate system of the micromechanics model

The components of the small strain tensor are given by

$$\varepsilon_{ij}^{(\beta\gamma)} = \frac{1}{2}\left[\, \partial_i u_j^{(\beta\gamma)} + \partial_j u_i^{(\beta\gamma)} \,\right] \qquad i, j = 1, 2, 3 \tag{4.2}$$

where $\partial_1 = \frac{\partial}{\partial x_1}$, $\partial_2 = \frac{\partial}{\partial \bar{x}_2^{(\beta)}}$ and $\partial_3 = \frac{\partial}{\partial \bar{x}_3^{(\gamma)}}$.

Under the assumption of perfect bonding between the fiber and matrix phases, the following displacement continuity conditions must be satisfied at the interface of each subcell in the representative cell,

$$u_i^{(1\gamma)}\Big|_{\bar{x}_2^{(1)} = \mp\frac{h_1}{2}} = u_i^{(2\gamma)}\Big|_{\bar{x}_2^{(2)} = \pm\frac{h_2}{2}},$$

$$u_i^{(\beta 1)}\Big|_{\bar{x}_3^{(1)} = \pm\frac{l_1}{2}} = u_i^{(\beta 2)}\Big|_{\bar{x}_3^{(2)} = \mp\frac{l_2}{2}}. \tag{4.3}$$

Imposing Eqn. (4.1) on an average basis, and performing a smoothing operation with respect to the global coordinates (x_1, x_2, x_3) [24], the displacement continuity conditions can be expressed in terms of the local microvariables as follows.

$$w_i^{(11)} = w_i^{(12)} = w_i^{(21)} = w_i^{(22)} \equiv w_i,$$

$$h_1\phi_i^{(1\gamma)} + h_2\phi_i^{(2\gamma)} = (h_1 + h_2)\frac{\partial w_i}{\partial x_2},$$

$$l_1\psi_i^{(\beta 1)} + l_2\psi_i^{(\beta 2)} = (l_1 + l_2)\frac{\partial w_i}{\partial x_3}. \tag{4.4}$$

The average composite strains are given in terms of the average subcell strains in the usual fashion.

$$\bar{\varepsilon}_{ij} = \frac{1}{V} \sum_{\beta,\gamma=1}^{2} V_{\beta\gamma}\, \varepsilon_{ij}^{(\beta\gamma)}, \tag{4.5}$$

where $V_{\beta\gamma} = h_\beta l_\gamma$ and $V = (h_1 + h_2)(l_1 + l_2)$.

Using Eqns. (4.1), (4.2) and (4.5), the average strains of the composite can be expressed in terms of the microvariables. This yields:

$$\bar{\varepsilon}_{ij} = \frac{1}{2}\left(\frac{\partial w_j}{\partial x_i} + \frac{\partial w_i}{\partial x_j}\right). \tag{4.6}$$

4.2.3 Stress Field

The traction continuity conditions at the interfaces of the subcells within the representative unit cell are given by

$$\sigma_{2i}^{(1\gamma)}\Big|_{\bar{x}_2^{(1)} = \pm\frac{h_1}{2}} = \sigma_{2i}^{(2\gamma)}\Big|_{\bar{x}_2^{(2)} = \mp\frac{h_2}{2}},$$

$$\sigma_{3i}^{(\beta 1)}\Big|_{\bar{x}_3^{(1)} = \pm\frac{l_1}{2}} = \sigma_{3i}^{(\beta 2)}\Big|_{\bar{x}_3^{(2)} = \mp\frac{l_2}{2}}. \tag{4.7}$$

The average stress components in the individual subcells are defined below,

$$S_{ij}^{(\beta\gamma)} = \frac{1}{V_{\beta\gamma}} \int_{-\frac{h_\beta}{2}}^{\frac{h_\beta}{2}} \int_{-\frac{l_\gamma}{2}}^{\frac{l_\gamma}{2}} \sigma_{ij}^{(\beta\gamma)}\, d\bar{x}_2^{(\beta)} d\bar{x}_3^{(\gamma)} \tag{4.8}$$

where $S_{ij}^{(\beta\gamma)}$ denote the components of the stress tensor.

Employing the equilibrium equations in each subcell,

$$\partial_j \ \sigma_{ji}^{(\beta\gamma)} \ = \ 0 \quad , \tag{4.9}$$

and incorporating these into the first order continuum theory, the traction continuity in an average sense [24] can be expressed in terms of average stresses in the subcells as follows:

$$\begin{aligned} S_{2i}^{(1\gamma)} \ &= \ S_{2i}^{(2\gamma)} \\ S_{3i}^{(\beta 1)} \ &= \ S_{3i}^{(\beta 2)} \end{aligned} \tag{4.10}$$

The average composite stresses are defined in terms of the average subcell stresses as in the case of the average composite strains.

$$\bar{\sigma}_{ij} \ = \ \frac{1}{V} \sum_{\beta,\gamma=1}^{2} V_{\beta\gamma} \ S_{ij}^{(\beta\gamma)}, \tag{4.11}$$

From Eqns. (4.5) and (4.11), it is seen that the required average stresses and strains are established in terms of the local subcell microvariables. The effective behavior of the composite can be determined once the relations between the average composite stresses $\bar{\sigma}_{ij}$ and the average composite strains $\bar{\varepsilon}_{ij}$ are found.

4.2.4 Average Stress-Strain Relations of the Constituents

The average stress-strain relations of the inelastic constituents in each of the subcells are established as follows. The total rate of strain of the material in the subcell $(\beta\gamma)$ is decomposed into elastic, thermal and inelastic terms in the form

$$\dot{\varepsilon}_{ij}^{(\beta\gamma)} \ = \ \dot{\varepsilon}_{ij}^{EL(\beta\gamma)} \ + \ \dot{\varepsilon}_{ij}^{T(\beta\gamma)} \ + \ \dot{\varepsilon}_{ij}^{PL(\beta\gamma)} \qquad i, j \ = \ 1, 2, 3 \tag{4.12}$$

For a transversely isotropic material in the elastic range, the stress is related to the strain as follows

$$\underset{\sim}{\sigma}^{(\beta\gamma)} = \underset{\sim}{C}^{(\beta\gamma)} \underset{\sim}{\varepsilon}^{EL(\beta\gamma)} \tag{4.13}$$

where

$$\underset{\sim}{\sigma}^{(\beta\gamma)} = [\sigma_{11}^{(\beta\gamma)}, \sigma_{22}^{(\beta\gamma)}, \sigma_{33}^{(\beta\gamma)}, \sigma_{12}^{(\beta\gamma)}, \sigma_{13}^{(\beta\gamma)}, \sigma_{23}^{(\beta\gamma)}],$$

$$\underset{\sim}{\varepsilon}^{EL(\beta\gamma)} = [\varepsilon_{11}^{EL(\beta\gamma)}, \varepsilon_{22}^{EL(\beta\gamma)}, \varepsilon_{33}^{EL(\beta\gamma)}, 2\varepsilon_{12}^{EL(\beta\gamma)}, 2\varepsilon_{13}^{EL(\beta\gamma)}, 2\varepsilon_{23}^{EL(\beta\gamma)}],$$

and

$$\underset{\sim}{C}^{(\beta\gamma)} = \begin{bmatrix} c_{11}^{(\beta\gamma)} & c_{12}^{(\beta\gamma)} & c_{12}^{(\beta\gamma)} & 0 & 0 & 0 \\ c_{12}^{(\beta\gamma)} & c_{22}^{(\beta\gamma)} & c_{23}^{(\beta\gamma)} & 0 & 0 & 0 \\ c_{12}^{(\beta\gamma)} & c_{23}^{(\beta\gamma)} & c_{22}^{(\beta\gamma)} & 0 & 0 & 0 \\ 0 & 0 & 0 & c_{44}^{(\beta\gamma)} & 0 & 0 \\ 0 & 0 & 0 & 0 & c_{44}^{(\beta\gamma)} & 0 \\ 0 & 0 & 0 & 0 & 0 & c_{66}^{(\beta\gamma)} \end{bmatrix}$$

The stiffness constants $c_{ij}^{(\beta\gamma)}$ in (4.13) are related to the engineering constants in the following manner (omitting the superindices $(\beta\gamma)$):

$$c_{11} = E_A + 4\kappa\nu_A^2,$$

$$c_{12} = 2\kappa\nu_A,$$

$$c_{22} = \kappa + 0.5E_T/(1 + \nu_T),$$

$$c_{23} = \kappa - 0.5E_T/(1 + \nu_T),$$

$$c_{44} = G_A,$$

$$c_{66} = (c_{22} - c_{23})/2,$$

$$\kappa = 0.25 E_A / [0.5(1 - \nu_T)(E_A / E_T) - \nu_A^2]. \tag{4.14}$$

where E_A, ν_A are the Young modulus and Poisson's ratio respectively, G_A is shear modulus, and E_T, ν_T are the transverse Young's modulus and Poisson's ratio.

The thermal strains are given by

$$\varepsilon_{ij}^{T(\beta\gamma)} = A_{ij}^{(\beta\gamma)} \Delta T, \tag{4.15}$$

where

$$A_{ij}^{(\beta\gamma)} = [\alpha_{11}^{(\beta\gamma)}, \alpha_{22}^{(\beta\gamma)}, \alpha_{11}^{(\beta\gamma)}, 0, 0, 0]$$

with $\alpha_{11}^{(\beta\gamma)}$ and $\alpha_{22}^{(\beta\gamma)}$ being the axial and transverse thermal expansion coefficients of the material occupying the subcell $(\beta\gamma)$.

The plastic strains in Eqn. (4.12) are determined using the unified theory of plasticity proposed by Bodner [36]. This theory has been chosen because no yield criterion is required, and thus it is not necessary to differentiate between loading and unloading conditions. The same governing equation can be directly used in all stages of loading and unloading, greatly simplifying the computational procedure.

According to this theory, the inelastic strain rates for elastoplastic material with isotropic hardening are given by the isotropic form of the Prandtl-Reuss flow rule

$$\dot{\varepsilon}_{ij}^{PL(\beta\gamma)} = \Lambda_{\beta\gamma} s_{ij}^{(\beta\gamma)}, \tag{4.16}$$

where $s_{ij} = \sigma_{ij} - \delta_{ij}\sigma_{kk}/3$ are the deviators of the stresses and δ_{ij} is the Kronecker delta (omitting superindices β γ).

An explicit form of the flow rule function Λ is given by

$$\Lambda = D_0 \exp \{ -\hat{n} [Z^2 / (3 J_2)]^n \} / J_2^{1/2} , \tag{4.17}$$

where $\hat{n} = 0.5(n+1)/n$ and $J_2 = s_{ij}s_{ij}/2$ is the second invariant of the stress deviators s_{ij} , D_0 , n are inelastic material parameters, and Z is a state variable given by,

$$Z = Z_1 + (Z_0 - Z_1) \exp [- m W_p / Z_0]. \tag{4.18}$$

where W_p is the plastic work.

Equations (4.17) - (4.18) contain five parameters, Z_0, Z_1, m, n and D_0, which characterize the behavior of the material in inelastic range. Generally speaking, Z_0 and Z_1 specify yield stress and ultimate stress of the material respectively, and m controls the hardening rate from Z_0 to Z_1. The parameter n governs the strain rate.

Incorporating Bodner's constitutive theory into the present first order continuum formulation in an average sense, the evolution equations for average plastic strains $L_{ij}^{(\beta\gamma)}$ in each subcell are given by

$$\dot{L}_{ij}^{(\beta\gamma)} = \Lambda_{\beta\gamma} \hat{S}_{ij}^{(\beta\gamma)} \tag{4.19}$$

where $\hat{S}_{ij}^{(\beta\gamma)}$ are the stress deviators of $S_{ij}^{(\beta\gamma)}$.

The explicit relations between the average stresses in the subcells and the average strains of the composite can be obtained by substituting Eqn. (4.13) in Eqn. (4.8) and using Eqn. (4.12). These relations are

$$S_{11}^{(\beta\gamma)} = c_{11}^{(\beta\gamma)} \bar{\varepsilon}_{11} + c_{12}^{(\beta\gamma)} (\phi_2^{(\beta\gamma)} + \psi_3^{(\beta\gamma)}) - d_{11}^{(\beta\gamma)} \Delta T - 2\mu_{\beta\gamma} L_{11}^{(\beta\gamma)}$$

$$S_{22}^{(\beta\gamma)} = c_{12}^{(\beta\gamma)} \bar{\varepsilon}_{11} + c_{22}^{(\beta\gamma)} \phi_2^{(\beta\gamma)} + c_{23}^{(\beta\gamma)} \psi_3^{(\beta\gamma)} - d_{22}^{(\beta\gamma)} \Delta T - 2\mu_{\beta\gamma} L_{22}^{(\beta\gamma)}$$

$$S_{33}^{(\beta\gamma)} = c_{12}^{(\beta\gamma)}\bar{\varepsilon}_{11} + c_{23}^{(\beta\gamma)}\phi_2^{(\beta\gamma)} + c_{22}^{(\beta\gamma)}\psi_3^{(\beta\gamma)} - d_{33}^{(\beta\gamma)}\Delta T - 2\mu_{\beta\gamma}L_{33}^{(\beta\gamma)}$$

$$S_{12}^{(\beta\gamma)} = c_{44}^{(\beta\gamma)}\left(\frac{\partial w_2}{\partial x_1} + \phi_1^{(\beta\gamma)}\right) - 2c_{44}^{(\beta\gamma)}L_{12}^{(\beta\gamma)}$$

$$S_{13}^{(\beta\gamma)} = c_{44}^{(\beta\gamma)}\left(\frac{\partial w_3}{\partial x_1} + \psi_1^{(\beta\gamma)}\right) - 2c_{44}^{(\beta\gamma)}L_{13}^{(\beta\gamma)}$$

$$S_{23}^{(\beta\gamma)} = c_{66}^{(\beta\gamma)}\left(\phi_3^{(\beta\gamma)} + \psi_2^{(\beta\gamma)}\right) - 2c_{66}^{(\beta\gamma)}L_{23}^{(\beta\gamma)} \tag{4.20}$$

where

$$d_{11}^{(\beta\gamma)} = c_{11}^{(\beta\gamma)}\alpha_{11}^{(\beta\gamma)} + 2c_{12}^{(\beta\gamma)}\alpha_{22}^{(\beta\gamma)},$$

$$d_{22}^{(\beta\gamma)} = c_{12}^{(\beta\gamma)}\alpha_{11}^{(\beta\gamma)} + \left(c_{22}^{(\beta\gamma)} + c_{23}^{(\beta\gamma)}\right)\alpha_{22}^{(\beta\gamma)},$$

$$d_{33}^{(\beta\gamma)} = d_{22}^{(\beta\gamma)}$$

and $\mu_{\beta\gamma} = 0$ for perfectly elastic anisotropic materials in the elastic region, while $\mu_{\beta\gamma}$ stands for the shear modulus for elastoplastic isotropic constituents in the elastic region.

4.2.5 Explicit Overall Stress-Strain Relations of the Composite

Using the displacement continuity conditions, Eqn. (4.4), and traction continuity conditions, Eqn. (4.10), the necessary unknown microvariables are obtained in terms of the material properties and geometrical dimensions of the constituents. The required effective stress-strain relations of unidirectional fiber-reinforced material are subsequently established in the following explicit form:

$$\bar{\sigma}_{11} = b_{11}\bar{\varepsilon}_{11} + b_{12}\bar{\varepsilon}_{22} + b_{13}\bar{\varepsilon}_{33} - \Gamma_{11}\Delta T - H_{11}$$

$$\bar{\sigma}_{22} = b_{12}\bar{\varepsilon}_{11} + b_{22}\bar{\varepsilon}_{22} + b_{23}\bar{\varepsilon}_{33} - \Gamma_{22}\Delta T - H_{22}$$

$$\bar{\sigma}_{33} = b_{13}\,\bar{\varepsilon}_{11} + b_{23}\,\bar{\varepsilon}_{22} + b_{33}\,\bar{\varepsilon}_{33} - \Gamma_{33}\,\Delta T - H_{33}$$

$$\bar{\sigma}_{12} = 2\,b_{44}\,\bar{\varepsilon}_{12} - H_{12}$$

$$\bar{\sigma}_{13} = 2\,b_{55}\,\bar{\varepsilon}_{13} - H_{13}$$

$$\bar{\sigma}_{23} = 2\,b_{66}\,\bar{\varepsilon}_{23} - H_{23} \qquad (4.21)$$

or in matrix form

$$\underset{\sim}{\bar{\sigma}} = \underset{\sim}{E}\,(\underset{\sim}{\bar{\varepsilon}} - \underset{\sim}{\bar{\varepsilon}}^{(PL)} - \underset{\sim}{U}\,\Delta T) \qquad (4.22)$$

where $\underset{\sim}{\bar{\varepsilon}}^{(PL)} = \underset{\sim}{B}^{-1}\underset{\sim}{H}$ and $\underset{\sim}{U} = \underset{\sim}{B}^{-1}\underset{\sim}{\Gamma}$, in which $\underset{\sim}{B} = [b_{ij}]$ is a 6 x 6 matrix, $\underset{\sim}{H} = [H_{11}, H_{22}, H_{33}, H_{12}, H_{13}, H_{23}]$ and $\underset{\sim}{\Gamma} = [\Gamma_{11}, \Gamma_{22}, \Gamma_{33}, 0, 0, 0]$

The coefficients $\underset{\sim}{B}$ and $\underset{\sim}{H}$ are in fact the elastic constants and inelastic terms in the elastoplastic average constitutive relations of the composite. The complete expressions for $\underset{\sim}{B}$ and $\underset{\sim}{H}$ can be found in reference [28]. The coefficients $\underset{\sim}{\Gamma}$ are the effective thermal expansion coefficients of the composite, which are given by

$$V\Gamma_{11} = Q_2\,[\,d_{22}^{(m)} - d_{22}^{(f)}\,] + Q_3\,[\,d_{22}^{(m)} - d_{22}^{(f)}\,] + [\,\nu_{11}\,d_{11}^{(f)} + (\,\nu_{12} + \nu_{21} + \nu_{22}\,)\,d_{11}^{(m)}\,]$$

$$V\Gamma_{22} = Q'_2\,[\,d_{22}^{(m)} - d_{22}^{(f)}\,] + Q'_3\,[\,d_{22}^{(m)} - d_{22}^{(f)}\,] + [\,\nu_{11}\,d_{22}^{(f)} + (\,\nu_{12} + \nu_{21} + \nu_{22}\,)\,d_{22}^{(m)}\,]$$

$$V\Gamma_{33} = Q''_2\,[\,d_{22}^{(m)} - d_{22}^{(f)}\,] + Q''_3\,[\,d_{22}^{(m)} - d_{22}^{(f)}\,] + [\,\nu_{11}\,d_{22}^{(f)} + (\,\nu_{12} + \nu_{21} + \nu_{22}\,)\,d_{22}^{(m)}\,] \ ,$$

where 'f' , 'm' denote fiber and matrix, respectively. The expressions for Q_1 , Q_2 , ... can also be found in the Appendix of reference [28].

The overall thermal elastoplastic behavior of the composite is governed by the average stress-strain relations of the composite given in Eqn. (4.21). These equations consist of 9 independent elastic constants, b_{11}, b_{12}, b_{13}, b_{22}, b_{23}, b_{33}, b_{44}, b_{55} and b_{66}, so that the composite effectively behaves as an

orthotropic material. For square fibers with equal spacing, $h_1 = l_1$ and $h_2 = l_2$, the number of these constants are reduced to 6 since $b_{12} = b_{13}$, $b_{22} = b_{33}$ and $b_{44} = b_{55}$. In order to obtain the desired transversely isotropic characteristics, the following operation was performed.

$$\underset{\sim}{E} = \frac{1}{\pi}\int_0^{\pi} \underset{\sim}{B}'(\xi)d\xi \tag{4.23}$$

where $\underset{\sim}{B}'(\xi)$ is the transformed form of $\underset{\sim}{B}$ in the coordinate system rotated by an angle ξ about the x_1-axis, $\underset{\sim}{E} = [e_{ij}]$ are the resulting elastic constants of a transversely isotropic material. The elements of symmetric matrix $\underset{\sim}{E}$ are expressed in terms of the elements of $\underset{\sim}{B}$ in the form

$$e_{11} = b_{11}$$

$$e_{12} = e_{13} = (b_{12} + b_{13})/2$$

$$e_{22} = e_{33} = 3(b_{22} + b_{33})/8 + b_{23}/4 + b_{66}/2$$

$$e_{23} = (b_{22} + b_{33})/8 + 3b_{23}/4 - b_{66}/2$$

$$e_{44} = e_{55} = (b_{44} + b_{55})/2$$

$$e_{66} = (e_{22} - e_{23})/2 \tag{4.24}$$

In applications, the model requires the input of the thermal elastoplastic properties of the constituents and the ratio of fiber reinforcement. The effective stress-strain relations in the principal material coordinate system can be directly determined from Eqn. (4.21) with the help of a computer program. The calculations involve the incorporated evolution equations (4.19), so that a step by step incremental procedure is needed for the computation of inelastic response. Once the effective behavior in the principal material coordinate system is obtained, the stress-strain relations in the laminate coordinate system can be determined by transformation theory. Neglecting the inelastic

and thermal terms, the effective elastic engineering constants of the composite can be computed by inverting Eqn. (4.14) with e_{ij} replacing c_{ij}.

In conclusion, the model provides a low-cost computer programming and a straight forward implementation, i.e. specification of the properties of the constituents and fiber volume fraction results in the effective properties of the composite expressed by the average stress-strain relations of the representative cell. This model can be applied to arbitrary loading situations, and no yield criterion and loading or unloading conditions are required.

4.3 In-Situ Properties and Residual Stresses

A successful semi-inverse methodology for correlating the micromechanics predictions and experimental results of tests carried out on unidirectional boron/aluminum composite has been developed by Pindera, Aboudi, and Herakovich in reference [29]. The methodology involves backing out the unknown in-situ properties from selected experimental results including the residual stresses which are obtained from the yield stress of monotonic tension and compression test results.

In the above investigation, good predictions for the effective elastic parameters were obtained using the bulk properties of boron fiber and 6061-O aluminum. However, in order to obtain good correlation in the nonlinear region the following procedure was employed. Based on the assumption that during the fabrication process the bulk properties of the boron fiber are not significantly affected, and that only the temper condition of the aluminum matrix is altered, the in-situ yield stress and nonlinear properties of the matrix were backed out by correlating the predicted axial shear response of a 10° off-axis coupon with the experimental results. This procedure is possible since the temper condition of 6061 aluminum only affects its yield stress and nonlinear properties [37].

The residual stresses in each phase were subsequently expressed in terms of an equivalent temperature which resulted in the observed different yield stresses in tension and compression. The equivalent temperature was backed out by matching the yield stress of monotonic tension and compression test results of the 0° specimen, for which a higher yield stress was observed experimentally in compression, with the analytical predictions. The choice of the 0° specimen was motivated by the large difference in the yield stress in tension and compression which was significantly greater than for other tested configurations.

Using the above "backed-out" in-situ properties of the aluminum and the equivalent temperature of residual stresses, good agreement was obtained between the analytical and experimental results for longitudinal, transverse and off-axis loading conditions.

In correlating the analytical and experimental results for the present P100/6061 graphite/aluminum composite, the above semi-inverse methodology was employed. However, the determination of the actual in-situ properties of the constituents and residual stresses is more difficult in the present case. The initial difficulty encountered was the lack of reliable data for Thornel P100-2K graphite fiber. This type of graphite fiber has been developed recently and is thought to be transversely isotropic with perfectly elastic characteristics. Five engineering elastic constants are required to characterize the material, but only one constant, axial Young's modulus, is available in the open literature [38].

Since the present study is primarily concerned with the nonlinear response of the investigated unidirectional composite, the elastic constants of graphite fiber were backed out using the micromechanics model and the test data of reference [12] and 6061-O aluminum. The test results given in reference [12] only provide the in-plane elastic moduli, E_{11}^{*}, E_{22}^{*} , ν_{12}^{*} and G_{12}^{*} . A value of 0.45 was thus hypothetically assigned to ν_{13}^{*} which was also used for ν_{13} of the Thornel T-50 graphite fiber.

The in-situ yield and nonlinear properties of the aluminum matrix were subsequently backed out by matching the analytical predictions with the experimentally obtained shear response of the 0°

Iosipescu specimen. The 0° Iosipescu specimen provided more information on the nonlinear behavior of the material than other tested configurations [12]. The backed-out in-situ nonlinear characteristics of the aluminum matrix were expressed in terms of the five parameters of Bodner's unified plasticity theory.

The elastic constants of the graphite fiber and the in-situ nonlinear parameters of the aluminum matrix are given in Table 4.1. The employed experimental data of the composite is also included for reference. The backed-out in-situ stress-strain curve of the aluminum matrix along with the stress-strain curve of 6061-O aluminum are plotted in Fig. 4.2. It is seen that the stress-strain curve for the obtained in-situ aluminum matrix has a bilinear response with a higher yield stress and lower ultimate stress than that of the bulk 6061-O aluminum.

Table 4.1 Material properties of the constituents

Material	E_{11} (msi)	E_{22} (msi)	ν_{12}	ν_{13}	G_{12} (msi)
Graphite/Aluminum Composite **	58.4	3.5	0.291	0.45***	2.43
P100-2K Graphite Fiber *	112	0.88	0.133	0.477	1.42

	E (msi)	ν	D_0^{-1} (sec)	Z_0 (ksi)	Z_1 (ksi)	m	n
6061 Aluminum	10.5	0.33	10^{-4} *	10.9 *	16 *	40 *	10 *

* Backed-Out Data
** Reference [12]
*** Assigned Number

The equivalent temperature of the residual stresses could not be determined from the available test results for the present graphite/aluminum composite. To back out the equivalent temperature, the tension and compression test results of 0° configuration are considered as the most natural

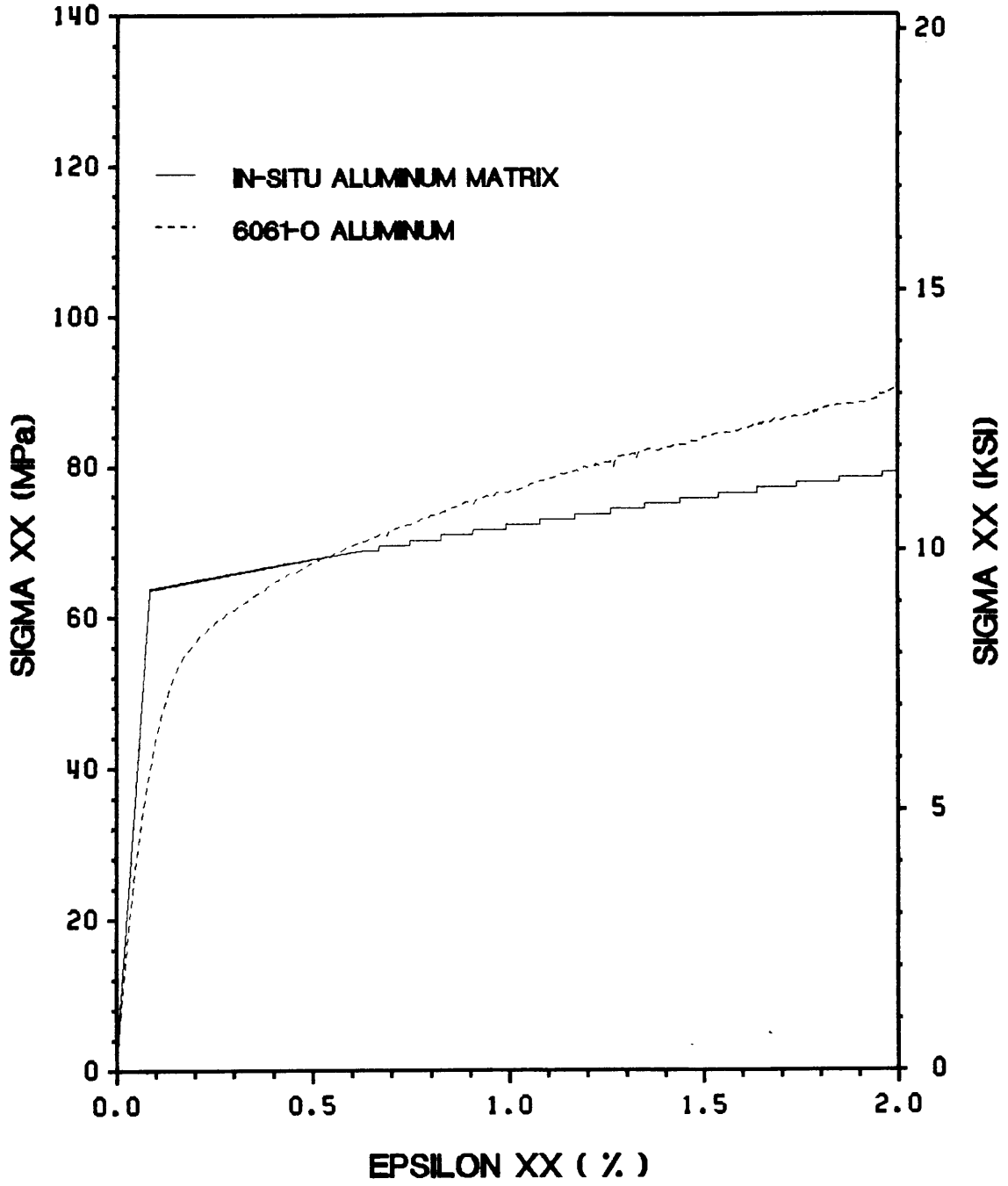

Figure 4. 2. Backed-out response of the in-situ aluminum matrix.

candidates. However, from the monotonic tension and compression test results of 0° specimens illustrated in Fig. 4.3, a higher tensile yield stress is observed. This phenomenon is physically contradictory with the tensile residual stresses in the aluminum matrix induced during the cool-down [12]. Another candidate for determining the equivalent temperature is the 90° specimen. In Fig. 3.2, it is seen that the 90° specimen failed in a premature manner in tension. This is believed to be due to the poor interface of the precursor wires. Thus the apparent yield stress measured in tension might be more representative of the precursor wire-to-wire interfacial strength. Consequently, the methodology for determining the equivalent temperature of the residual stresses was not employed for the present material.

4.4 Comparison of Analytical and Experimental Results

In the micromechanics analysis, the "backed-out" in-situ properties of the constituents listed in Table 4.1 were employed along with the value of 47% for the fiber volume and an assumption of isotropic hardening for the aluminum matrix. Because of the difficulty in determining the residual stresses, they were not included in the analysis. For axial, transverse and in-plane shear responses, incremental strain loading was used. For the off-axis response, incremental stress loading was employed. In the tension-compression cyclic loading case, the reversal points were based on the corresponding strain level.

Comparisons of the analytical and experimental results for monotonic tension are illustrated in Figs. 4.4 - 4.6. The predicted axial and off-axis response are depicted in Fig. 4.4 along with the experimental results. It is seen that excellent agreement was obtained in the elastic range for the 0° specimen. This is expected since the elastic moduli of the graphite fiber were backed out using the same model. The correlation in the nonlinear response is also good for this configuration.

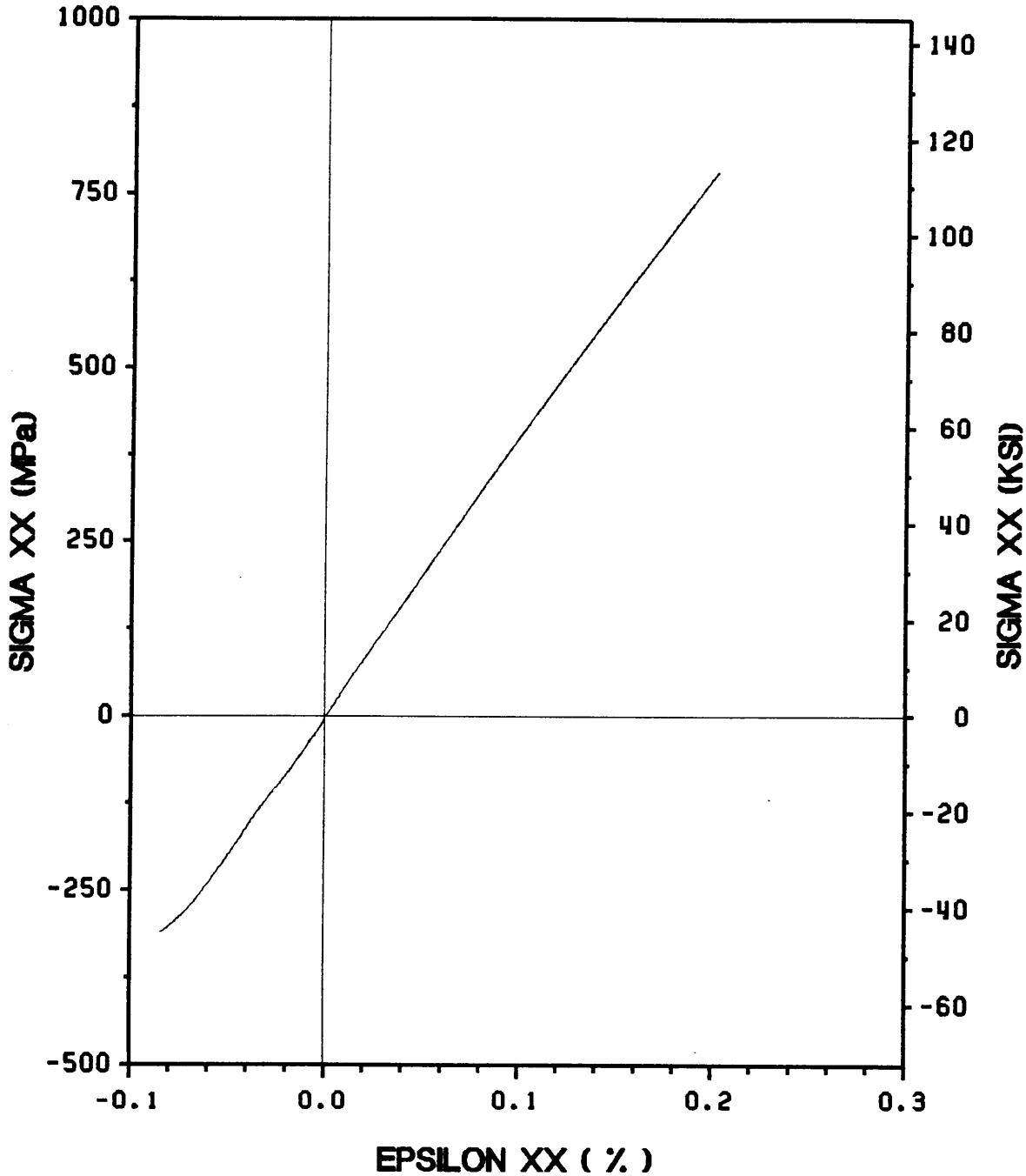

Figure 4. 3. Axial response obtained in monotonic tension and compression tests, reference [12,13].

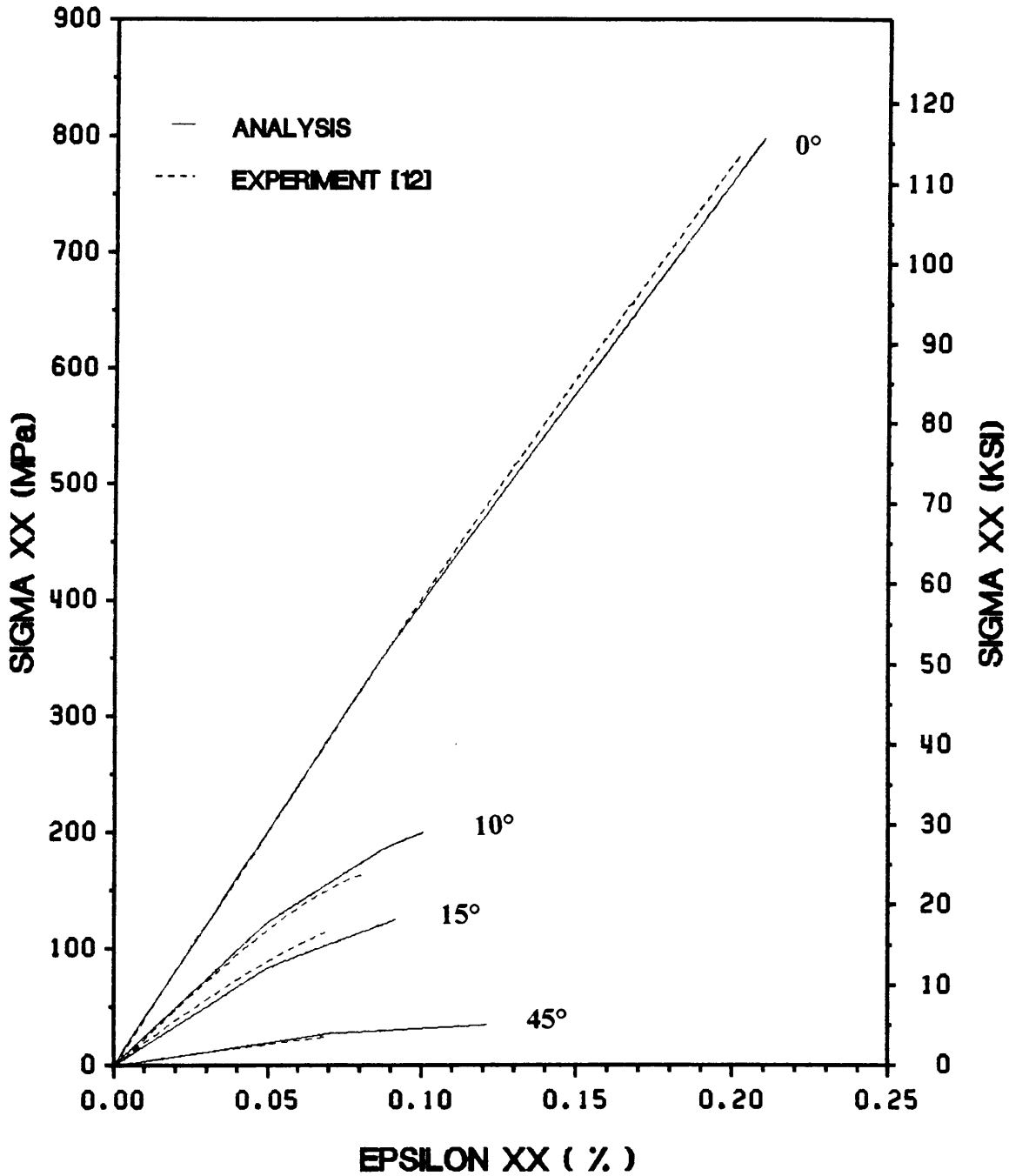

Figure 4. 4. Comparison of the axial and off-axis response.

For the remaining off-axis specimens, it is seen that good agreement was also obtained in the elastic range. The relatively higher slope in the experimental result of 15° specimen could be caused by end-constraint effects. For all the off-axis specimens, the experimental results indicate lower yield stress than those predicated by the analytical model, but the difference is not pronounced. This may be due to the influence of residual stresses and poor interface between the precursor wires. It is seen that good correlation was also obtained for the off-axis configurations in the nonlinear region.

It is noted that the predicted stress-strain curves have apparent kinks. Those kinks are believed to be cause by the discontinuity in the response curve of the aluminum matrix modeled by Bodner's plasticity theory. Smooth analytical curves can be obtained if the kink in the response curve of aluminum matrix is eliminated.

The analytical and experimental results of the transverse response are presented in Fig. 4.5. Good agreement in the elastic response is expected since the backed-out properties of the graphite fiber were used. The small difference appears in this comparison because the average value of E_{22}^{*} was used, and the presented experimental curve is a typical one. It is seen that some nonlinearity exists in the experimental result, whereas the predicted curve remains linear up to the corresponding failure stress. The low yield and ultimate stress in the experimental result is believed mostly to be caused by poor interface between the precursor wires as cited previously.

The predicted shear responses obtained for selected off-axis specimens are included in Fig. 4.6 with the experimental results. It is noted that the Iosipescu response was employed in the backed-out procedure, thus the correlation, not surprisingly, is good. For the remaining specimen configurations, good agreement was obtained in the elastic range, whereas for the nonlinear behavior, the experimental results do not provide sufficient information for comparison.

The comparison of the analytical and experimental results for the present tension-compression cyclic tests is illustrated in Figs. 4.7 - 4.10. In Fig. 4.7 the predicted and experimental stress-strain

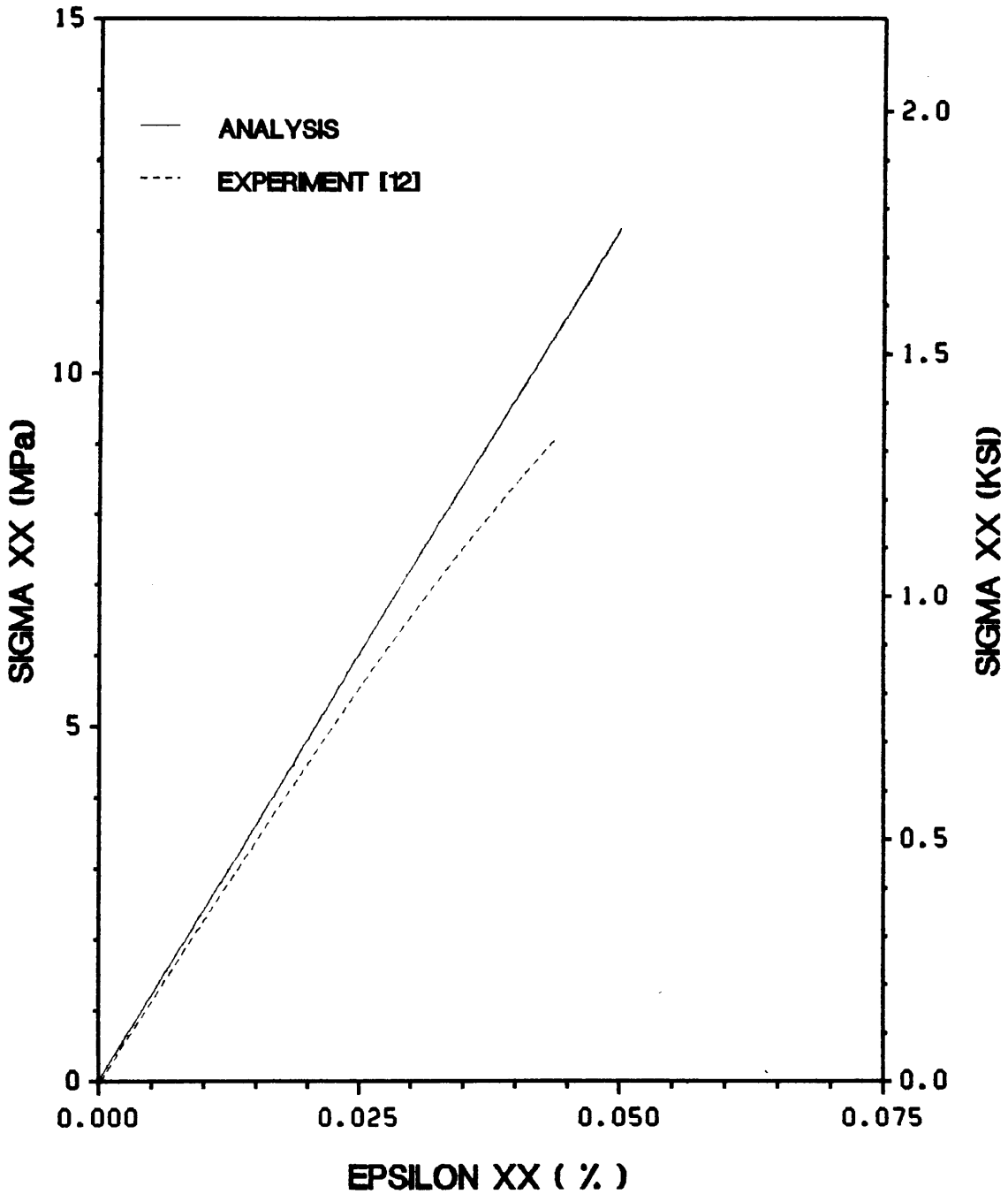

Figure 4. 5. Comparison of the transverse response.

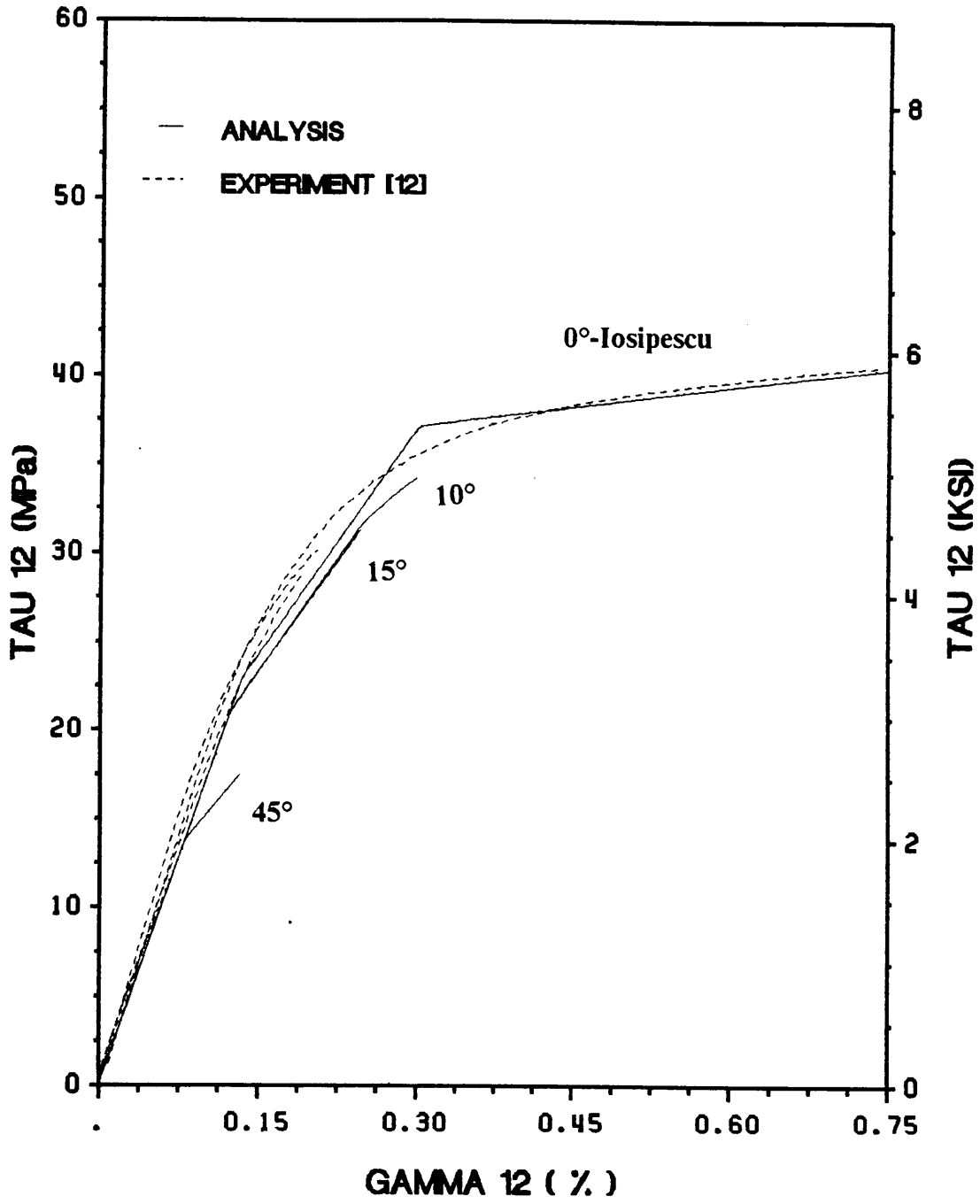

Figure 4. 6. Comparison of the shear response.

curves of the 15° specimen under tension-compression-tension loading cycle are given. It is seen that fairly good agreement was obtained for the entire loading path. The analysis predicted a lower initial stiffness as in the case of monotonic tension (see Fig. 4.4). In the initial stage of tensile loading, the analytical response remains elastic up to the reversal point while the experimental curve shows evidence of yielding. During the subsequent compressive loading, good correlation for the compressive yield stress was obtained while more plastic strain was predicted by the micromechanics model. In subsequent unloading and reloading in tension, the model predicts lower yield stress than initially obtained (i.e. kinematic hardening effects) and more plastic strain than observed in the experiment.

Examining the analytical results for the entire loading cycle, it is seen that the yield stress exhibits kinematic hardening behavior. It is recalled that in the analysis, isotropic hardening for the aluminum matrix was employed. The kinematic hardening behavior of the composite is not due to the hardening features of the aluminum matrix but it is caused by the geometric constraint of the elastic fibers. The mechanically induced residual stresses in each phase of the composite are the primary mechanisms that cause the kinematic hardening phenomenon of the composite. In experimental results, the influence of the secondary dissipative mechanisms results in the slope changes in the unloading-reloading response. The subsequent yield stress cannot be easily defined from the present experimental results.

The predicted stress-strain curve for the 15° specimen under compression-tension-compression loading cycle as well as the experimental results are included in Fig. 4.8. It is seen that fairly good agreement was also obtained for this loading path. The analysis also predicted a lower initial stiffness as that in the loading cycle discussed above. During the initial compressive loading, the initial yield stress was well predicted by the model, however, more plastic strain was observed in the analysis. It is noted that kinematic hardening behavior was also exhibited in the analytical results.

In Fig. 4.9, the comparison of the analytical predictions and experiment for the 90° specimen under tension-compression-tension loading cycle is presented. The analysis predicted a lower initial

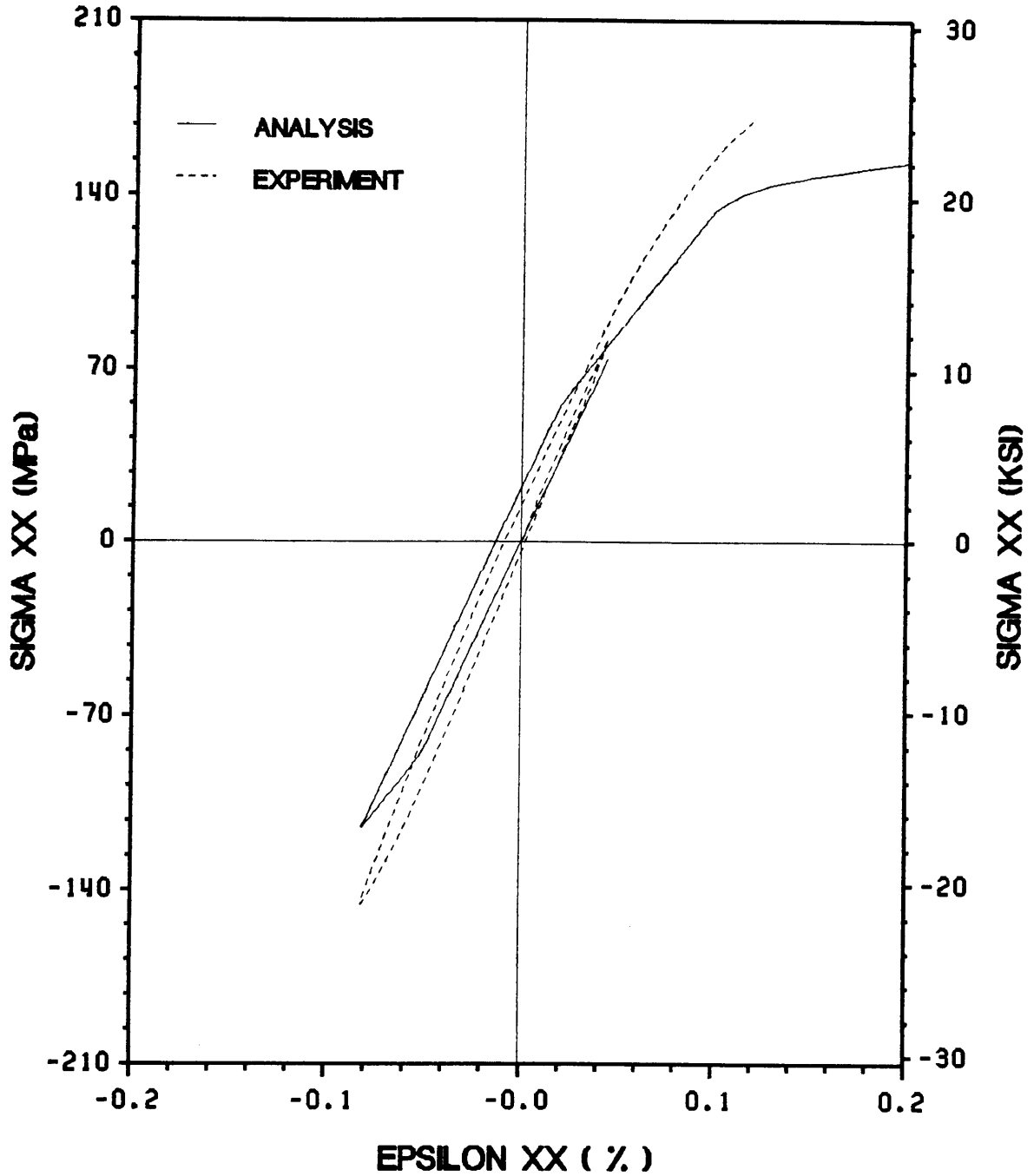

Figure 4. 7. Comparison for 15° specimen under tension-compression-tension cyclic loading at room temperature

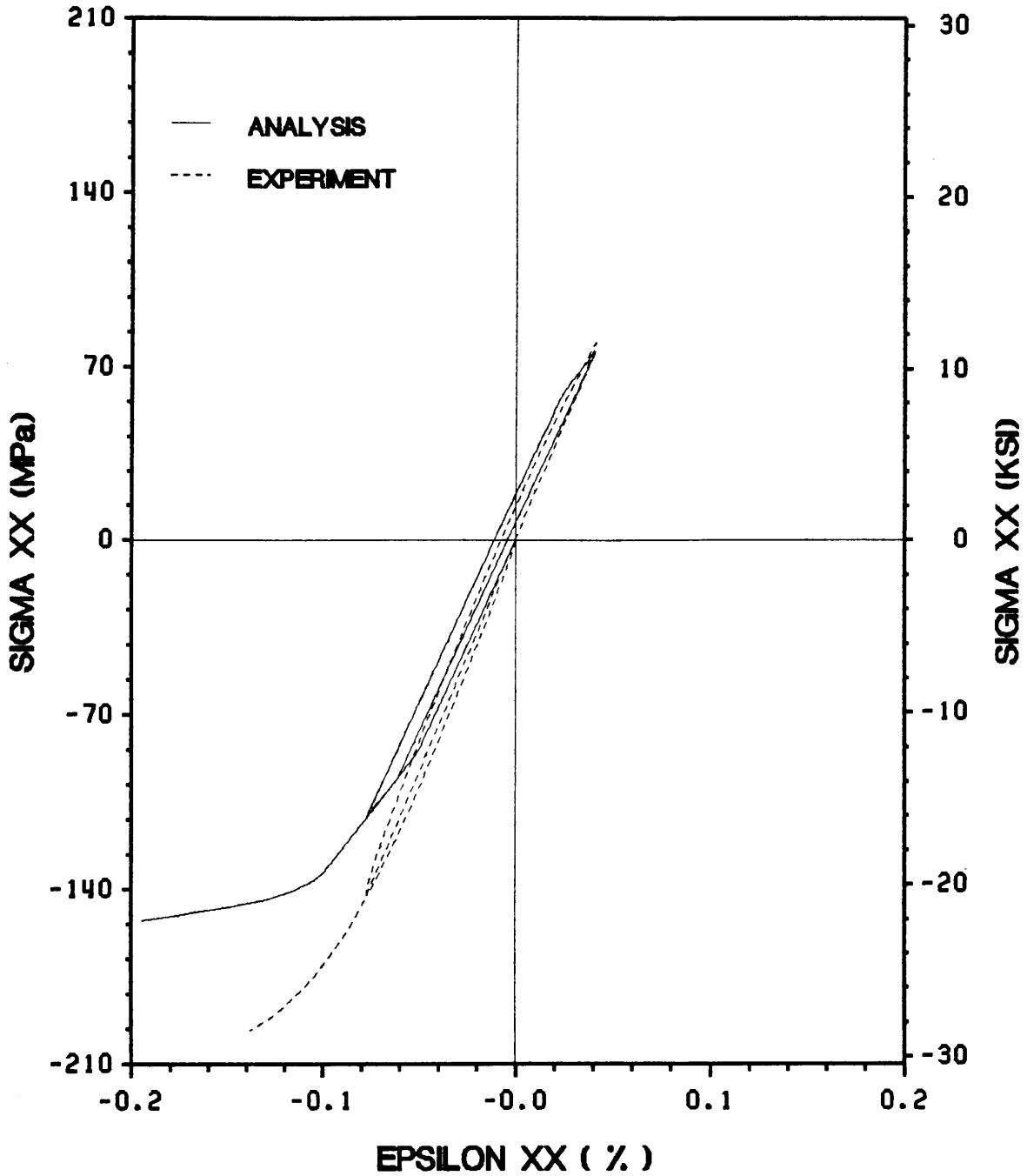

Figure 4. 8. Comparison for 15° specimen under compression-tension-compression cyclic loading at room temperature

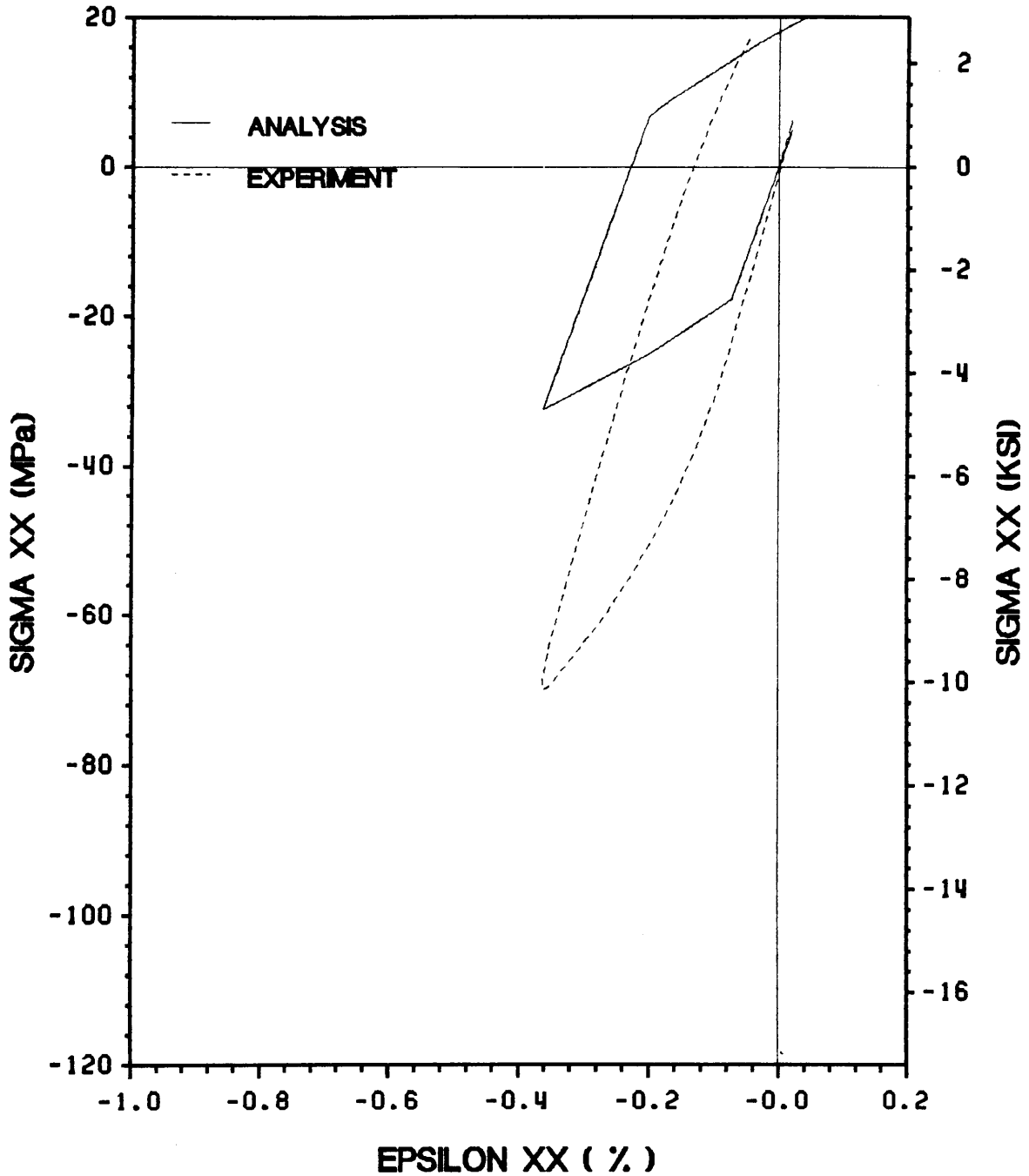

Figure 4. 9. Comparison for 90° specimen under tension-compression-tension cyclic loading at room temperature

stiffness. This may be explained by the scatter of the experimental data due to different source panels of the specimens (recall that the monotonic test results [12] were used in the back-out procedure). In the subsequent compressive loading, it is seen that apparently lower subsequent yield stress and significantly more plastic strain were predicted by the micromechanics model. For the entire cyclic response, the material behavior observed in the experiment is not well predicted by the model. It will be recalled that secondary dissipative mechanisms, which appear to be significant for the 90° configuration under compressive loading, were not taken into account in the theory. These secondary dissipative mechanisms arise because of the inherent defects in the material microstructure.

The comparison of the response of 90° specimen under compression-tension-compression loading cycle with the predictions of the micromechanics model is given in Fig. 4.10. As in the loading cycle discussed above, apparently lower initial yield stress and more plastic strain were also predicted by the micromechanics model for this loading condition. Poor correlation between the experiment and analysis was obtained for this loading path. It is noted that the trend of the kinematic hardening in the analysis is also evident in this case.

Comparing the analytical and experimental results described above, it is observed that good agreement was obtained for the monotonic tension loading. For the tension-compression cyclic results, fairly good correlation was obtained for 15° specimens, but poor for 90° specimens. The discrepancy in the correlation could be caused by the following factors.

1. The end-constraint effects for off-axis specimens were not taken into account in the model. This results in higher initial moduli observed in the experimental data in comparison with the predictions of the analytical model.

2. The influence of secondary dissipative mechanisms observed in the experiment was not considered in the analysis.

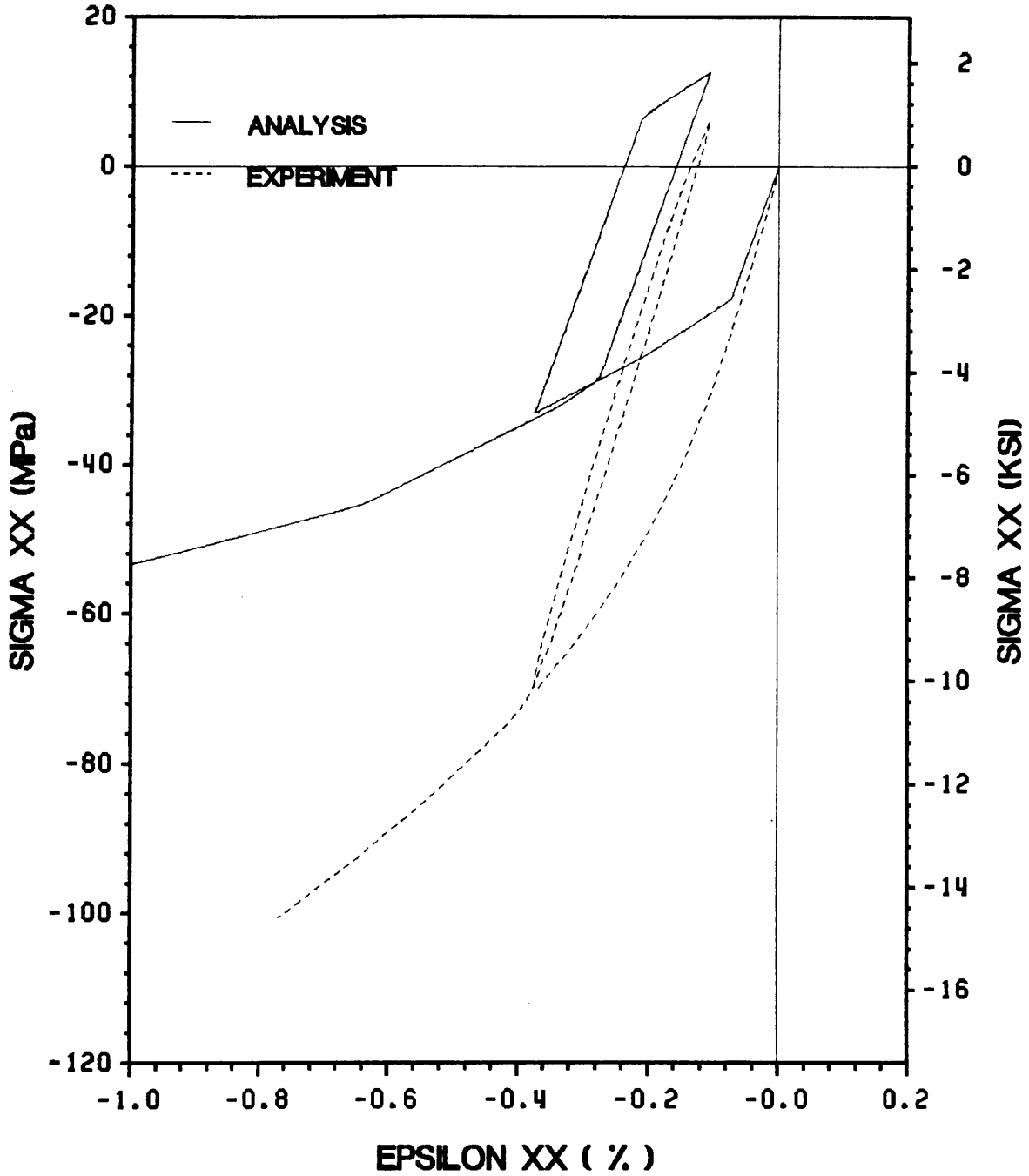

Figure 4. 10. Comparison for 90° specimen under compression-tension-compression cyclic loading at room temperature

3. Residual stresses induced in cooling process were not included in the analysis.

4. Material scatter in the experimental results.

Further discussion will be presented in Chapter 5.

Chapter 5 Discussion

Further discussion of the material response observed in the experiment and the correlation between the experimental and analytical results are presented in the following.

Comparing the experimentally obtained elastic moduli of the 15° off-axis specimens with the predictions of the transformation theory, it is observed that the end-constraint effects are significant. The end constraints introduce an error in the determination of the measured elastic parameters which results in higher apparent values of the elastic moduli than the values predicted by the transformation theory. In correlating the end-constraint analysis, Pagano-Halpin model and FEM analysis, with the experimental results, it has been demonstrated in Section 3.3.1.1 that no quantitative agreement was obtained. The FEM analysis with the second boundary condition which yields the most compliant clamping situation, gives the best predictions, but it still overestimates the end-constraint effects. Due to the difficulty of modelling the actual boundary conditions for the present specimen with low aspect ratio, quantitative corrections of the experimental results obtained from low off-axis configurations cannot be easily obtained.

Comparing the cyclic tensile and compressive response of the 15° and 90° specimens in Fig. 3.3 and Fig. 3.4 respectively, it is seen that significant hysteresis loops occur in compression for both configurations. The tensile response is predominantly elastoplastic, whereas the compressive

response involves the mechanisms of plasticity and secondary dissipative phenomenon. The secondary dissipative mechanisms are believed to be caused by the inherent defects in the material's microstructure. These defects are voids and weak interfaces between the individual wires (see Fig. 2.7). In compression, the voids close up; thus resulting in the geometrical change of the material's microstructure. In addition, friction and slippage between the individual precursor wires may be severe under this loading condition. In tension, on the other hand, the voids open up; thus less friction and slippage takes place between the individual precursor wires. Therefore, more energy loss and hysteresis phenomenon appear in compression. The hysteresis phenomenon is more evident for the 90° specimens than the 15° specimens. In Fig. 5.1, it is seen that for the 15° configuration, σ_{22} appears to be a relatively small component of the stress state. Therefore, closing of the voids is not so significant for this configuration. On the other hand, for the 90° configuration, the material is subjected to transverse loading; thus the void closure tends to be severe for this configuration.

Reviewing the experimental results outlined in Section 3.2, it is seen that for 90° specimens the ultimate stress in tension and compression is significantly different. Referring to Fig. 2.7, it is apparent that the poor interface between the adjacent wires and inherent voids exist in the material's structure. When the specimen is subjected to transverse tensile loading, it is very likely that the interfacial bond is damaged. Hence, the specimen fails in a premature manner under tension. On the other hand, when the specimen is subjected to compressive loading, the inherent voids tend to deform and close up. This increases the density of the material and results in a much higher ultimate stress and stiffer response in the nonlinear region in compression. For 15° off-axis specimens, the difference between tensile and compressive strength was not so pronounced. It is conjectured that since σ_{22} is a relatively small component of the stress state for the 15° configuration, the debonding of the weak interface is not so significant for this configuration.

From the experimental results at the different temperatures, it was observed that the initial yield stress in tension increased with increase of temperature, while the magnitude of the initial yield stress in compression decreased with increase of temperature. This phenomenon is believed to be

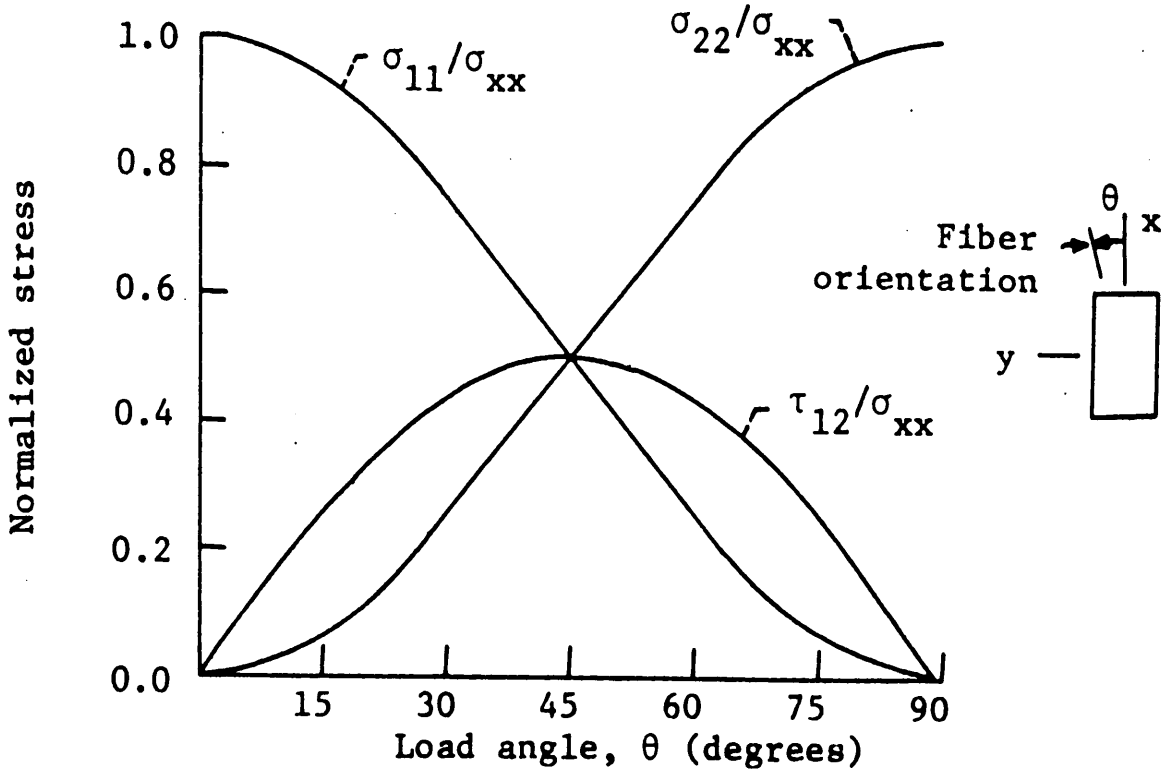

Figure 5. 1. Resolved stress components in the lamina coordinate system, reference [39].

due to thermally induced residual stresses caused by the mismatch of the coefficient of thermal expansion of the constituents. At low temperature, tensile residual stresses were induced in the matrix, thus the yield stresses were translated down in the compression direction. On the other hand, the yield stresses were translated up in the tension direction at high temperature.

In correlating analytical and experimental results, good agreement was obtained for monotonic tension. For tension-compression cyclic loading, the correlation is fair for 15° specimens but poor for 90° specimens. This is because the experimentally observed tensile response is dominated by plasticity, thus the micromechanics analysis is applicable for monotonic tension. It is recalled that the inherent voids of the material's structure were not taken into account in the analysis. However, the properties of the graphite fiber and the nonlinear properties of the aluminum matrix were backed out from the experimental results of the composite. Thus the influence of the voids has been reflected in the backed-out data. For cyclic tension-compression loading, the model cannot exclusively characterize the material response since relatively significant effects of the secondary dissipative mechanisms are exhibited in the experimental results. The discrepancy is more apparent for 90° specimens. It is believed that the secondary dissipative mechanisms resulting from the voids of the material's microstructure are more severe for this configuration, since the material is subjected to transverse loading.

Kinematic hardening effects were observed in the analytical predictions of the cyclic response. These effects are caused by the geometrical constraint of the fibers. In the compressive loading-unloading cycle, tensile residual stresses were induced in the matrix phase. Therefore, the subsequent yield stress was translated down in the compression direction. On the other hand, compressive residual stresses were induced in the matrix phase when the material was subjected to tensile loading-unloading cycle. Thus, the subsequent yield stress was translated up in the tension direction.

In the course of micromechanics analysis, accurate data for the in-situ properties of the constituents is essential. For the present investigation, the properties of the graphite fiber and nonlinear

properties of the aluminum matrix were backed out from the test results of the composite. However, due to the inherent defects of the material's microstructure, the accuracy of the backed-out data is questionable.

It has also been illustrated that thermal residual stresses have significant influence on the initial yield stress. Due to the difficulty in determining the residual stresses resulting from the fabrication processes for the present material system, the residual stresses were not included in the analysis. It has been demonstrated that the initial yield stress was not well predicted, particularly for the 90° specimens. The discrepancy between the experiment and analysis initial yielding might be caused by the presence of residual stresses as well as the secondary dissipative mechanisms.

Comparing the microstructure of the material and the geometry of the micromechanics model, it is seen that the particular arrangement of the material in its sandwich form and the resulting voids are not taken into account in the present analysis. The experimental evidence indicates that this is the major cause of the discrepancy between theory and experiment in situations where the secondary mechanisms are operative (i.e. void closure and interfacial slippage). As has been demonstrated in the case of boron/aluminum system [29], the response of the precursor wires may be predicted with good accuracy by the model. Therefore, in order to accurately predict the material behavior for the present Gr/Al, the geometry of the material's microstructure, the sandwich form and the resulting voids, needs to be modeled more realistically.

Chapter 6 Conclusions and Recommendations

The present investigation of the response of unidirectional graphite/aluminum under tension-compression cyclic loading leads to the following conclusions:

1. An experimental methodology and test fixture have been developed to conduct tension-compression cyclic loading tests on unidirectional composites. The experimental results indicate that for the employed specimens with low aspect ratio, the test methodology is applicable for 90° configuration. However, low off-axis configurations should be avoided due to pronounced end-constraint effects and the resulting difficulty of modelling the actual boundary conditions.

2. Poor wire-to-wire interface and inherent voids exist in the material under investigation.

3. The experimental results exhibit the following phenomena:

    - The tensile response is dominated by plasticity, while the compressive response exhibits apparent hysteresis phenomena which cannot be explained exclusively by classical plasticity theory. This evidence strongly indicates that secondary dissipative mechanisms along with plasticity effects are operative in compression.

- The secondary dissipative mechanisms are believed to be caused primarily by the void closure and interfacial slippage between adjacent precursor wires.

- Rounding of the hysteresis loops at the reversal points and slope changes were observed in the compressive response; thus the subsequent yield stress could not be defined.

- The hysteresis phenomenon in compressive response is more significant for the 90° specimens than for the 15° specimens, since for 90° specimens the material is subjected to transverse loading.

- For the 90° specimens, low tensile strength was observed, whereas relatively much higher compressive strength was present. This is believed to be caused by the poor wire-to-wire interface and inherent voids.

- For the 90° specimens, under tension-compression-tension loading cycle, the tensile strength was increased (compared with monotonic tension results) after plastic deformation in compression.

- The initial yield stresses were translated up in the tension direction when the test temperature was increased. This was caused by the change in the state of residual stresses in each phase of the composite due to the temperature change.

4. In correlating the micromechanics analysis and experimental results, good agreement was obtained for monotonic tension, and fairly good agreement was obtained for 15° specimens under tension-compression cyclic loading. However, the correlation was poor for 90° specimens under tension-compression cyclic loading. The influence of the secondary dissipative mechanisms (i.e. void closure and interfacial slippage) is suggested to be the major cause of discrepancy.

The following recommendations for further study result from the present research.

1. The most essential task is the improvement of the manufacture process. The inherent defects and poor wire-to-wire interface have to be eliminated in the fabricating process.

2. Reliable data for the properties of P100-2K graphite fiber should be generated in advance of correlating the micromechanics analysis and experimental results.

3. The actual in-situ properties of the constituents have to be determined more accurately.

4. The geometry of the model needs to be modified to simulate the actual arrangement of the material microstructure for this particular material.

Reference

1. Viswanathan, C. N., Davis, J. G. and Herakovich, C. T., "Tensile and Compressive Behavior of Borsic/Aluminum Composite Laminates", VPI-E-75-12, Virginia Polytechnic Institute & State University, Blacksburg, VA, June 1975.

2. Herakovich, C. T., Davis, J. G. and Viswanathan C. N., "Tensile Compressive Behavior of Borsic/Aluminum", Composite Materials: Testing and Design, (Fourth Conference), ASTM STP 617, American Society of Testing Materials, 1977, pp. 344-357.

3. Pipes, R. B. and Ballintyn, N. J., "Acoustic Emission Response of Metal Matrix Composites", NASA Report No. NADC-76082-30, January 1976.

4. Kennedy, J. M., Herakovich, C. T. and Tenney, D. R., "Influence of Temper Condition on the Nonlinear Stress-Strain Behavior of Boron/Aluminum", VPI-E-77-18, Virginia Polytechnic Institute & State University, Blacksburg, VA, June 1975.

5. Herakovich, C. T., Kennedy, J. M. and Tenney, D. R.,"Effect of Cyclic Loading and Temper Condition on the Tensile Behavior of Boron/Aluminum", Proceedings of the Conference of Environmental Degradation of Engineering Materials, Virginia Tech, Blacksburg, VA, October, 1977.

6. Kennedy, J. M., Tenney, D. R., and Herakovich, C. T., "Tensile and Compressive Stress-Strain Response of Heat Treated Boron/Aluminum", Second International Conference on Composite Materials, Toronto, Canada, April 1978.

7. Becker, W., "Mechanical Response of Unidirectional Boron/Aluminum under Combined Loading", Master Thesis, Department of Engineering Science and Mechanics, Virginia Polytechnic Institute & State University, Blacksburg, VA, June, 1987.

8. Pepper, R. T. and Penty, R. A., "Mechanical Properties of Aluminum-Graphite Composites Prepared by Liquid Phase Hot Pressing," *Journal of Composite Materials,* Vol. 8, 1974, pp. 29-37.

9. Hoover, W. R., "Graphite/Aluminum: An Evaluation of State-of-the-Art Material," *Journal of Composite Materials,* Vol. 11, 1977, pp. 17-29.

10. Pfeifer, W. H. and Kinna, M. A., "Characterization of the Mechanical Property Behavior of Selected Graphite Fiber Reinforced Aluminum Alloys," Proceedings of the Second International Conference on Composite Materials (ICCM-2), Toronto, Canada, April 16-20, 1978, pp. 153-172.

11. Tribendis, J. J., Koczak, M. J. and Gracia, R., "The Effect of Fiber Orientation and Thermal Treatment on the Mechanical Properties of Graphite-Aluminum Composites," *Powder Metallurgy International,* Vol. 13, 1981, pp. 88-92.

12. Fujita, T., Pindera, M. J., and Herakovich, C. T., "Temperature-Dependent Tensile and Shear Response of Graphite/Aluminum", VPI-E-87-8, Virginia Polytech Institute & State University, Blacksburg, VA, May, 1987.

13. Starbuck, J. M.,Gurdal Z. and Herakovich C. T., "Thermomechanical Response of Graphite-Aluminum in Compression", Proceedings of the Fourth Annual Review, CCMS, Virginia Polytechnic Institute and State University, Blacksburg, VA, May 1987.

14. Hill, R., "Theory of Mechanical Properties of Fiber-Strengthened Materials: II. Inelastic Behavier", *J. Mech. Phys. Solids,* 1964, Vol. 12, pp. 213-218.

15. Hill, R., "Theory of Mechanical Properties of Fiber-Strengthened Materials : III. Self-Consistent Model", *J. Mech. Phys. Solids,* 1965, Vol. 13, pp. 189-198.

16. Mulhern, J. F., Rogers, T. G. and Spencer, A. J. M., "Cyclic Extension of an Elastic Fiber with an Elastic-Plastic Coating", *J. Inst. Maths. Applics.,* 1967, Vol. 3, pp. 21-40.

17. Adams, D. F., "Inelastic Analysis of a Unidirectional Composite Subjected to Transverse Normal Loading", *J. Composite materials,* 1970, Vol. 4, pp. 310-328.

18. Lin, T. H. Salinas, D. And Ito, Y. M., "Initial Yield Surface of a Unidirectionally Reinforced Composite", *J. Applied Mechanics,* 1972, Vol. 39, pp. 321-326.

19. Lin, T. H. Salinas, D. and Ito, Y. M., "Elastic-Plastic Analysis of Unidirectional Composites", *J. Composite materials,* 1972, Vol. 6, pp. 48-60.

20. Dvorak, G. J., Rao, M. S. M. and Tarn, J. Q., "Yielding in Unidirectional Composites under External Loads and Temperature Changes", *J. Composite Materials,* 1973, Vol. 7, pp. 195-214.

21. Dvorak, G. J., Rao, M. S. M. and Tarn, J. Q., "Generalized Initial Yield Surfaces for Unidirectional Composites", J. Applied Mechanics, 1974, Vol. 41, pp. 249-253.

22. Foye, R. L., "Theoretical Post-Yielding Behavior of Composite Laminates. I. Inelastic Micromechanics", *J. Composite Materials,* 1973, Vol. 7, pp. 178-193.

23. Dvorak, G. J. and Rao M. S. M., "Axisymmetric Plasticity Theory of Fibrous Composites", *Int. J. Engr. Sci.,* 1976, Vol. 14, pp. 361-373

24. Aboudi, J., "A Continuum Theory for Fiber Reinforced Elastic-Viscoplastic Composites", *Int. J. Engr. Sci.,* 1982, Vol. 20, pp. 605-621.

25. Aboudi, J., "Effective Behavior of Inelastic Fiber-Reinforced Composites", *Int. J. Engr. Sci.,* 1984, Vol. 22, pp. 439-449.

26. Aboudi, J., "The Effective Thermomechanical Behavior of Inelatic Fiber-Reinforced Materials", *Int. J. Engr. Sci.,* 1985, Vol. 23, pp. 773-787.

27. Aboudi, J., "Elastoplasticity Theory for Composite Materials", *Solid Mechanics Archives,* 1986, Vol. 11, pp. 141-183.

28. Aboudi, J., "Closed Form Constitutive Equations for Metal Matrix Composites", *Int. J. Engr. Sci.,* (to appear)

29. Pindera, M. J., Aboudi, J. and Herakovich, C. T., "Nonlinear Response of Boron/Aluminum under Combined Loading", Proceedings of the IUTAM/ICM Symposium on Yielding, Damage, and Failure of Anisotropic Solids, Grenoble, France, August, 1987.

30. Pindera, M. J., "Micromechanical Aspects of Yielding and Failure Criteria of Composites", Failure Criteria of Structured Media, J. P. Boehler, ed. A. A. Balkema (in press).

31. Pindera, M. J. and Herakovich, C. T., "Shear Characterization of Unidirectional Composites with the Off-Axis Tension Test', *Experimental Mechanics,* 1986, Vol. 26, pp. 103-112.

32. Gurdal, Z. and Starbuck, J. M., "Compressive Characterization of Unidirectional Composite Material", Proceeding of the International Conference on Analytical and Testing Methodologies for Design with Advanced Material, Montreal, Canada, August 1987.

33. Hidde, J. S., Beuth, J., and Herakovich, C. T., "MATPAC: A PC Based software Package for Materials Testing", Composite Mechanics Group, Department of Engineering Science and Mechanics, Virginia Polytechnic Institute and State University, September, 1987.

34. Gregory, M. A., Choksi, G. N. and Herakovich, C. T., "ANFRAC- A Singular Finite Element Program for Fracture Analysis of Unidirectional Composites", CCMS-87-05, VPI-E-87-1, Virginia Polytechnic Institute and State University, February 1987.

35. Pagano, N. J., Halpin, J. C., "Influence of the End Constraint in the Testing of Anisotropic Bodies", *J. Composite materials,* 1968, Vol. 2, PP. 18-31.

36. Bonder, S. R. and Partom, Y., "Constitutive Equations for Elastic-Viscoplastic Strain-Hardening Materials", J. Applied Mechanics, 1975, Vol. 42, PP. 385-389.

37. "Structural Alloys Handbook", Department of Defence, Metals and Ceramics Information Center, Battelle's Columbus Division, 1986, Edition, Vol. 3.

38. Thornel Graphite Fiber P-100S 2K, Techanical Information, Amoco Performance Product, Inc., 1986.

39. Pindera, M. J. and Herakovich C. T., "Endochronic Theory for Transverse Isotropic Fibrous Composites", VPI-E-81-27, Virginia Polytechnic Institute and State University, Blacksburg, VA, October, 1981.

40. Choi, I. and Horgan, C. O., "Saint-Venant's Principle and End Effects in Anisotropic Elasticity", *J. Applied Mechanics* (Trans. ASME), 1977, Vol. 44, PP. 424-430.

41. Micro-Measurements, "Strain Gage Installations with M-Bond 200 Adhesive", Instruction Bulletin B-127-8, Micro-Measurements Division, Measurements Group, Inc..

42. Micro-Measurements, "Strain Gage Installations with M-Bond 43-B, 600 and 610 Adhesive Systems", Instruction Bulletin B-130-10, Micro-Measurement Division, Measurements Group, Inc..

43. Micro-Measurements, "Temperature-Induced Apparent Strain and Gage Factor Variation in Strain Gages", TN-504, Micro-Measurements Division, Measurements Group, Inc..

44. Jones, R. M., "Mechanics of Composite Materials", McGRAW-HILL, 1975.

45. Azzi, V. D. and Tsai, S. W., "Anisotropic Strength of Composites", *Experimental Mechanics,* 1965, Vol. 5, pp. 283-288.

46. Kelly, A. and Davies, G. J., "The Principles of the Fiber Reinforcement of Metals", *Metallurgical Reviews,* 1965, Vol. 10, pp. 1-77.

Appendix A. Individual Test Results

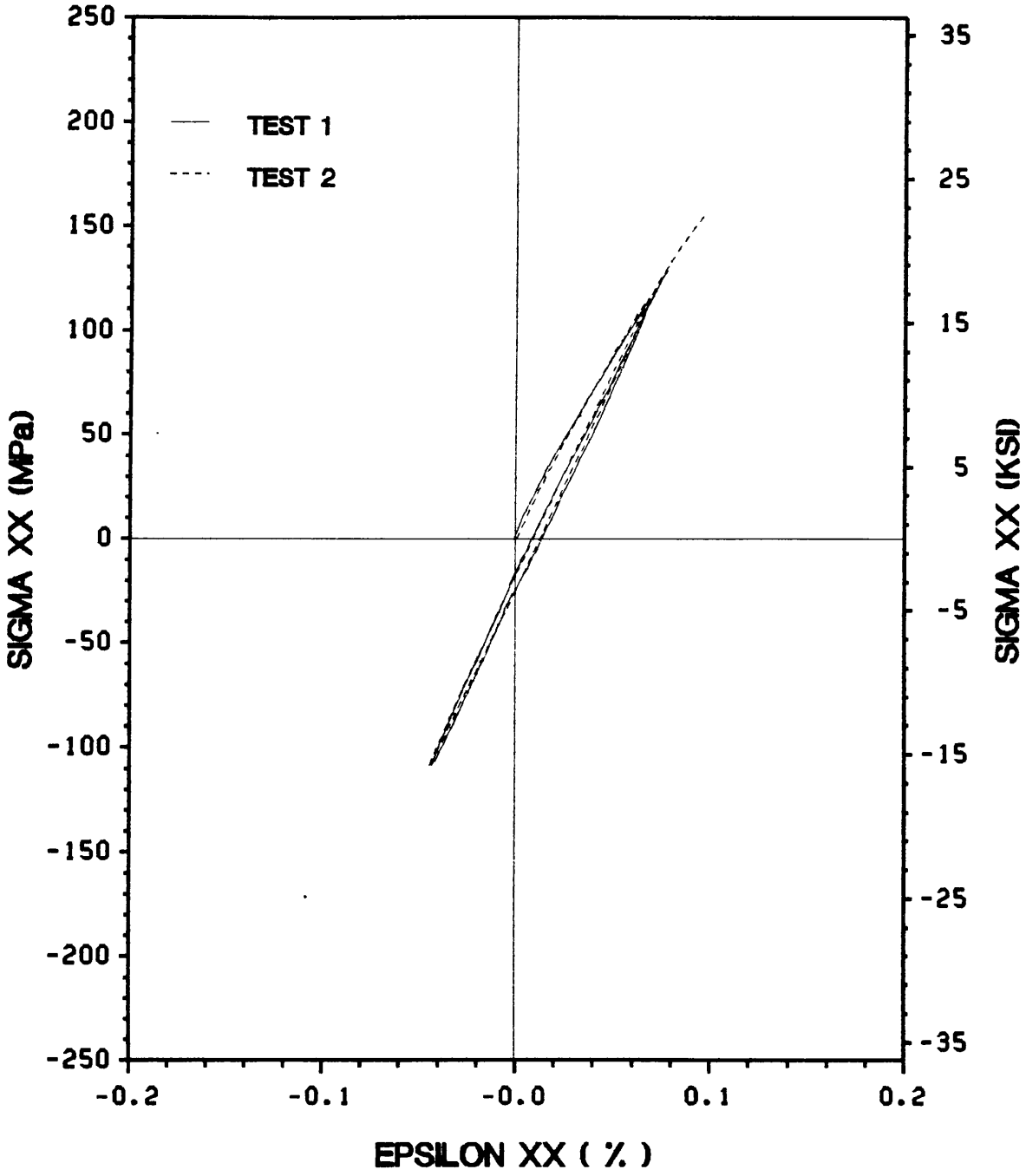

Figure A. 1. Longitudinal response of 15° specimens under tension-compression-tension cyclic loading at -150°F

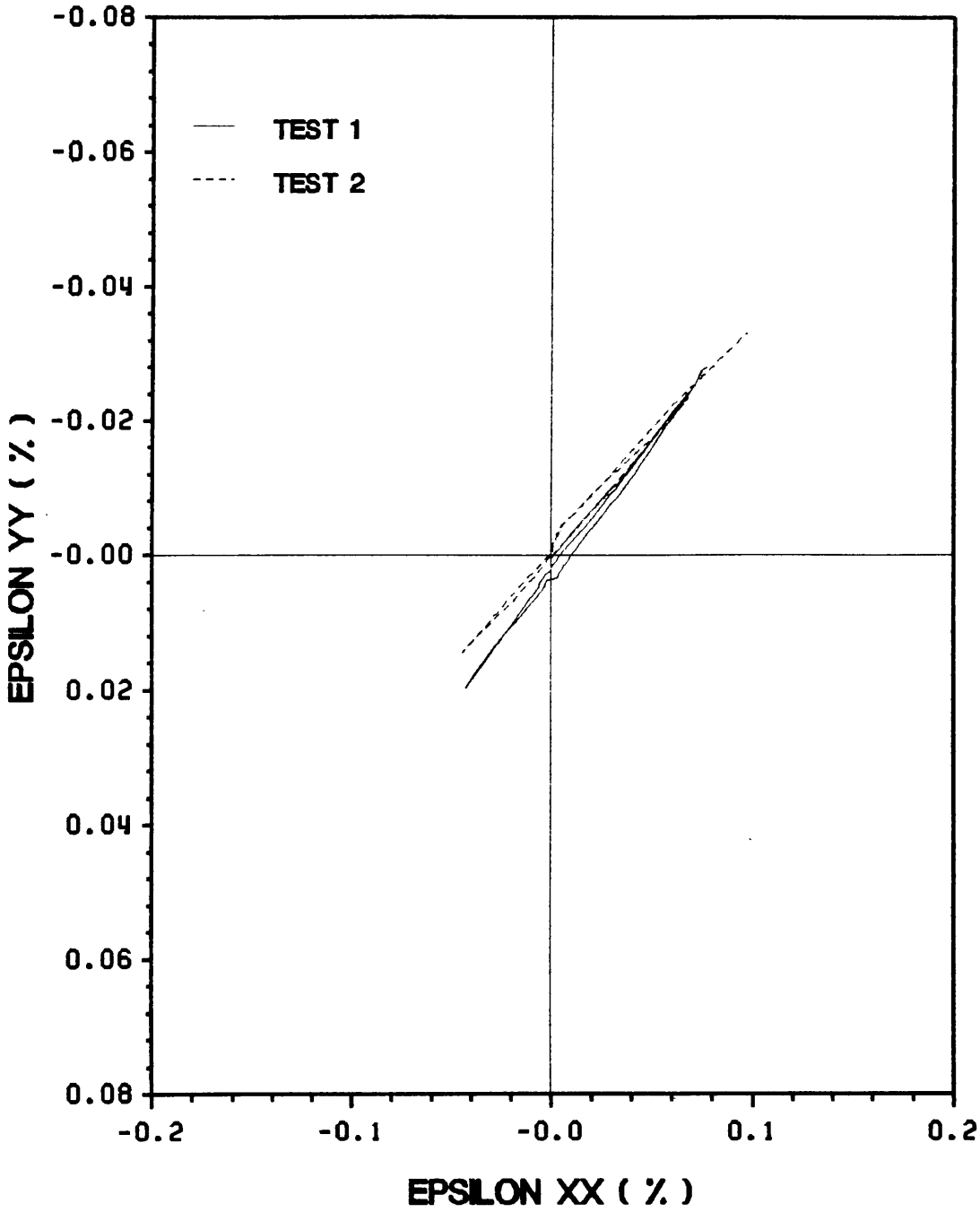

Figure A. 2. Poisson's response of 15° specimens under tension-compression-tension cyclic loading at -150°F

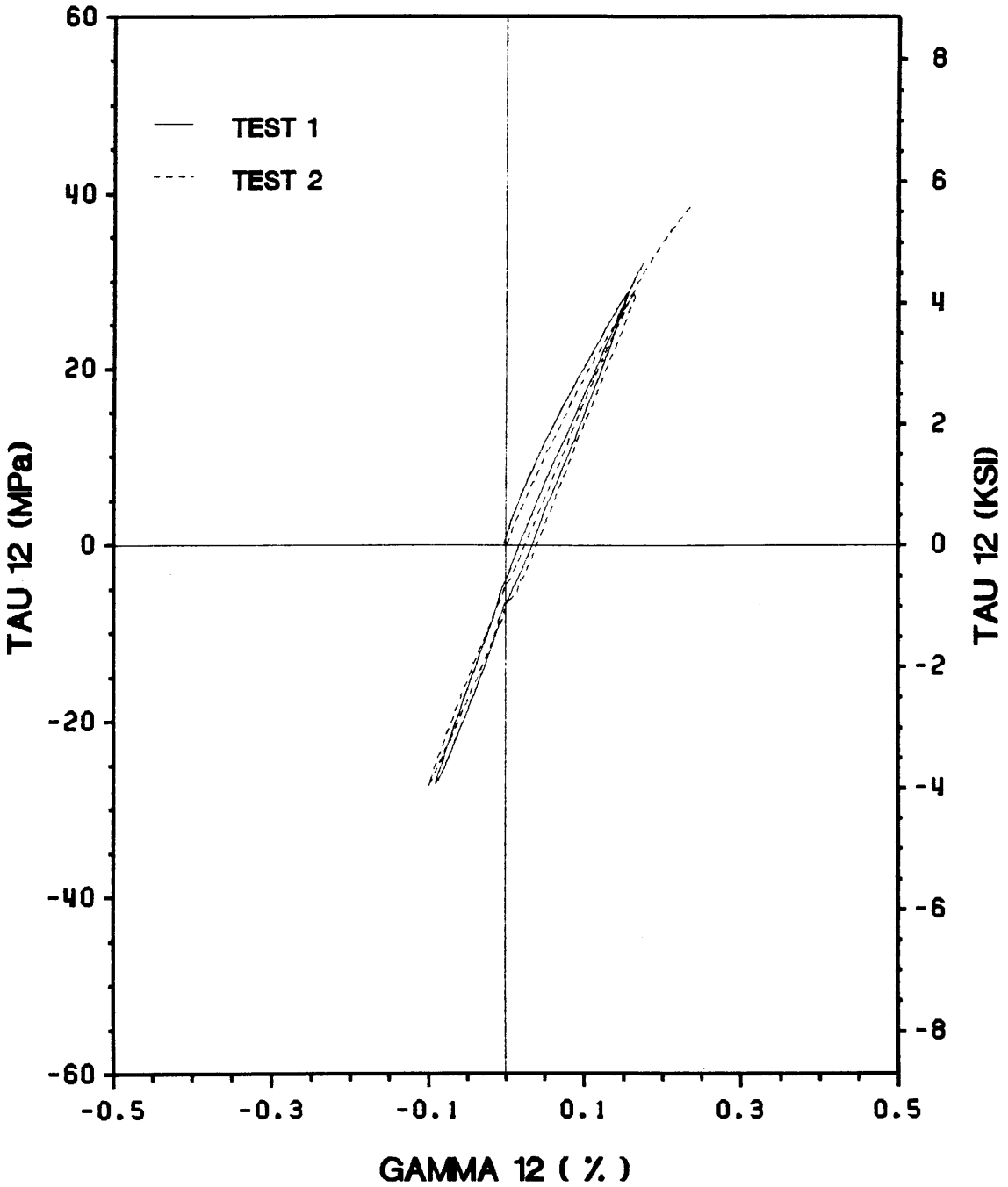

Figure A. 3. Shear response of 15° specimens under tension-compression-tension cyclic loading at -150°F

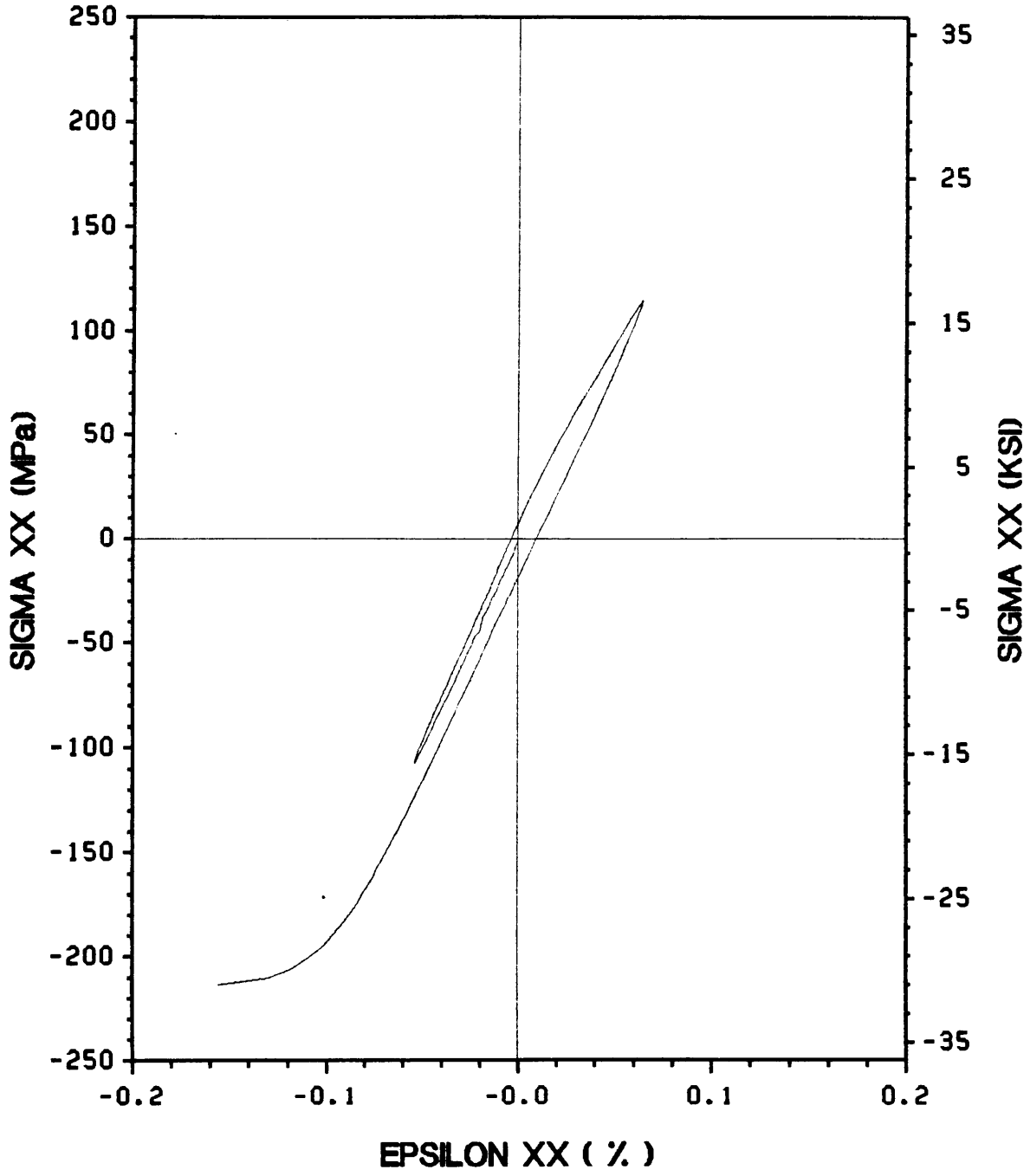

Figure A. 4. Longitudinal response of 15° specimen under compression-tension-compression cyclic loading at -150°F

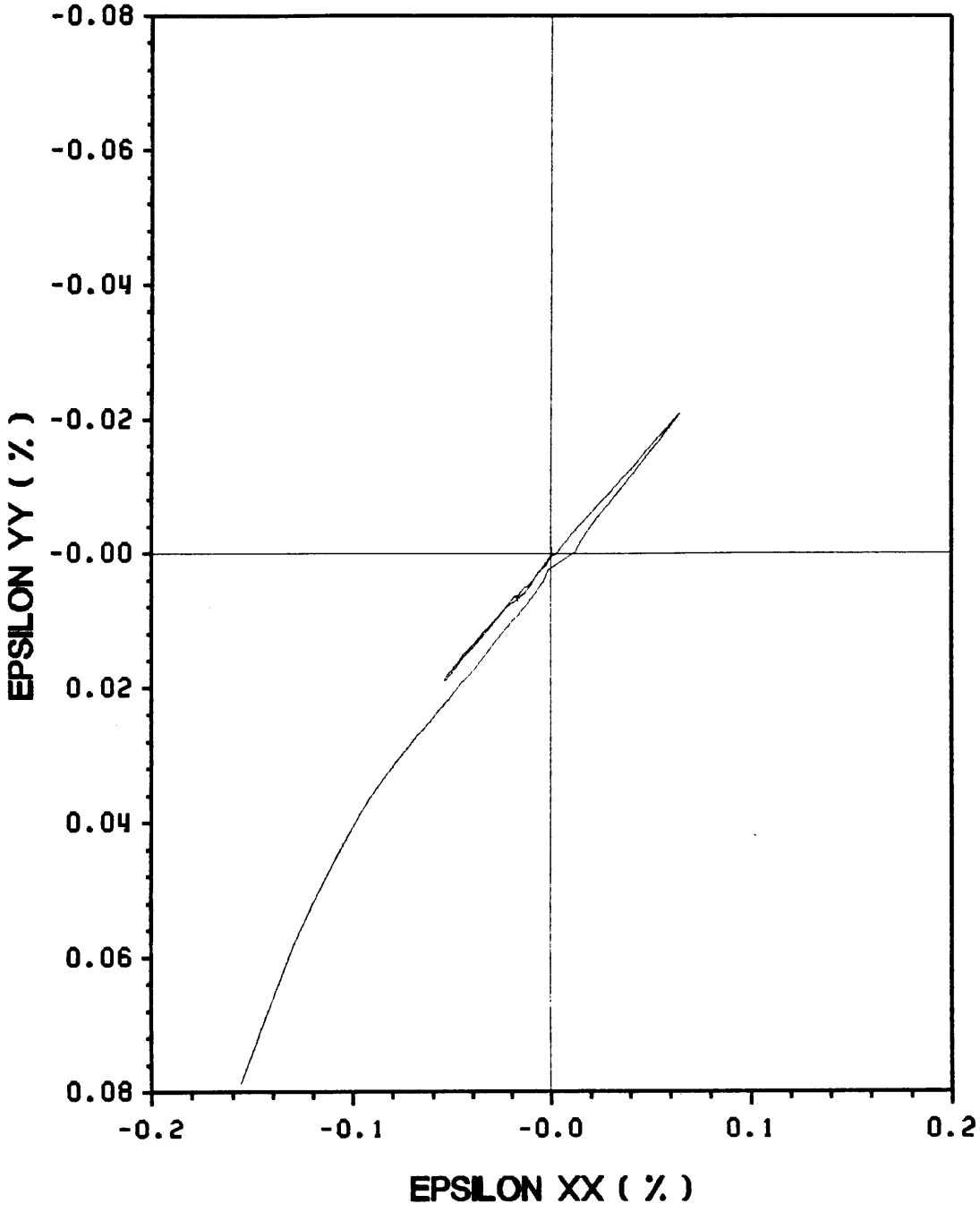

Figure A. 5. Poisson's response of 15° specimen under compression-tension-compression cyclic loading at -150°F

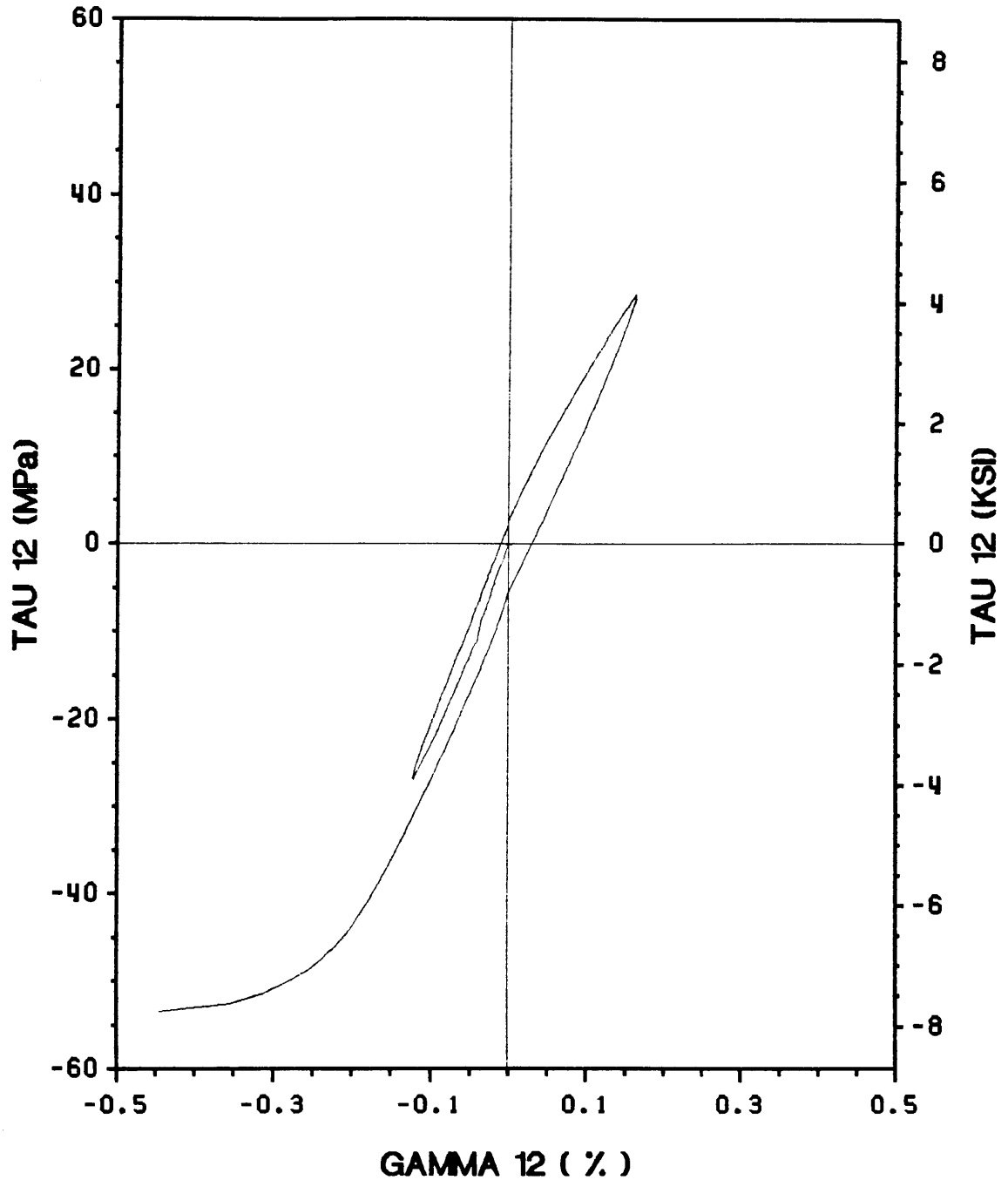

Figure A. 6. Shear response of 15° specimen under compression-tension-compression cyclic loading at -150°F

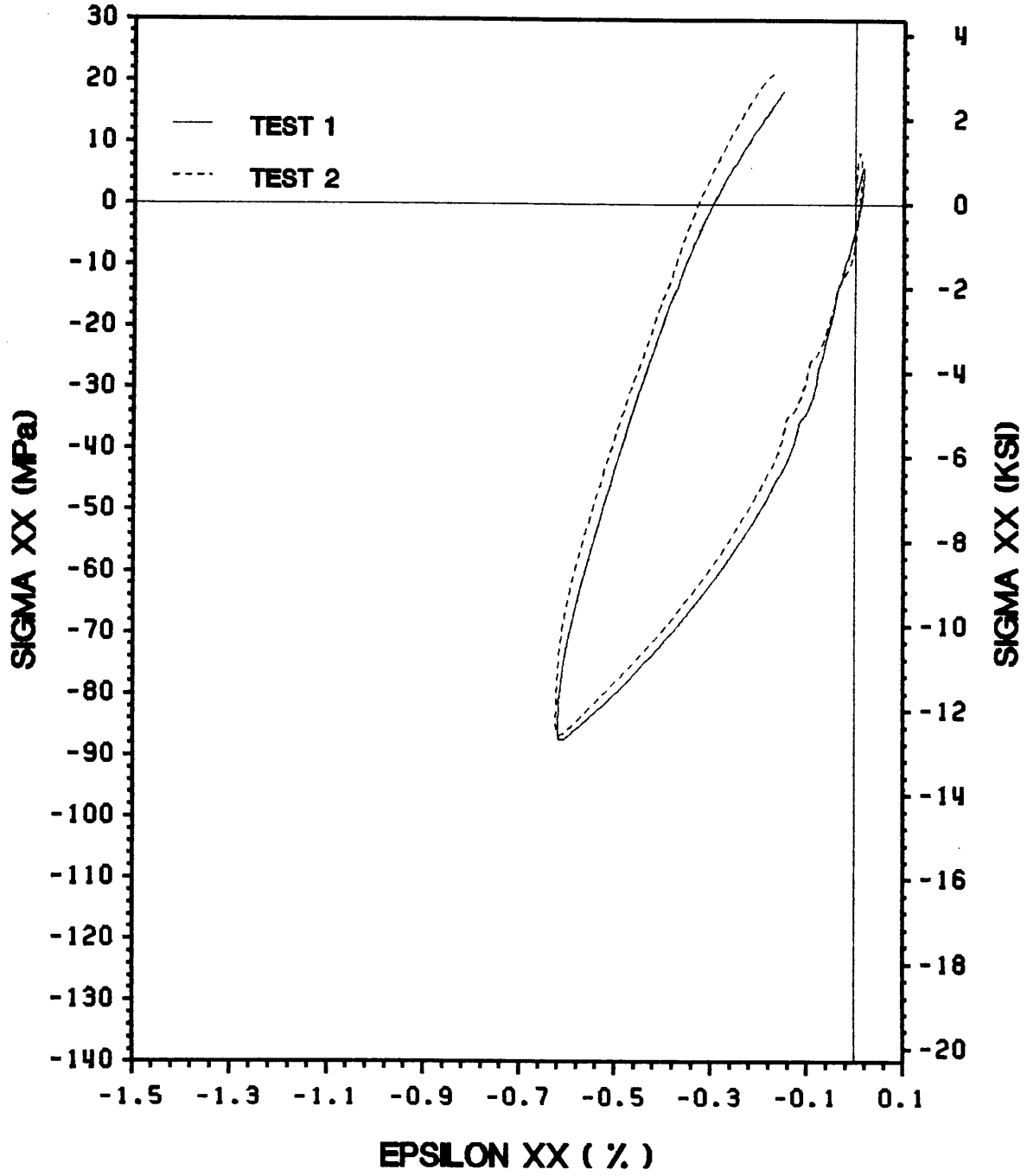

Figure A. 7. Longitudinal response of 90° specimens under tension-compression-tension cyclic loading at -150°F

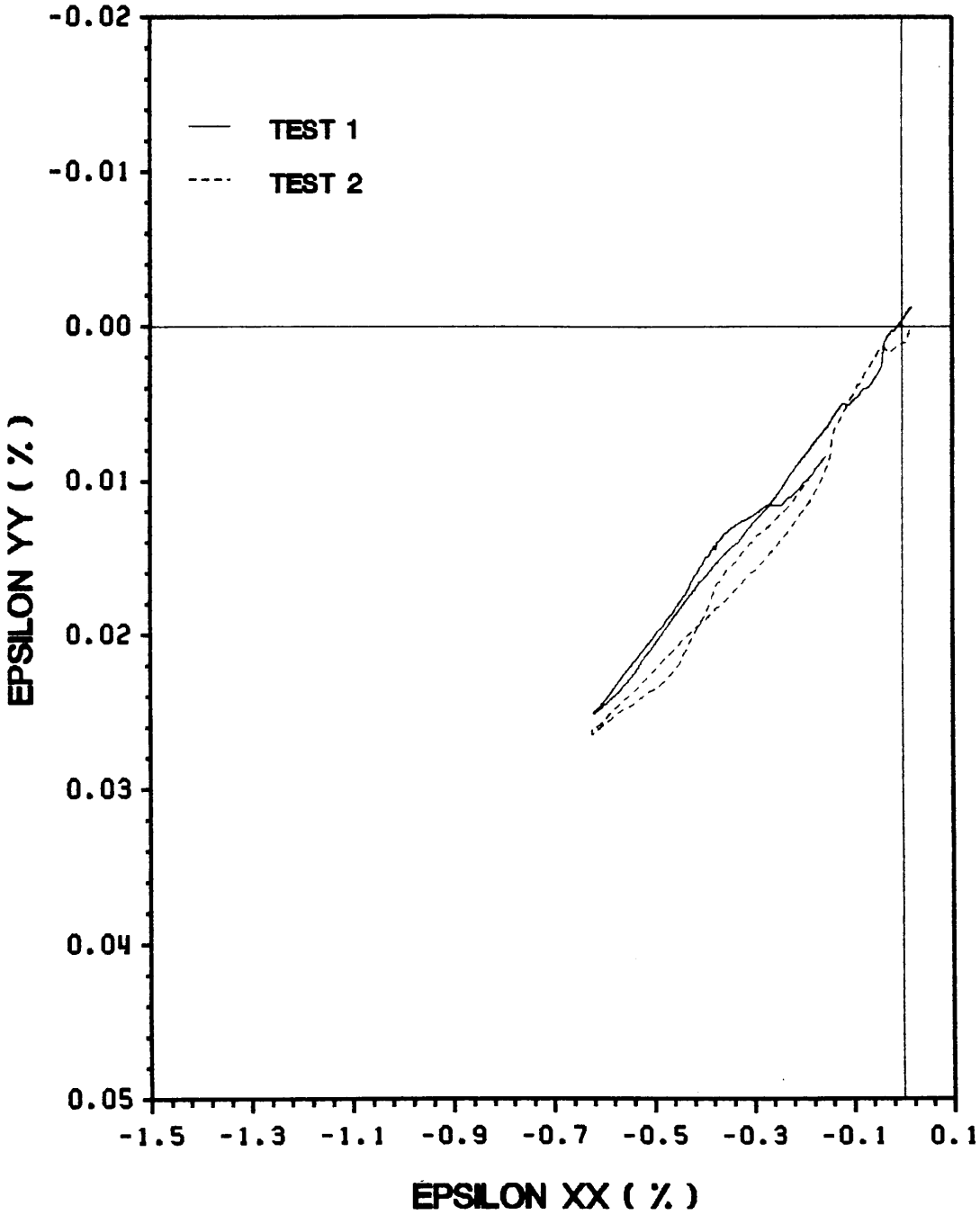

Figure A. 8. Poisson's response of 90° specimens under tension-compression-tension cyclic loading at -150°F

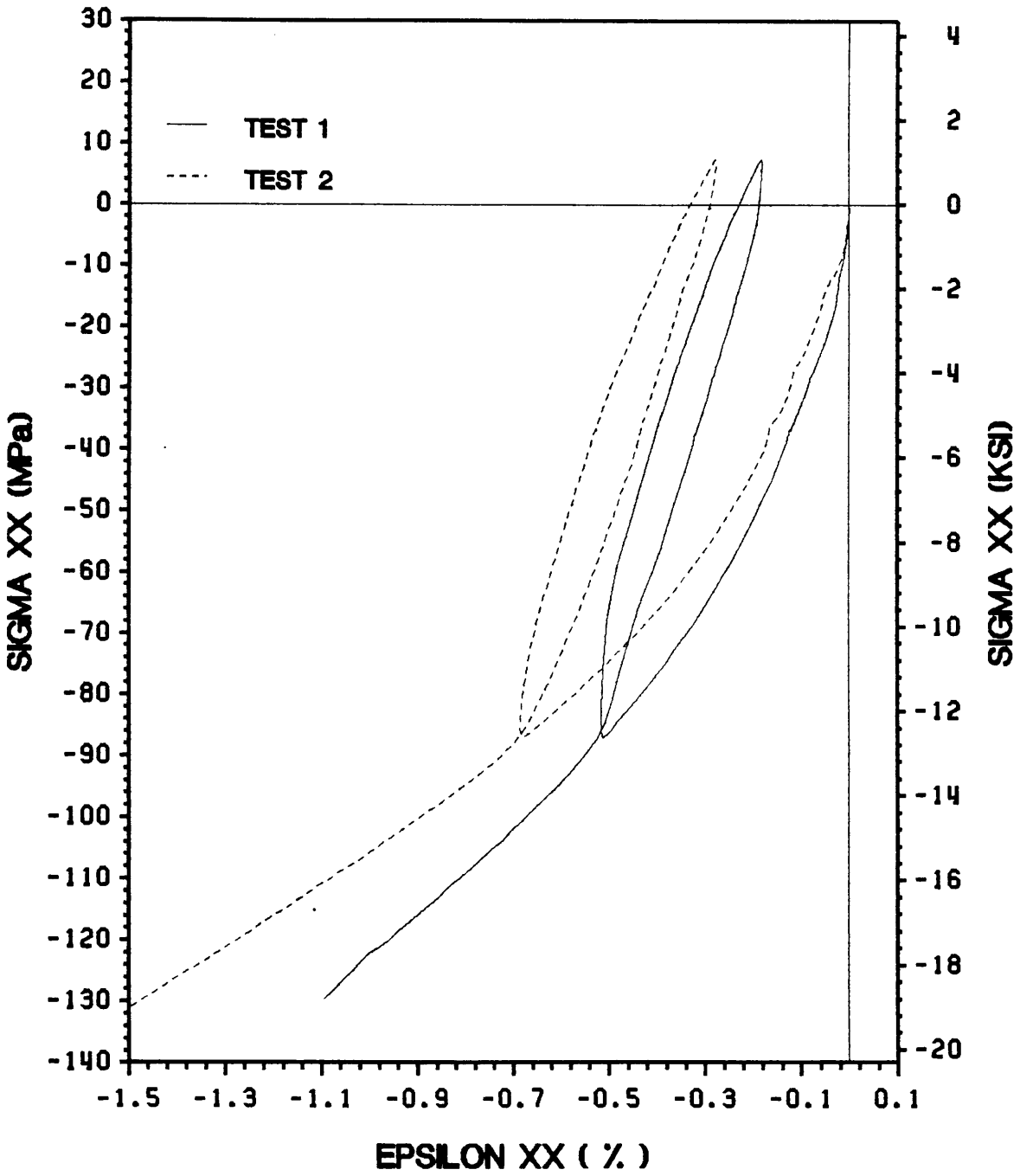

Figure A. 9. Longitudinal response of 90° specimens under compression-tension-compression cyclic loading at -150°F

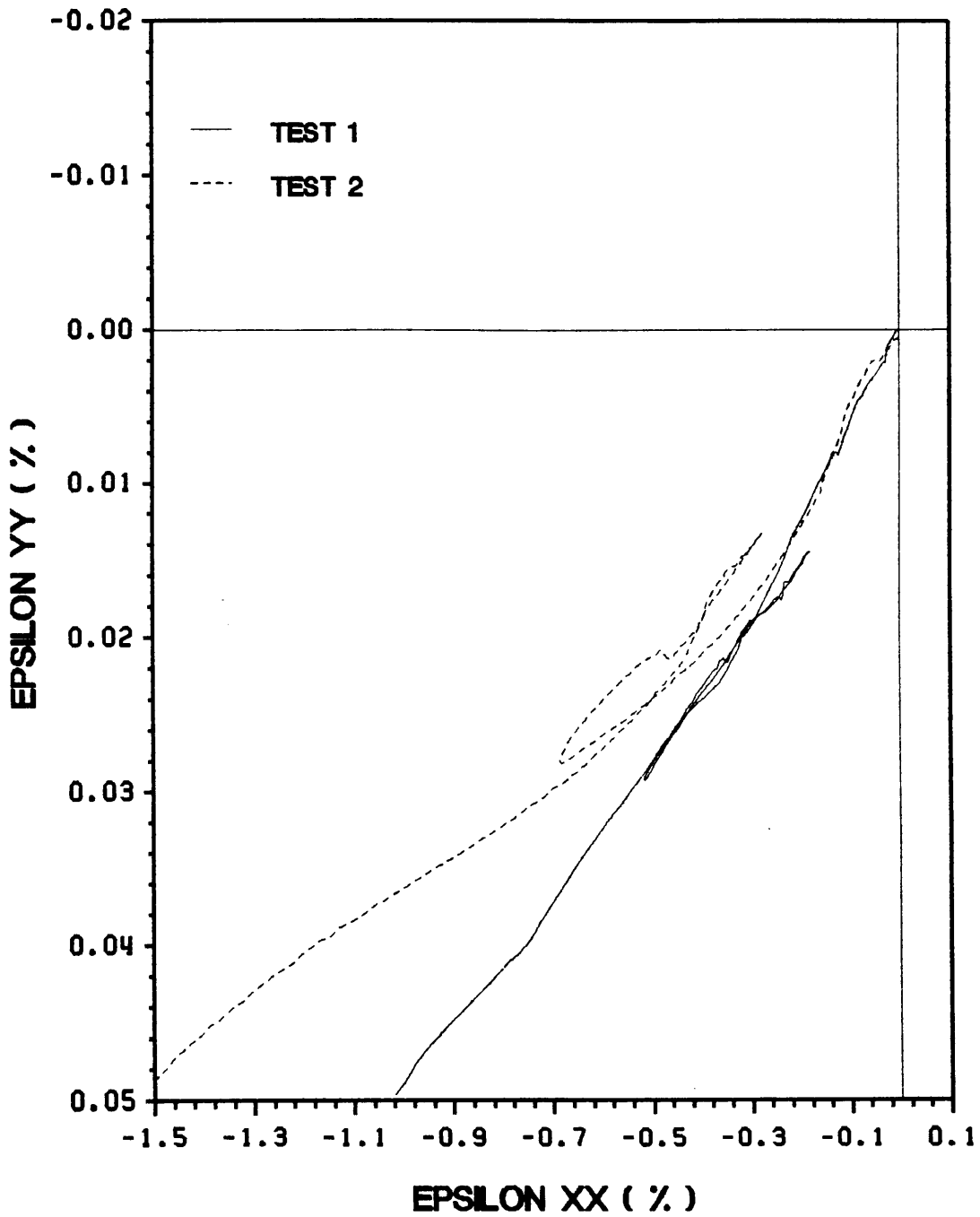

Figure A. 10. Poisson's response of 90° specimens under compression-tension-compression cyclic loading at -150°F

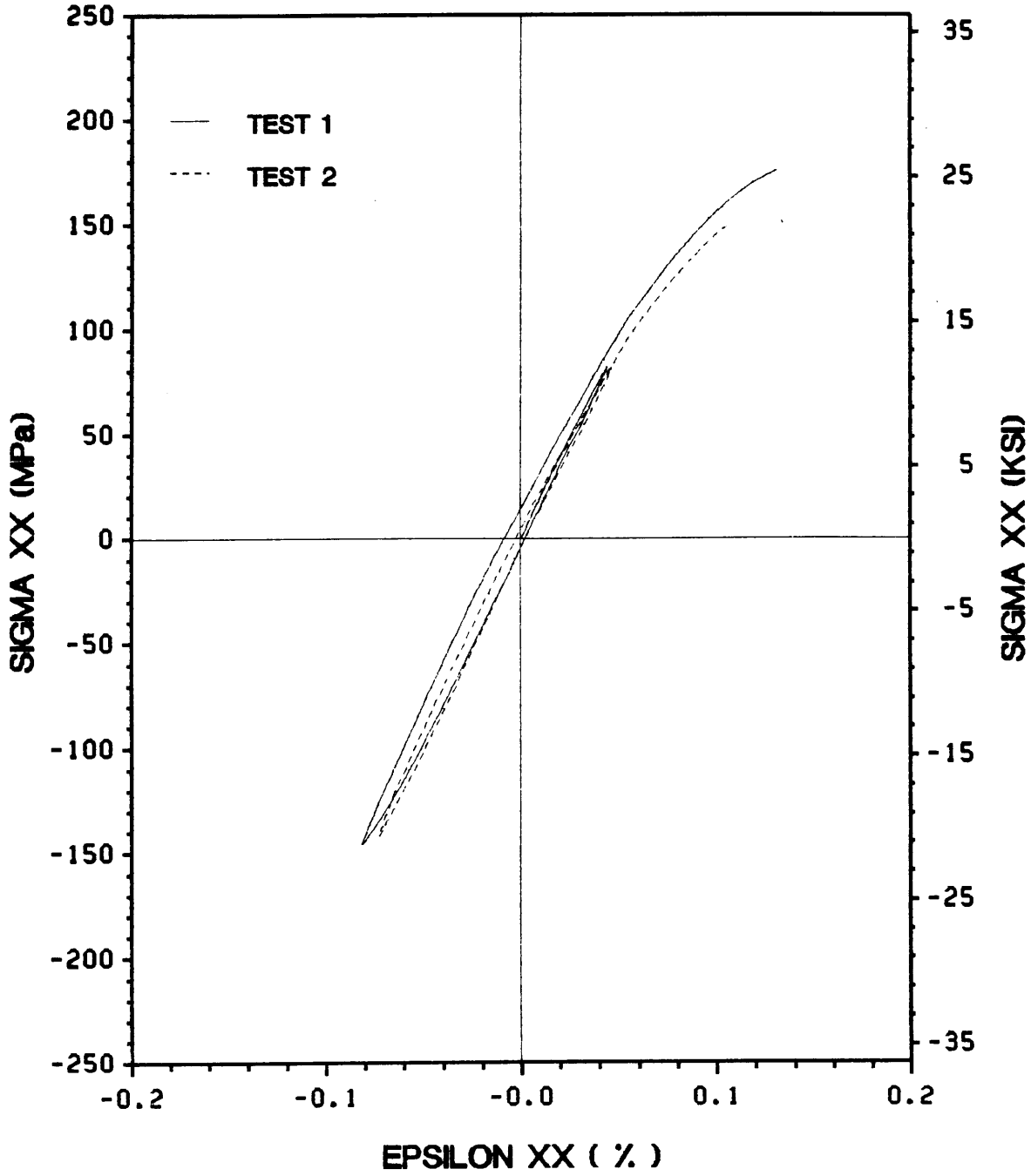

Figure A. 11. Longitudinal response of 15° specimens under tension-compression-tension cyclic loading at room temperature

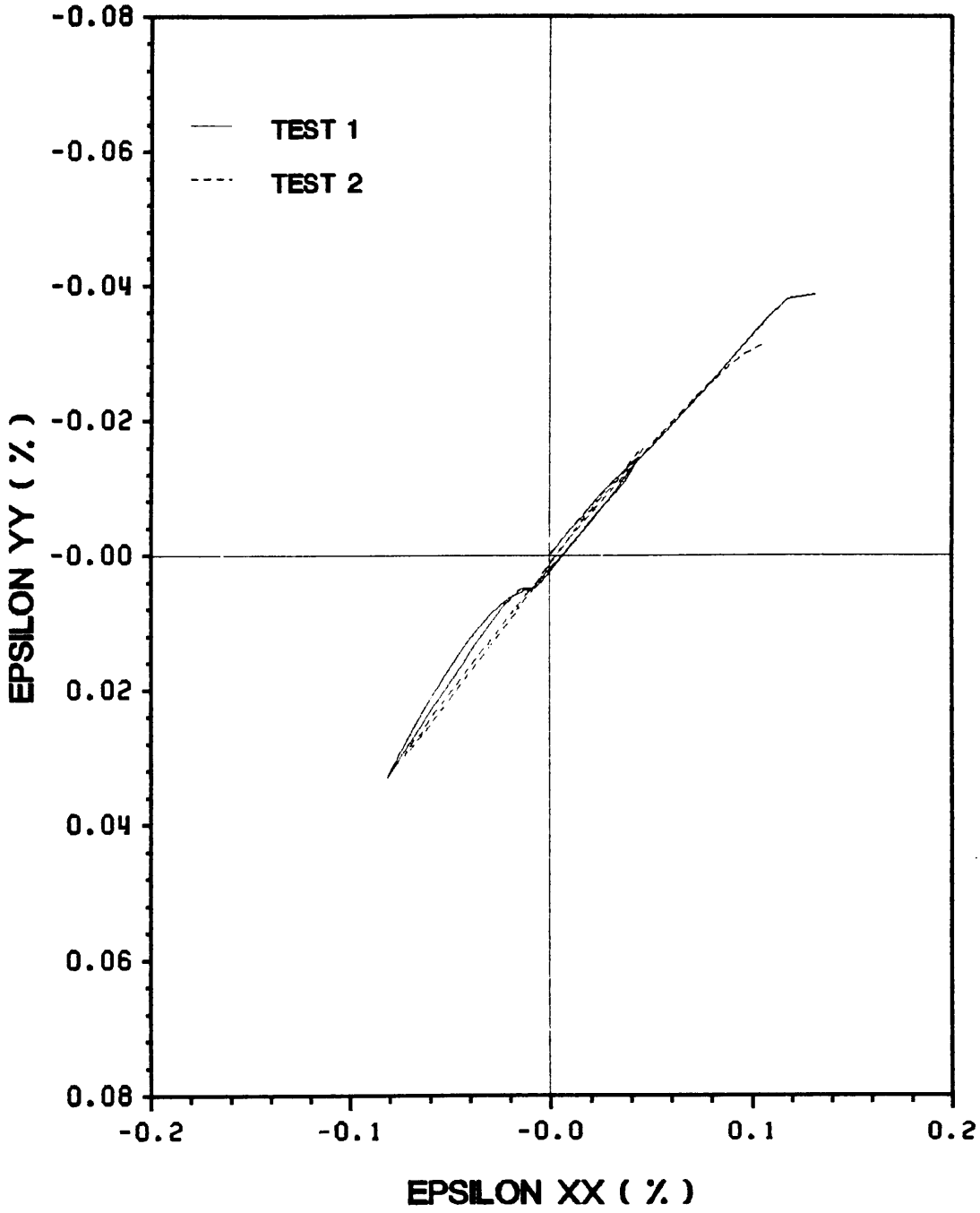

Figure A. 12. Poisson's response of 15° specimens under tension-compression-tension cyclic loading at room temperature

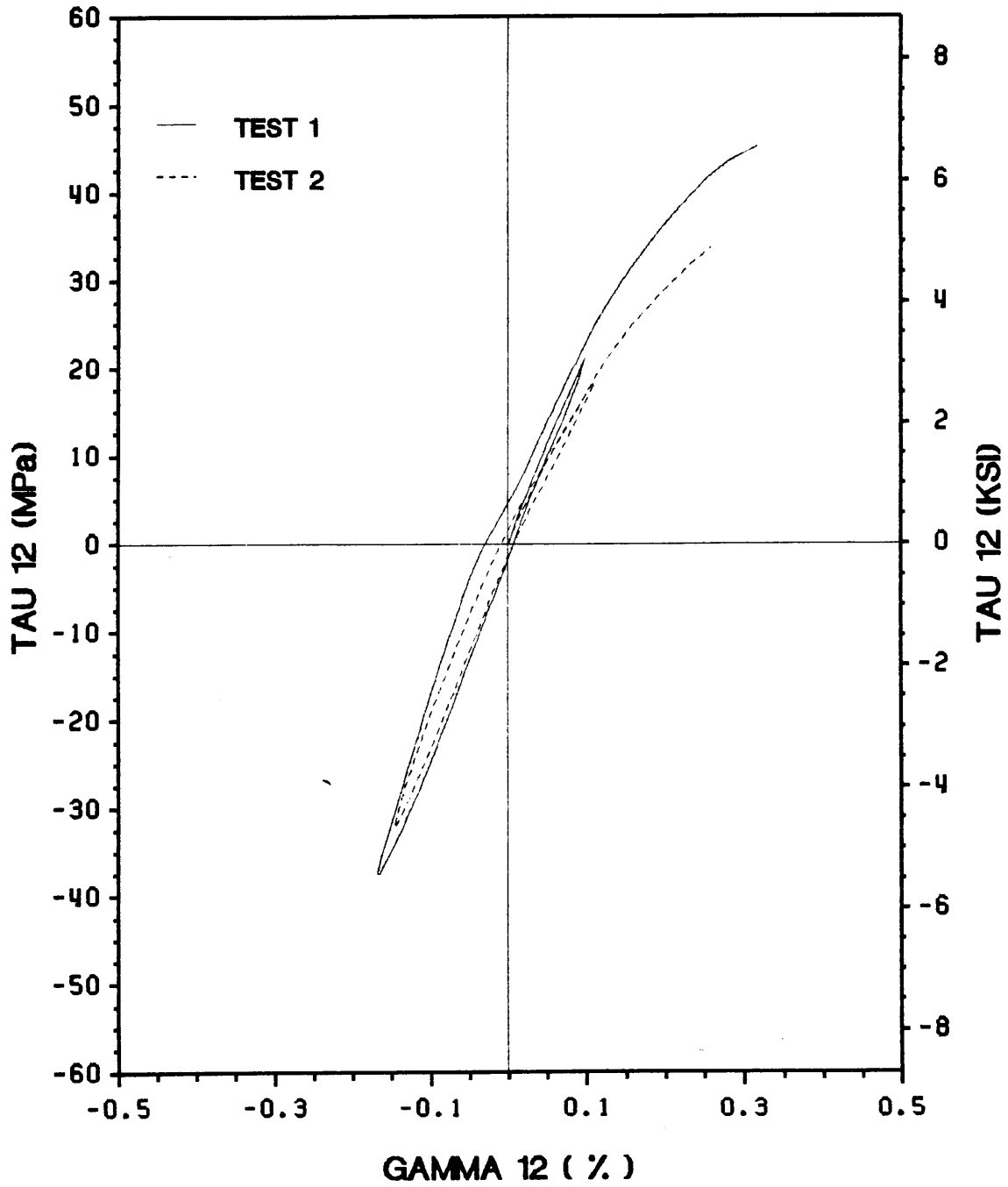

Figure A. 13. Shear response of 15° specimens under tension-compression-tension cyclic loading at room temperature

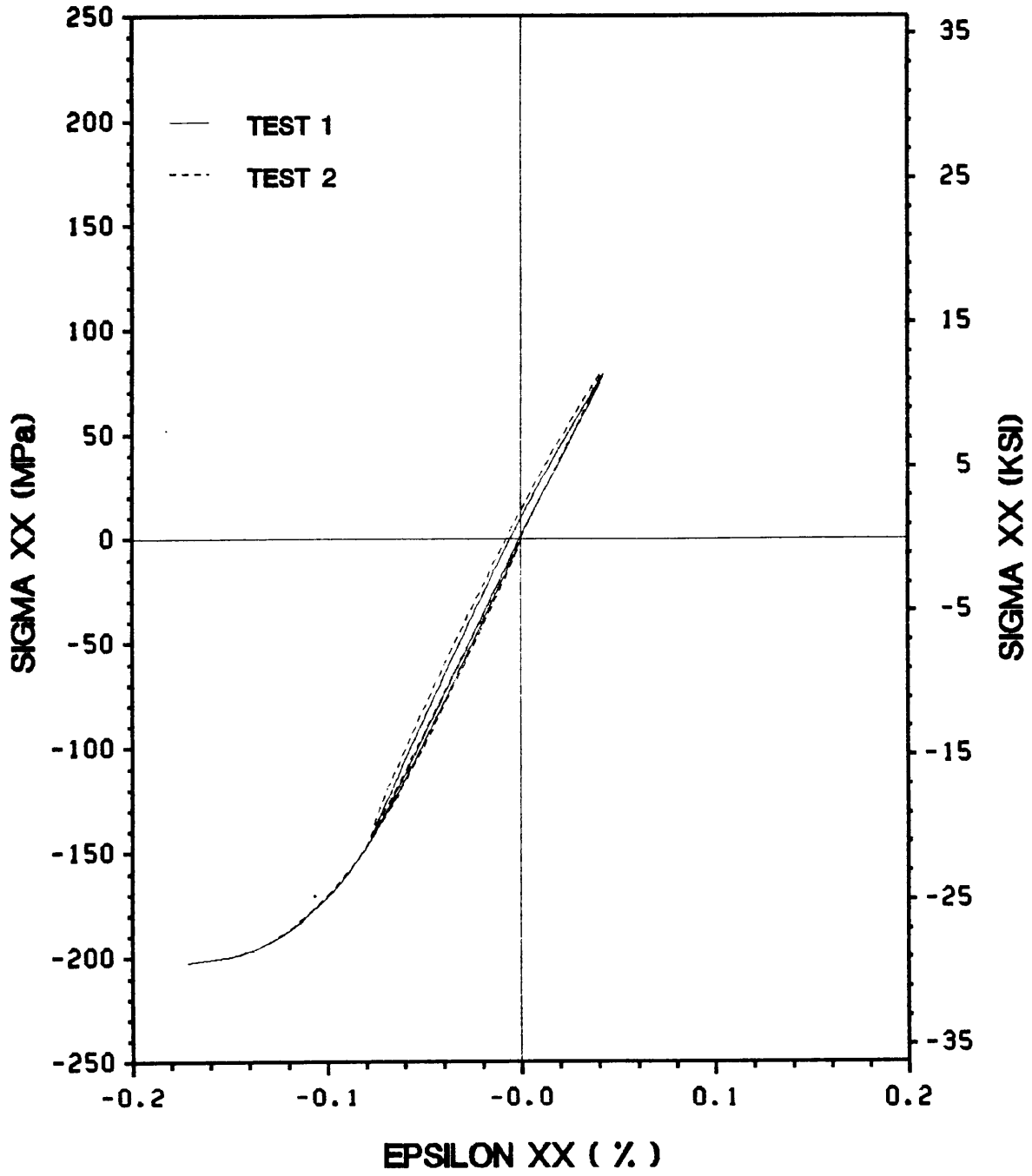

Figure A. 14. Longitudinal response of 15° specimens under compression-tension-compression cyclic loading at room temperature

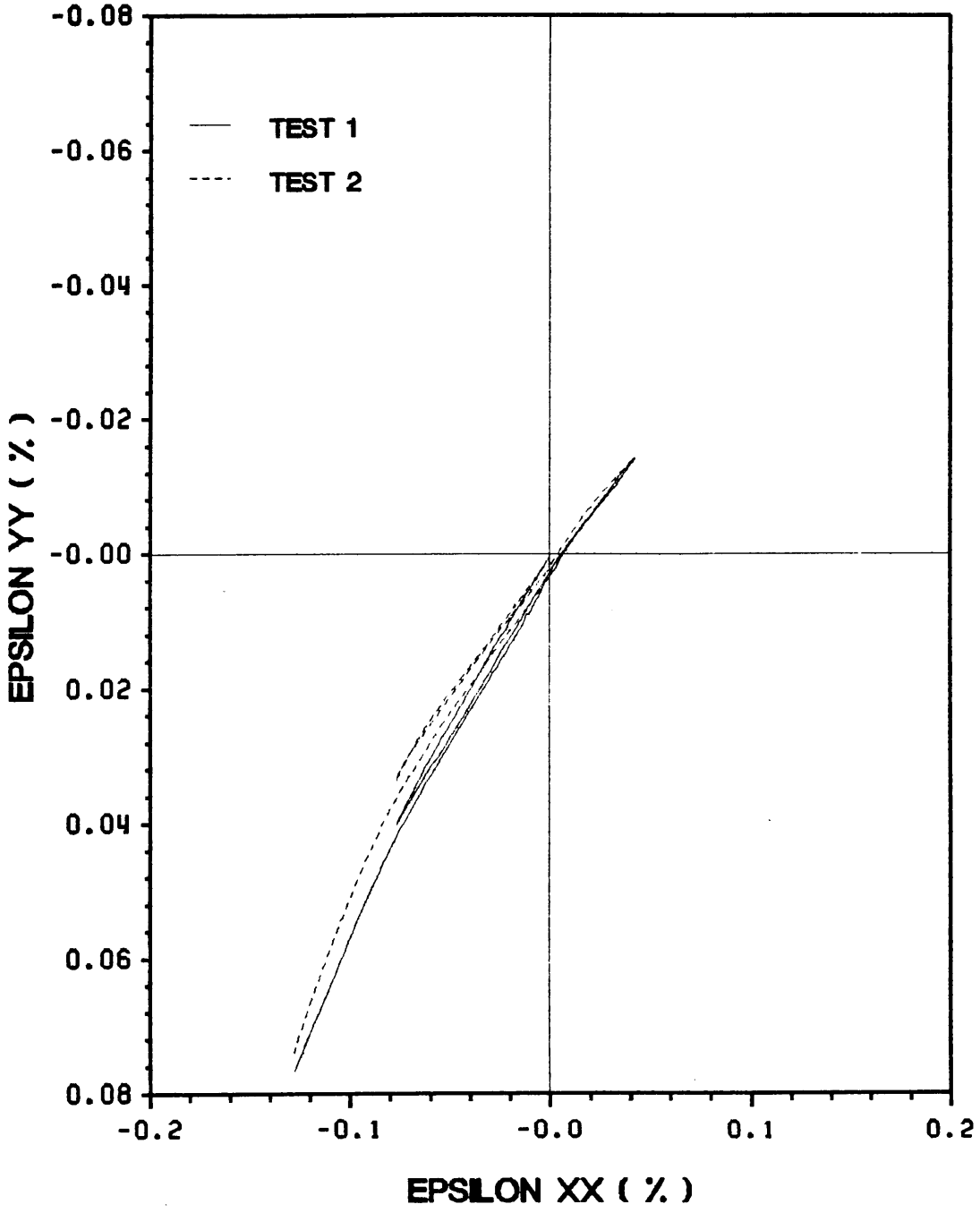

Figure A. 15. Poisson's response of 15° specimens under compression-tension-compression cyclic loading at room temperature

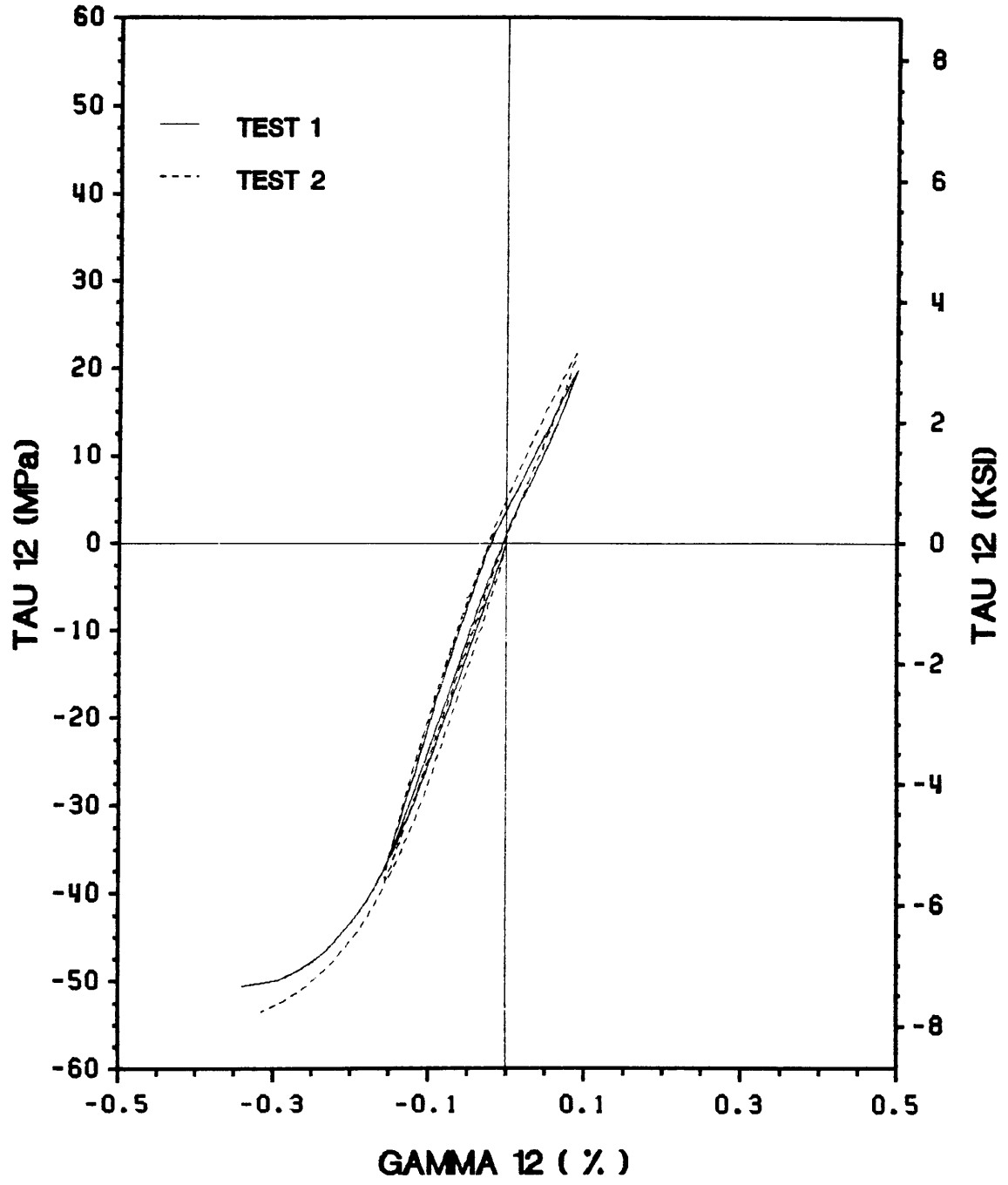

Figure A. 16. Shear response of 15° specimens under compression-tension-compression cyclic loading at room temperature

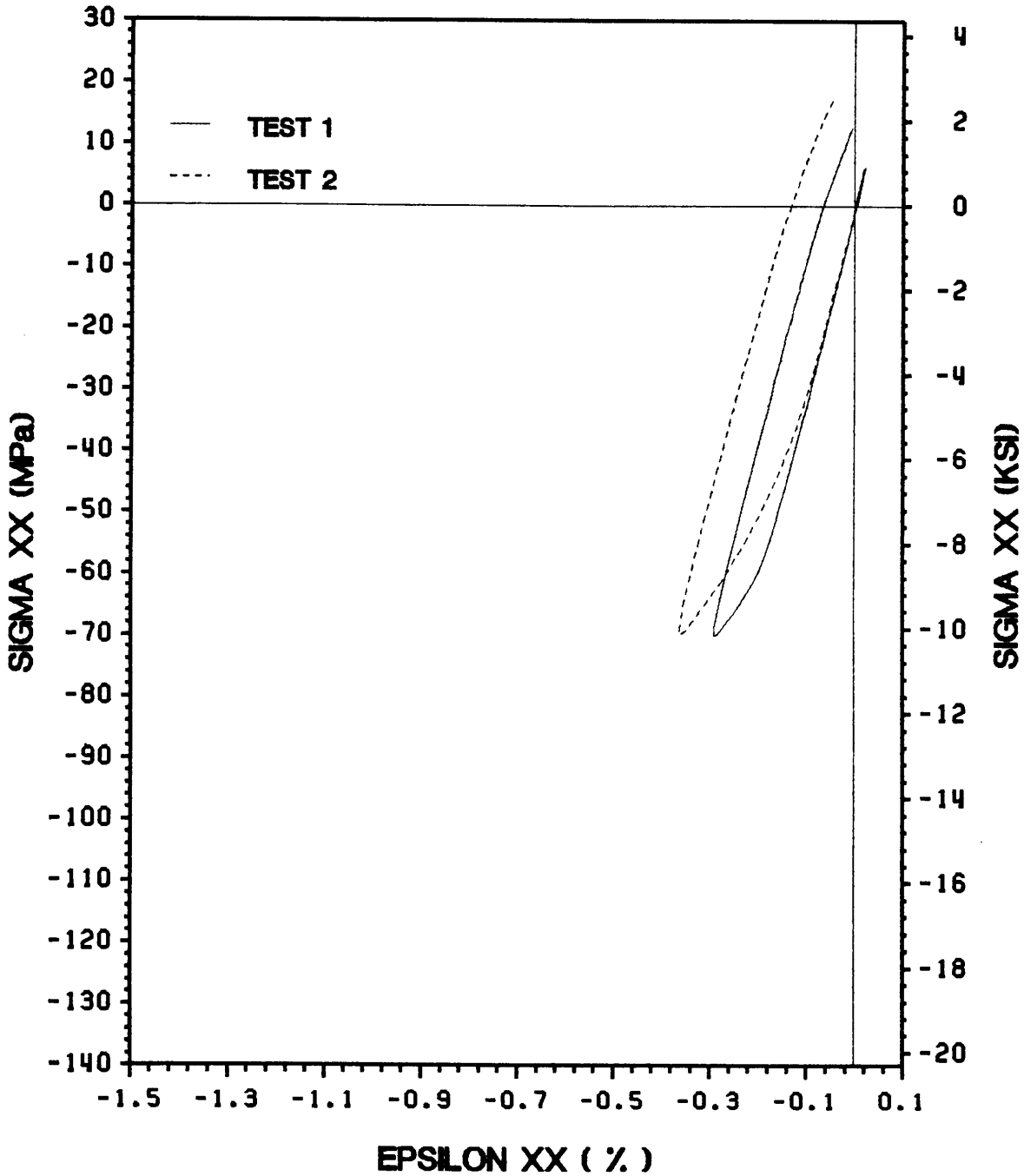

Figure A. 17. Longitudinal response of 90° specimens under tension-compression-tension cyclic loading at room temperature

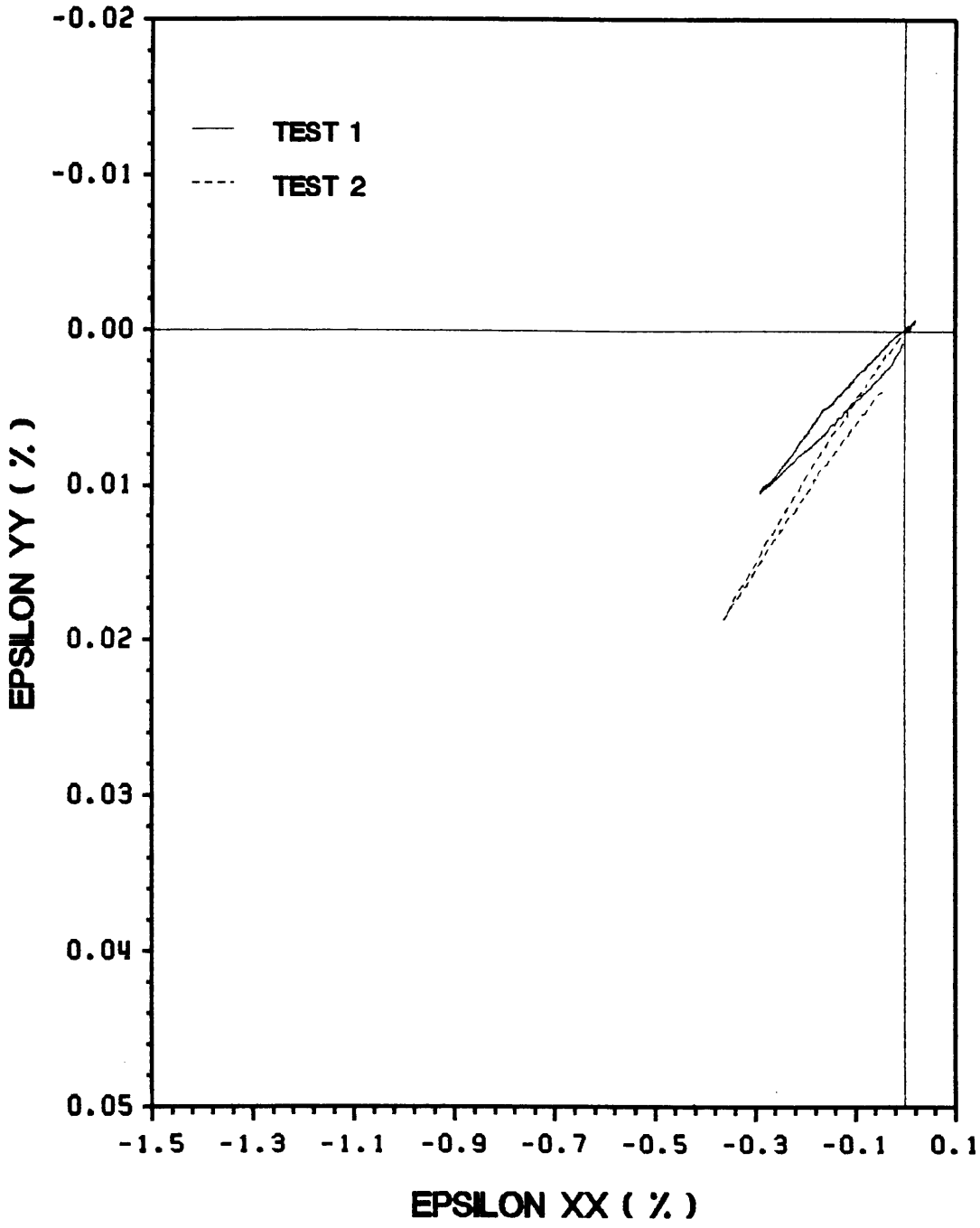

Figure A. 18. Poisson's response of 90° specimens under tension-compression-tension cyclic loading at room temperature

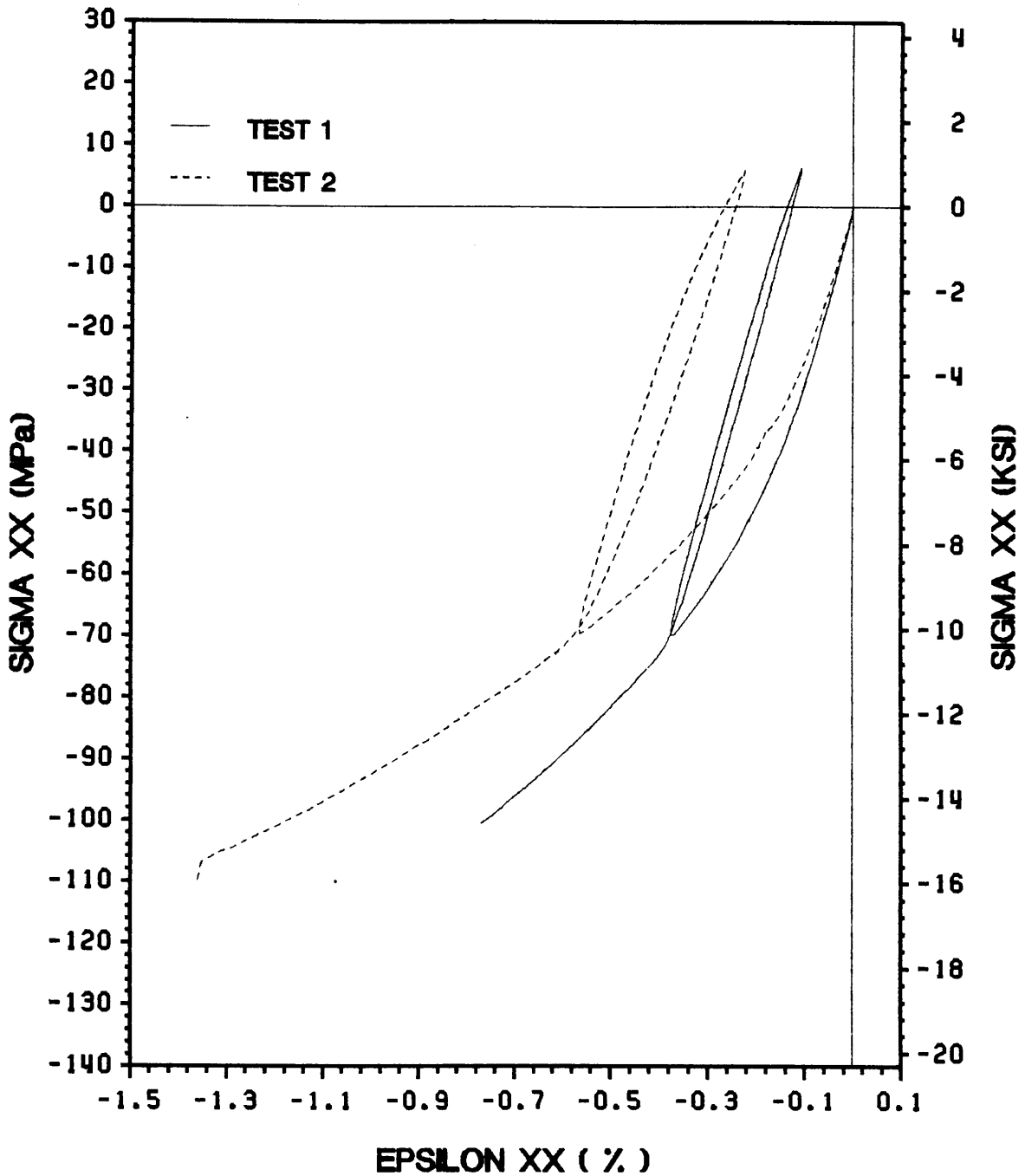

Figure A. 19. Longitudinal response of 90° specimens under compression-tension-compression cyclic loading at room temperature

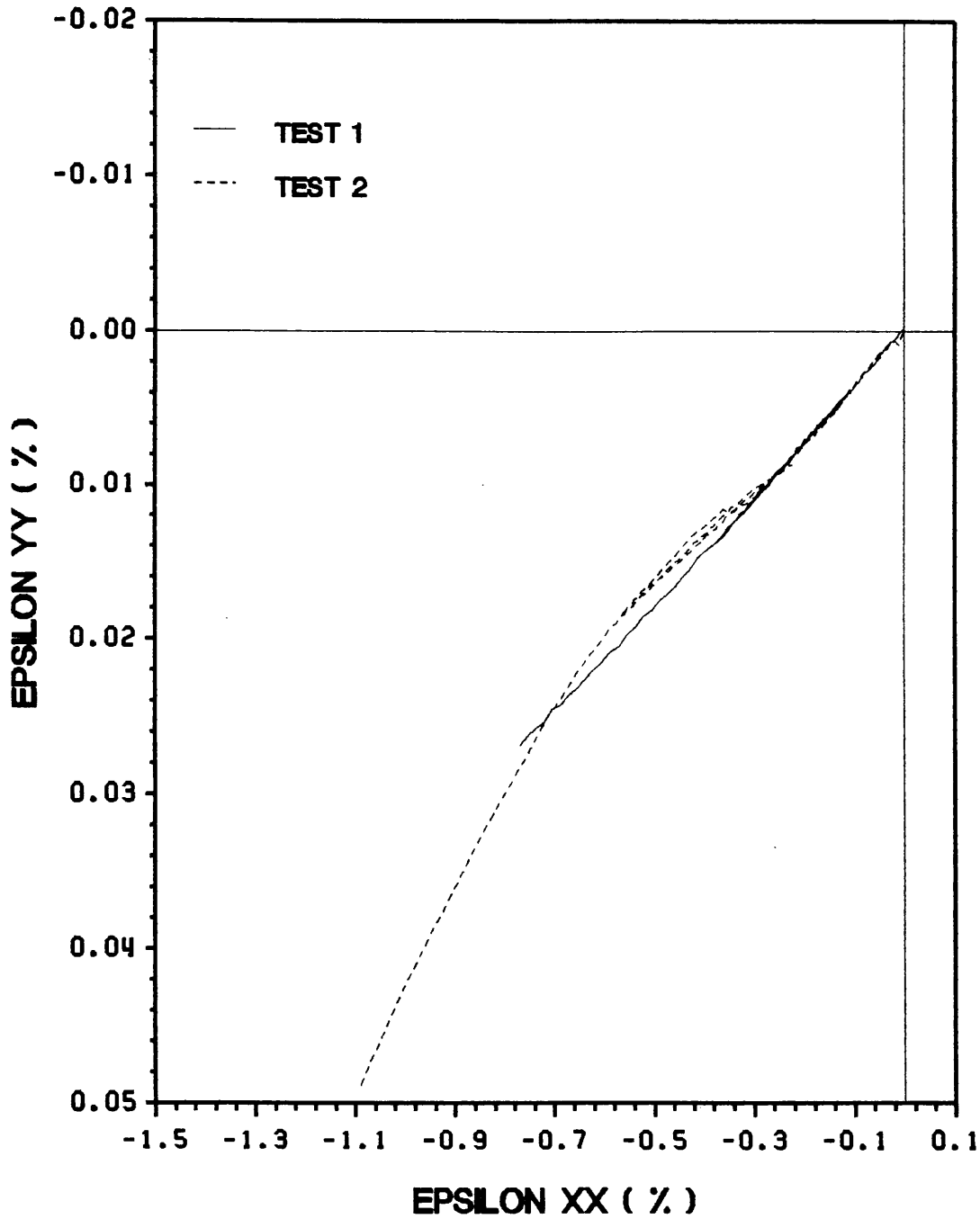

Figure A. 20. Poisson's response of 90° specimens under compression-tension-compression cyclic loading at room temperature

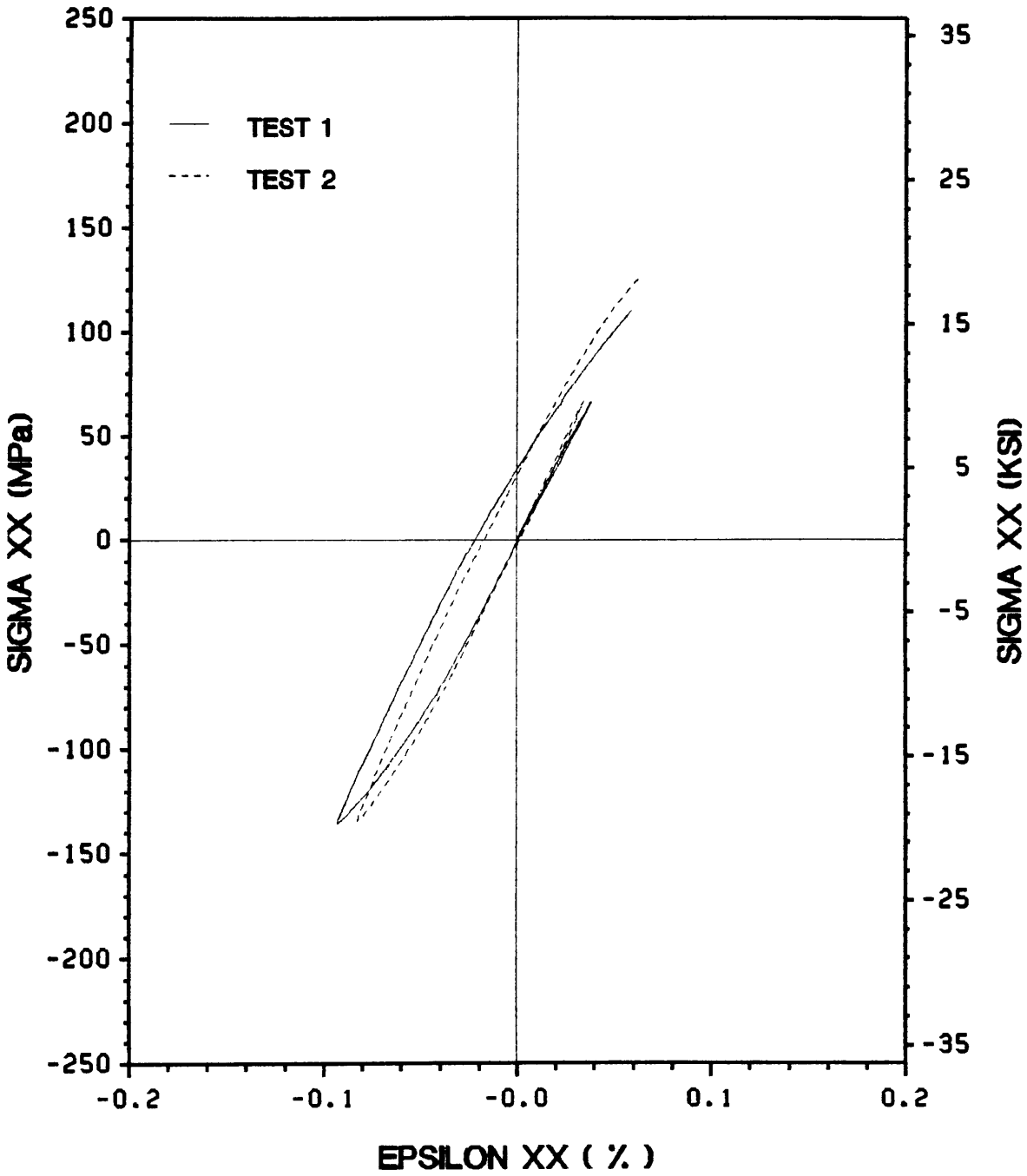

Figure A. 21. Longitudinal response of 15° specimens under tension-compression-tension cyclic loading at 250°F

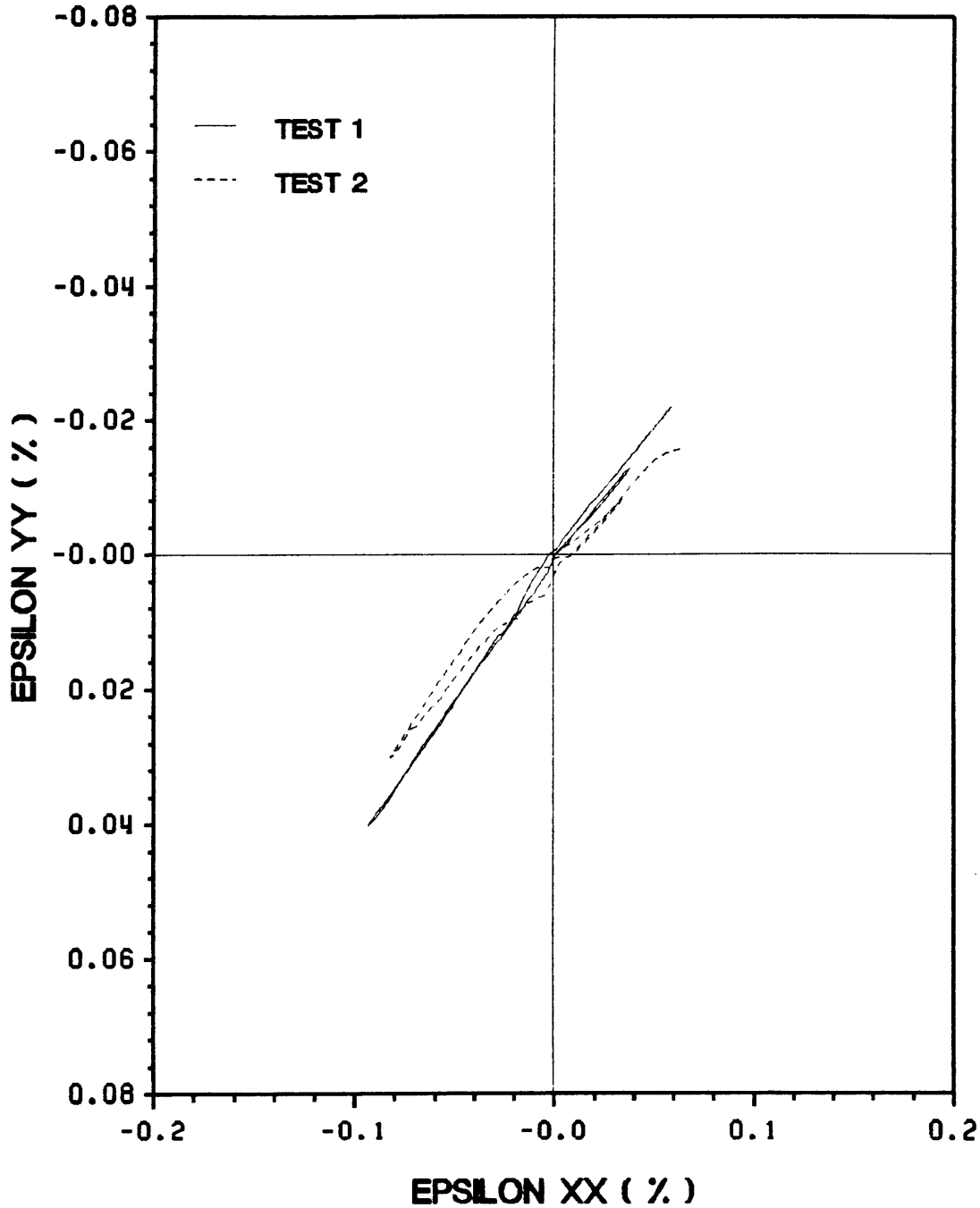

Figure A. 22. Poisson's response of 15° specimens under tension-compression-tension cyclic loading at 250°F

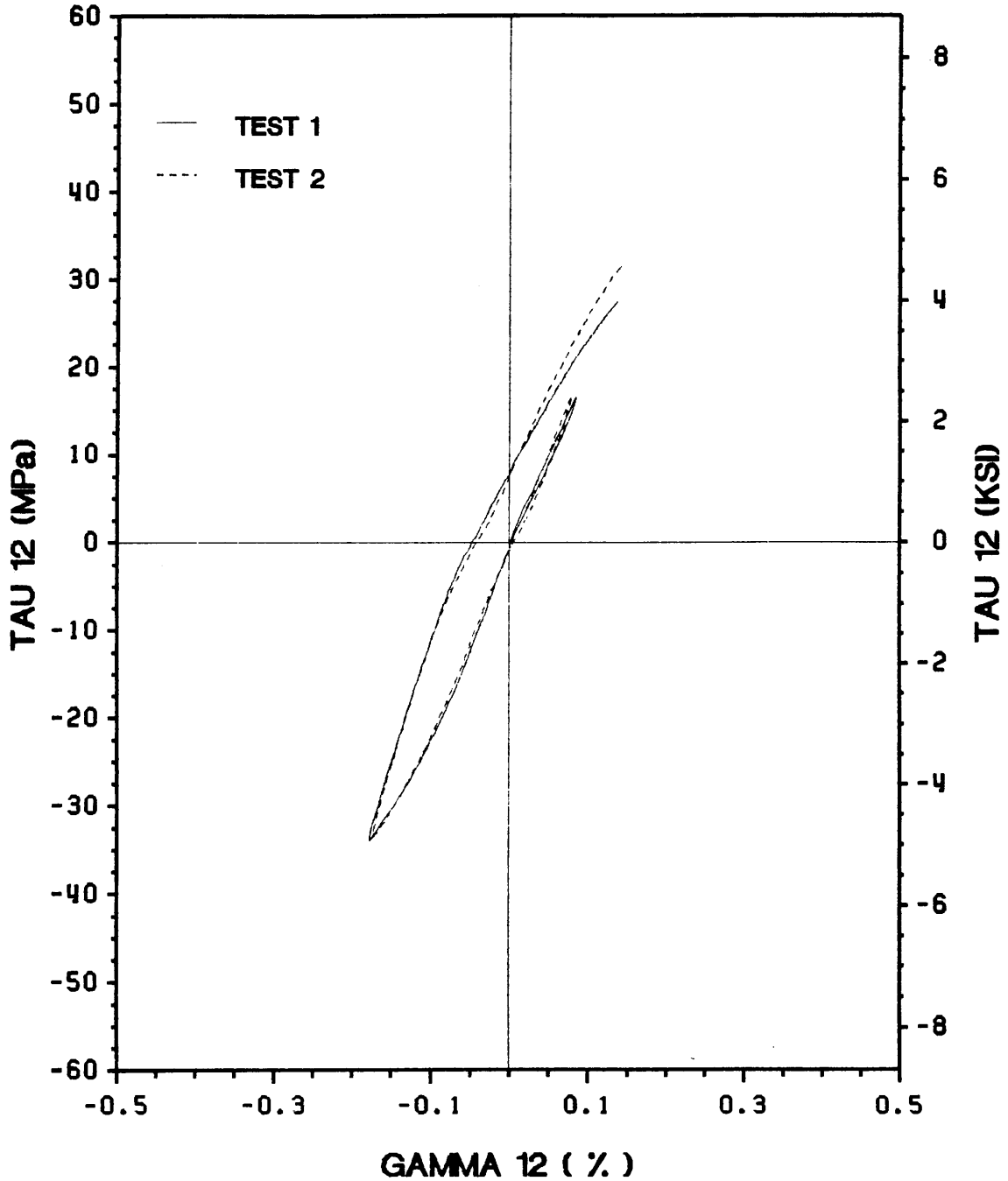

Figure A. 23. Shear response of 15° specimens under tension-compression-tension cyclic loading at 250°F

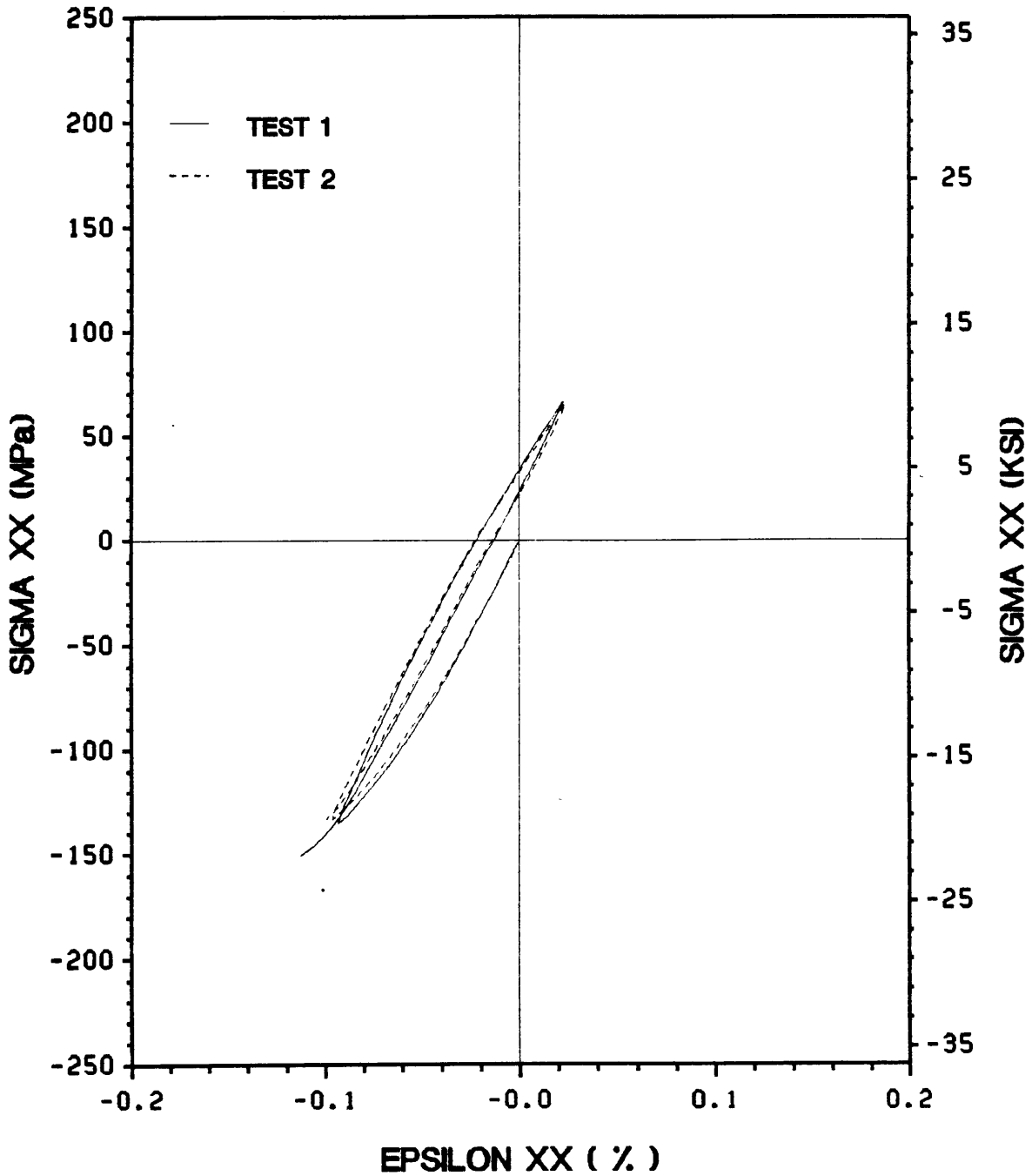

Figure A. 24. Longitudinal response of 15° specimens under compression-tension-compression cyclic loading at 250°F

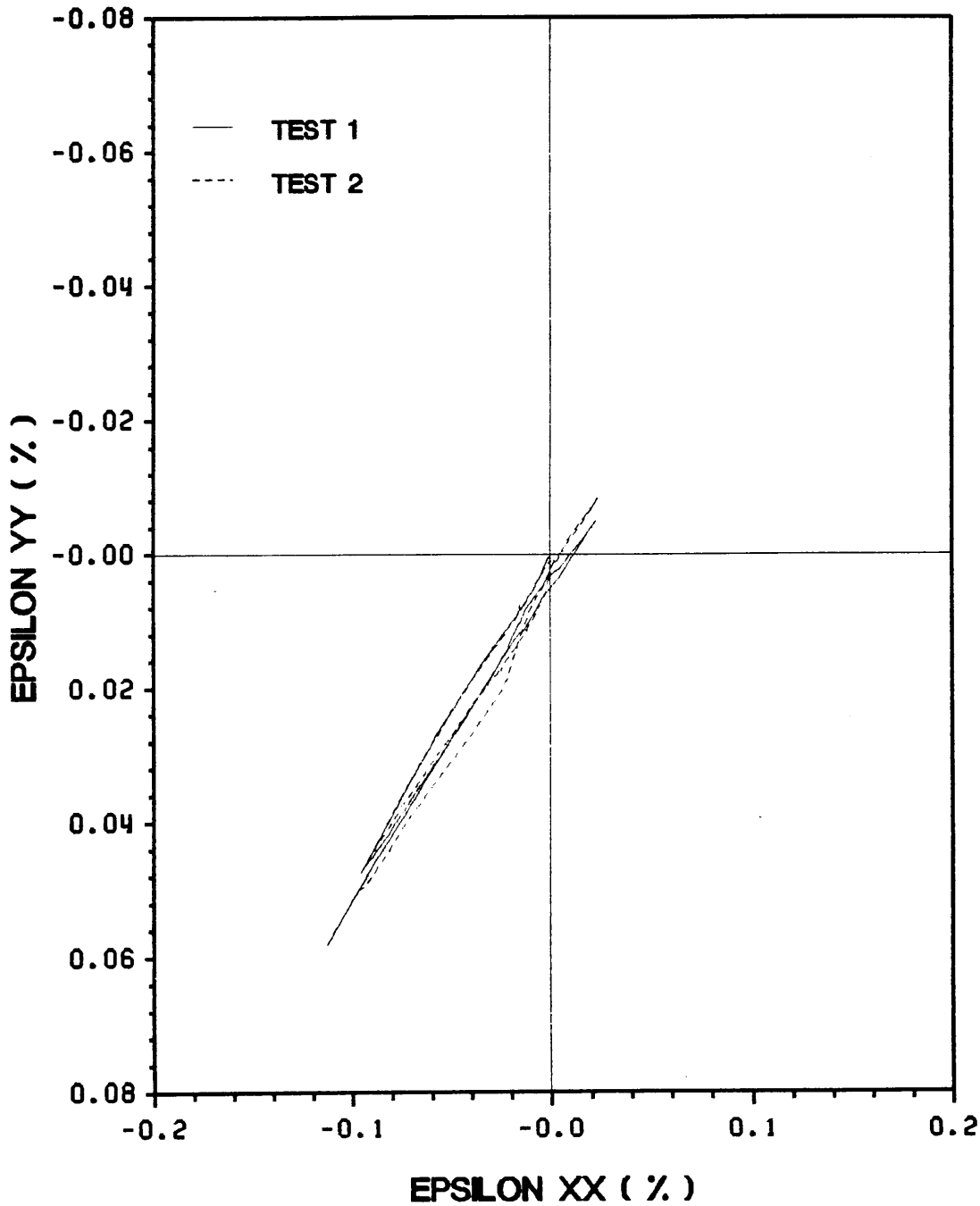

Figure A. 25. Poisson's response of 15° specimens under compression-tension-compression cyclic loading at 250°F

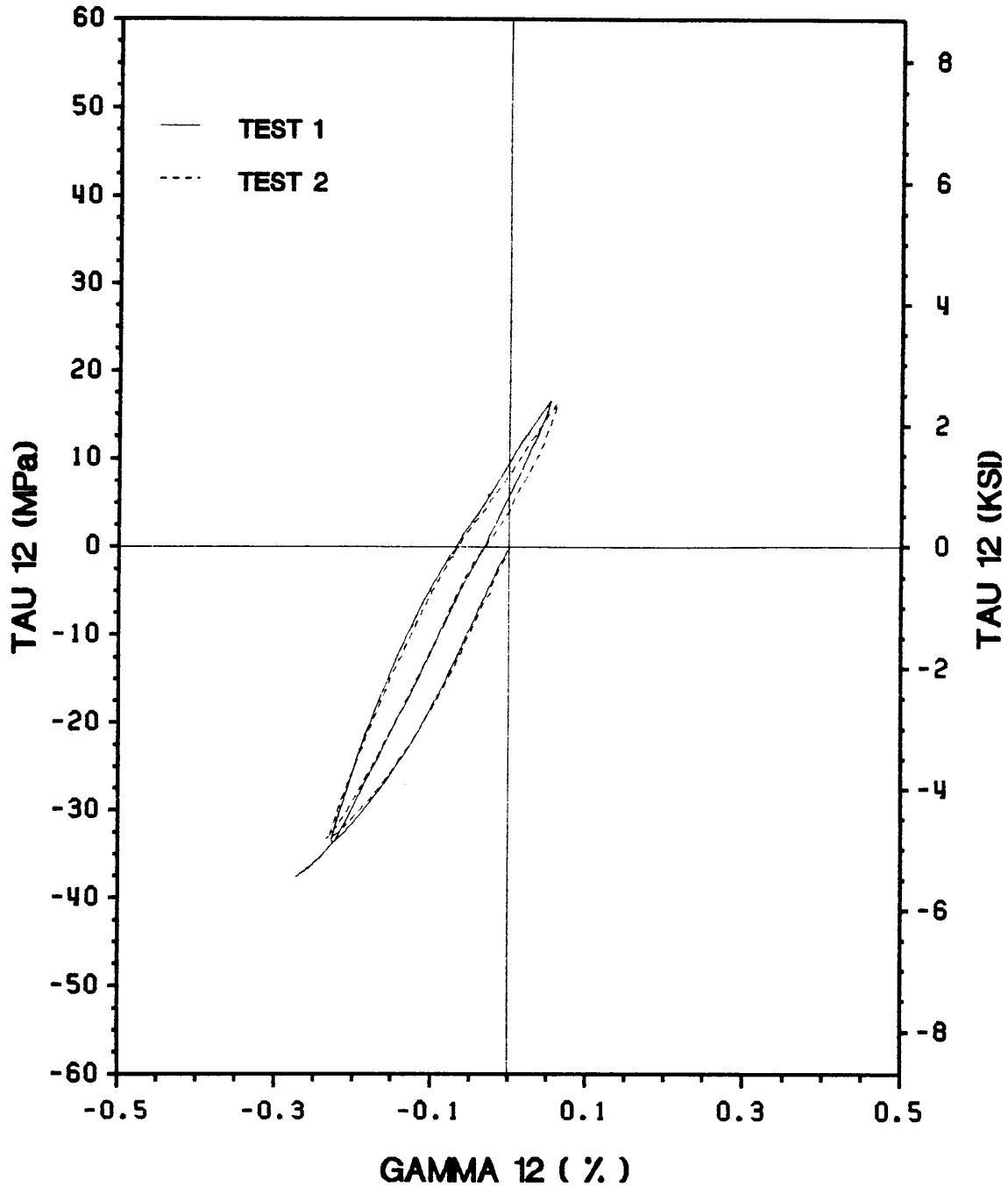

Figure A. 26. Shear response of 15° specimens under compression-tension-compression cyclic loading at 250°F

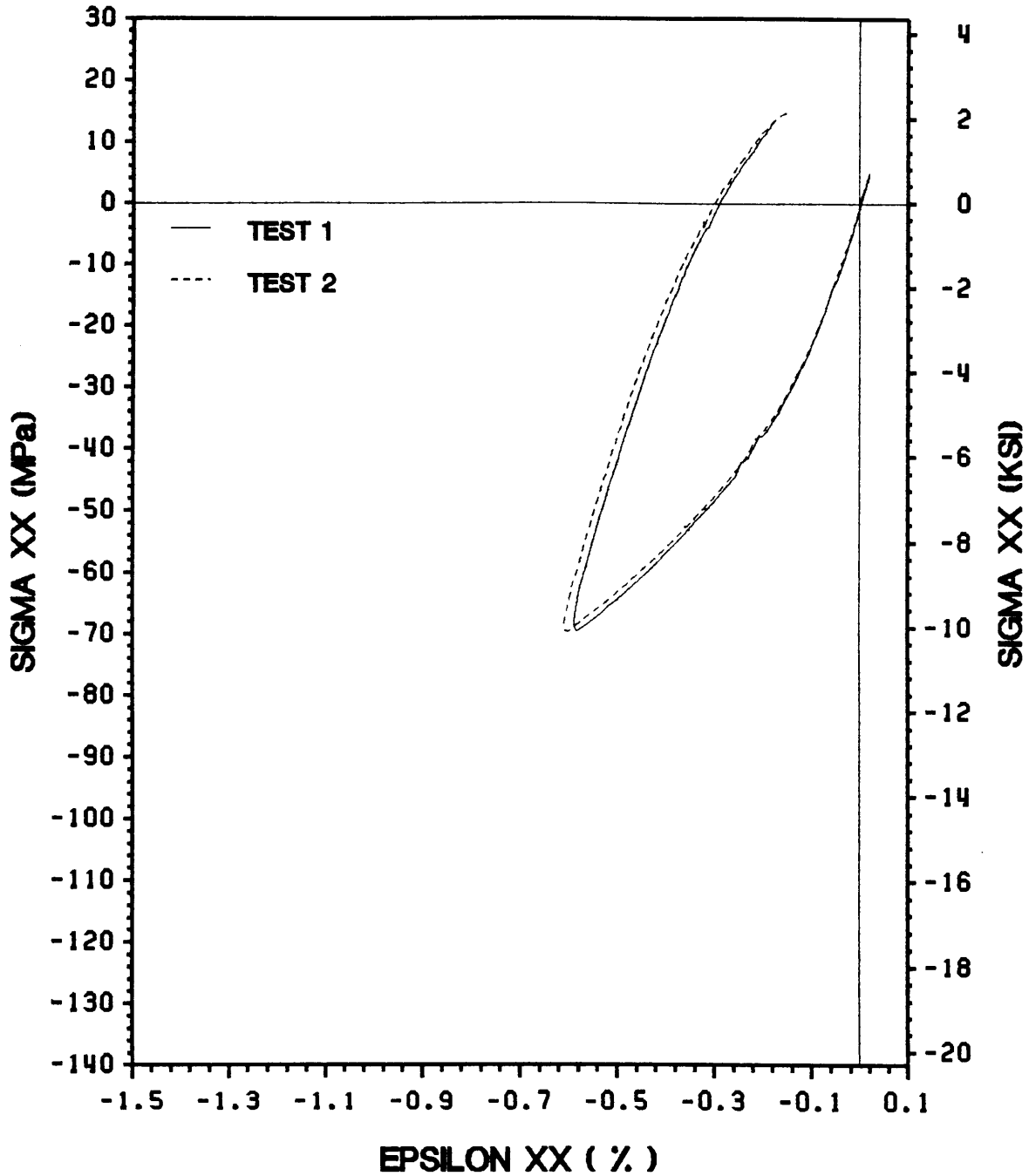

Figure A. 27. Longitudinal response of 90° specimens under tension-compression-tension cyclic loading at 250°F

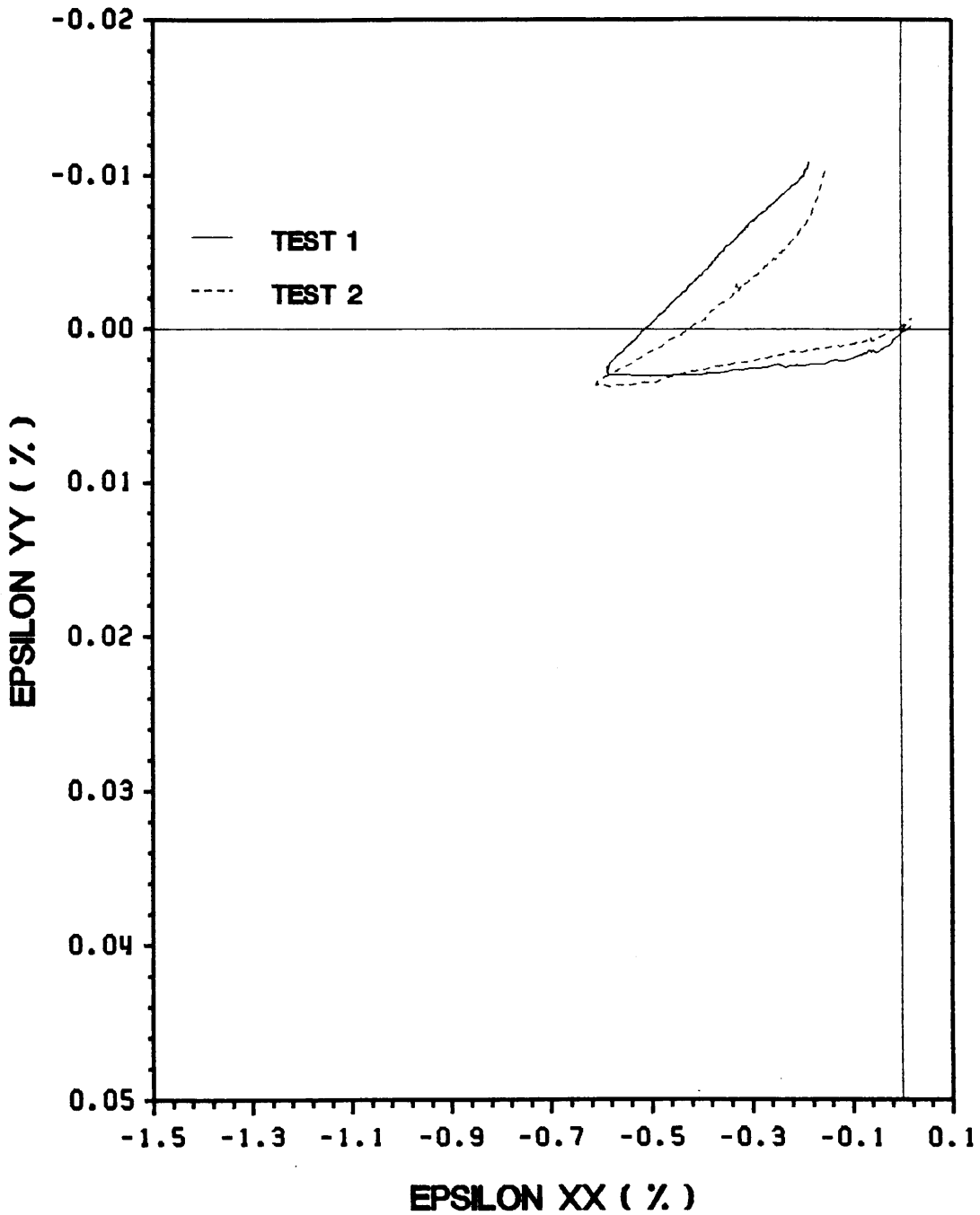

Figure A. 28. Poisson's response of 90° specimens under tension-compression-tension cyclic loading at 250°F

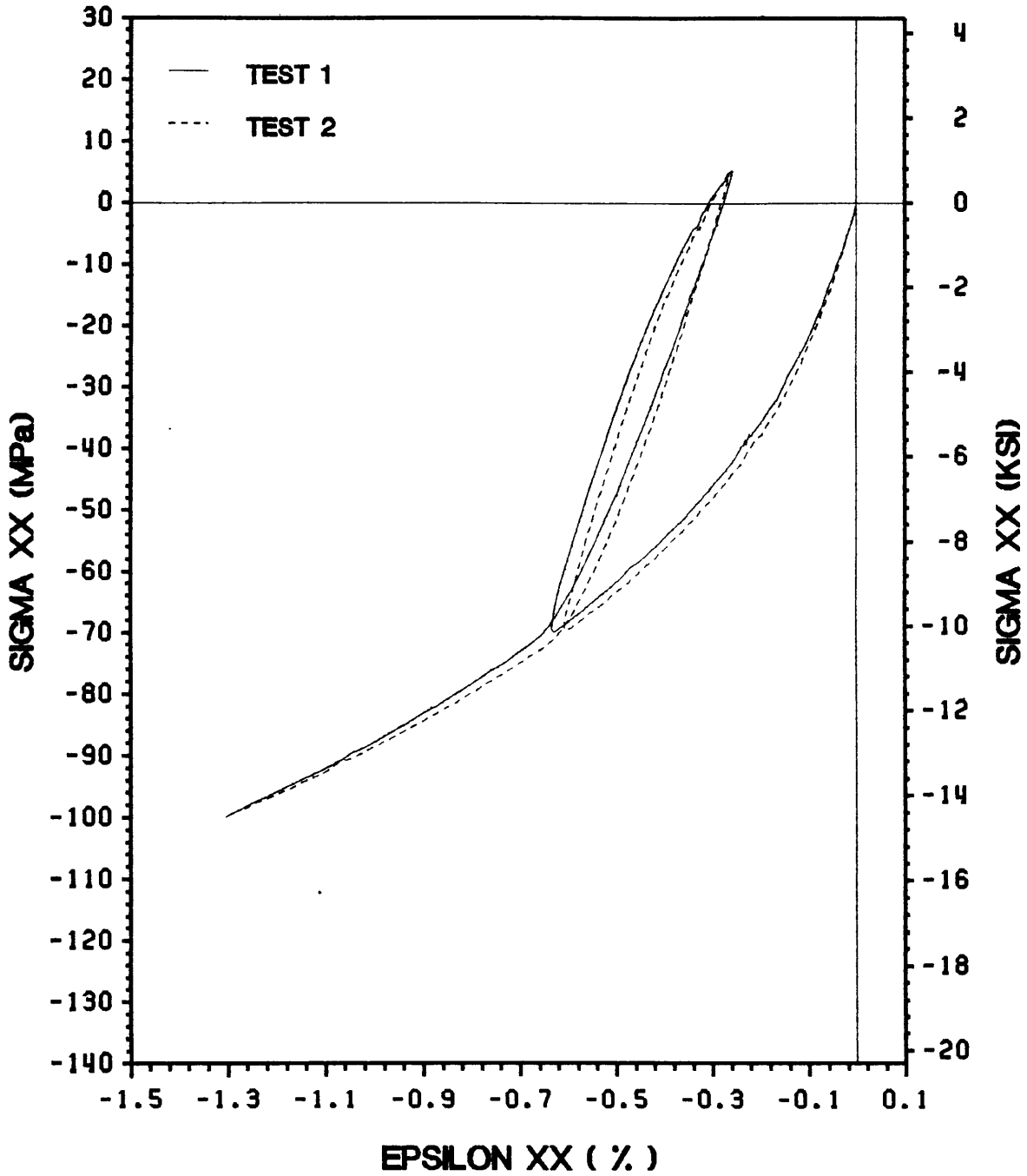

Figure A. 29. Longitudinal response of 90° specimens under compression-tension-compression cyclic loading at 250°F

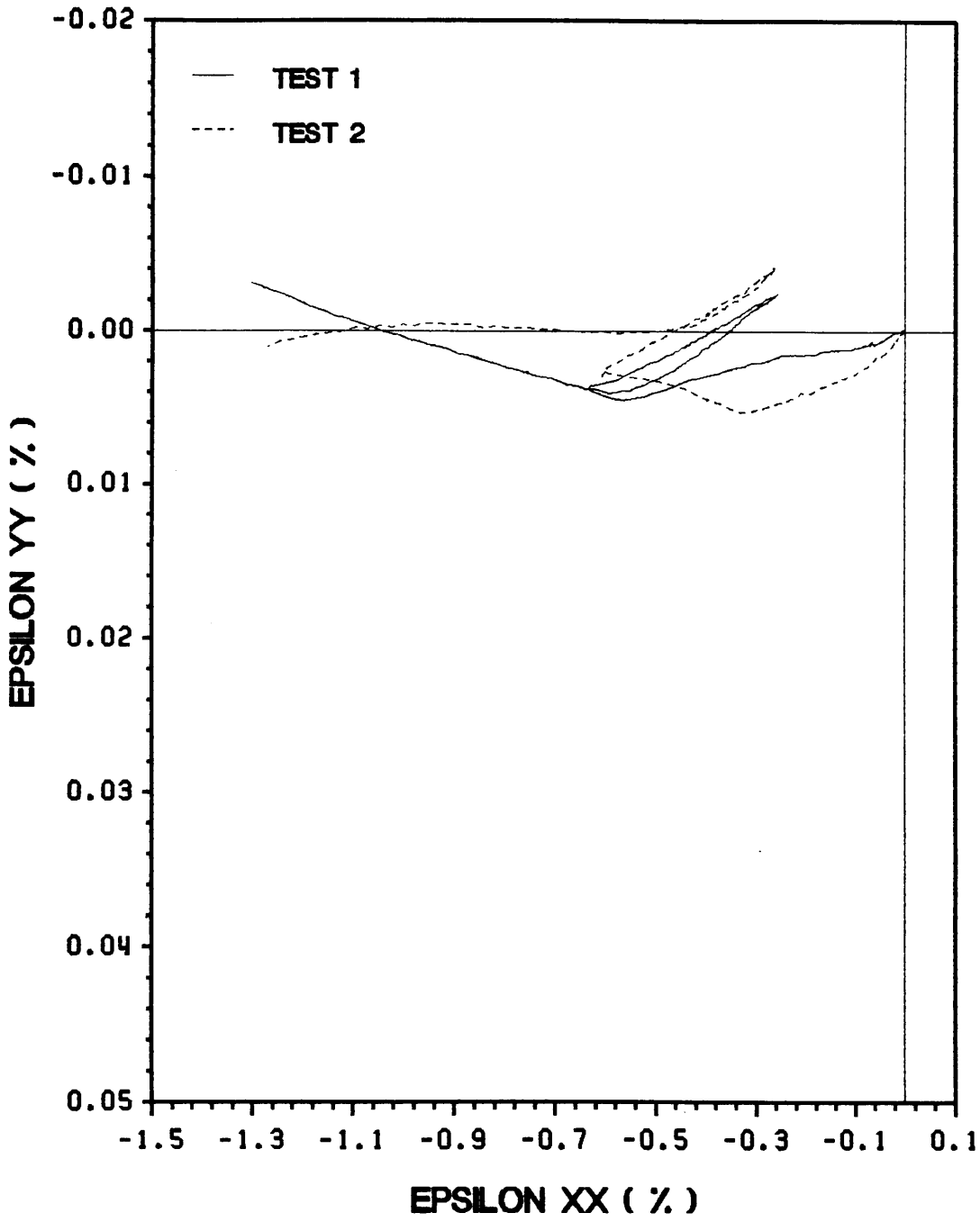

Figure A. 30. Poisson's response of 90° specimens under compression-tension-compression cyclic loading at 250°F

The vita has been removed from the scanned document